2010

Magnetic Nanosensors For Multiplexed Bacterial Pathogenesis Identification

Charalambos Kaittanis
University of Central Florida

MAGNETIC NANOSENSORS
FOR
MULTIPLEXED BACTERIAL PATHOGENESIS IDENTIFICATION

by

CHARALAMBOS KAITTANIS
B.S. The Pennsylvania State University, 2004

A dissertation submitted in partial fulfillment of the requirements
for the degree of Doctor of Philosophy
in the Burnett School of Biomedical Sciences
in the College of Medicine
at the University of Central Florida,
Orlando, Florida

Spring term
2010

Major Professor: J. Manuel Perez

Kaittanis C., Santra S., Perez J. M. Emerging nanotechnology-based strategies
for the identification of microbial pathogenesis.
Advanced Drug Delivery Reviews 2009 Nov 13.
Copyright 2009 Elsevier B.V.

Kaittanis C., Naser S. A., and Perez J. M. One-Step, Nanoparticle-mediated bacterial
detection with magnetic relaxation.
Nano Letters 2007 Feb;7(2):380-3.
Copyright 2007 American Chemical Society.

Kaittanis C., Santra S., Perez J. M. Role of nanoparticle valency in the nondestructive
magnetic-relaxation-mediated detection and magnetic isolation of cells in complex
media. JACS 2009 Sep 9;131(35):12780-91.
Copyright 2009 American Chemical Society.

Kaittanis C., Nath S., Perez J. M. Rapid nanoparticle-mediated monitoring of bacterial
metabolic activity and assessment of antimicrobial susceptibility in blood with magnetic
relaxation. PLoS ONE. 2008 Sep 23;3(9):e3253.

Nath S., Kaittanis C., Tinkham A., Perez J. M.
Dextran-coated gold nanoparticles for the assessment of antimicrobial susceptibility.
Analytical Chemistry. 2008 Feb 15;80(4):1033-8.
Copyright 2008 American Chemical Society.

ABSTRACT

Developing diagnostic modalities that utilize nanomaterials and miniaturized detectors can have an impact in point-of-care diagnostics. Diagnostic systems that (i) are sensitive, robust, and portable, (ii) allow detection in clinical samples, (iii) require minimal sample preparation yielding results quickly, and (iv) can simultaneously quantify multiple targets, would have a great potential in biomedical research and public healthcare. Bacterial infections still cause pathogenesis throughout the world (Chapter I). The emergence of multi-drug resistant strains, the potential appearance of bacterial pandemics, the increased occurrence of bacterial nosocomial infections, the wide-scale food poisoning incidents and the use of bacteria in biowarfare highlight the need for designing novel bacterial-sensing modalities.

Among the most prominent disease-causing bacteria are strains of *Escherichia coli*, like the *E. coli* O157:H7 that produces the Shiga-like toxin (Stx). Apart from diarrheagenic *E. coli* strains, others cause disease varying from hemolytic uremic syndrome and urinary tract infections to septicemia and meningitis. Therefore, the detection of *E. coli* needs to be performed fast and reliably in diverse environmental and clinical samples. Similarly, *Mycobacterium avium* spp. *paratuberculosis* (MAP), a fastidious microorganism that causes Johne's disease in cattle and has been implicated in Crohn's disease (CD) etiology, is found in products from infected animals and clinical samples from CD patients, making MAP an excellent proof-of-principle model.

Recently, magnetic relaxation nanosensors (MRnS) provided the first applications of improved diagnostics with high sensitivity and specificity. Nucleic acids, proteins, viruses and enzymatic activity were probed, yet neither large targets (for instance

bacterial and mammalian cells) nor multiple bacterial disease parameters have been simultaneously monitored, in order to provide thorough information for clinical decision making. Therefore, the goal of this study was to utilize MRnS for the sensitive identification of multiple targets associated with bacterial pathogenesis, while monitoring virulence factors at the microorganism, nucleic acid and virulence factor levels, to facilitate improved diagnosis and optimal treatment regimes. To demonstrate the versatility of MRnS, we used MAP as our model system, as well as several other pathogens and eukaryotic cell lines.

In initial studies, we developed MRnS suitable for biomedical applications (Chapter II). The resulting MRnS were composed of an iron oxide core, which was caged within a biodegradable polymeric coating that could be further functionalized for the attachment of molecular probes. We demonstrated that depending on the polymer used the physical and chemical properties of the MRnS can be tailored. Furthermore, we investigated the role of polymer in the enzyme-mimicking activity of MRnS, which may lead to the development of optimized colorimetric *in vitro* diagnostic systems such as immunoassays and small-molecule-based screening platforms.

Additionally, via facile conjugation chemistries, we prepared bacterium-specific MRnS for the detection of nucleic acid signatures (Chapter III). Considering that MAP DNA can be detected in clinical samples and isolates from CD patients via laborious isolation and amplification procedures requiring several days, MRnS detected MAP's IS900 nucleic acid marker up to a single MAP genome copy detection within 30 minutes. Furthermore, these MRnS achieved equally fast IS900 detection even in crude DNA extracts, outperforming the gold standard diagnostic method of nested Polymerase Chain

Reaction (nPCR). Likewise, the MRnS detected IS900 with unprecedented sensitivity and specificity in clinical isolates obtained from blood and biopsies of CD patients, indicating the clinical utility of these nanosensors.

Subsequently, we designed MRnS for the detection of MAP via surface-marker recognition in complex matrices (Chapter III). Milk and blood samples containing various concentrations of MAP were screened and quantified without any processing via MRnS, obtaining dynamic concentration-dependent curves within an hour. The MAP MRnS were able not only to identify their target in the presence of interferences from other Gram positive and Gram negative bacteria, but could differentiate MAP among other mycobacteria including *Mycobacterium tuberculosis*. In addition, detection of MAP was performed in clinical isolates from CD patients and homogenized tissues from Johne's disease cattle, demonstrating for the first time the rapid identification of bacteria in produce, as well as clinical and environmental samples.

However, comparing the unique MAP quantification patterns with literature-available trends of other targets, we were prompted to elucidate the underlying mechanism of this novel behavior (Chapter IV). We hypothesized that the nanoparticle valency – the amount of probe on the surface of the MRnS – may have modulated the changes in the relaxation times ($\Delta T2$) upon MRnS – target association. To address this, we prepared MAP MRnS with high and low anti-MAP antibody levels using the same nanoparticle formulation. Results corroborated our hypothesis, but to further bolster it we investigated if this behavior is target-size-independent. Hence utilizing small-molecule- and antibody-carrying MRnS, we detected cancer cells in blood, observing similar detection patterns that resembled those of the bacterial studies. Notably, a single cancer

cell was identified via high-valency small-molecule MRnS, having grave importance in cancer diagnostics because a single cancer cell progenitor in circulation can effectively initiate the metastatic process. Apart from cells, we also detected the Cholera Toxin B subunit with valencly-engineered MRnS, observing similar to the cellular targets' diagnostic profiling behavior.

Finally, as bacterial drug resistance is of grave healthcare importance, we utilized MRnS for the assessment of bacterial metabolism and drug susceptibility (Chapter V). Contrary to spectophotometric and visual nanosensors, their magnetic counterparts were able to quickly assess bacterial carbohydrate uptake and sensitivity to antibiotics even in blood. Two MRnS-based assay formats were devised relying on either the Concanavalin A (Con A)-induced clustering of polysaccharide-coated nanoparticles or the association between free carbohydrates and Con A-carrying MRnS. Overall, taking together these results, as well as those on pathogen detection and the recent instrumentation advancements, the use of MRnS in the clinic, the lab and the field should be anticipated.

Dedicated to

Androula and Giorgos – my parents

The ones who with patience and sacrifices brought me up.

The ones who taught me to seek the stars,

and not to be afraid of the shadows of failure.

The ones who traveled with me to new Ithacas,

and gave me the passion to fight Laestrygonians and Cyclops.

ACKNOWLEDGMENTS

The breeze was cool, scented with jasmine and citrus. He was sitting with his parents under the starry sky. They always loved asking him how his day went and what new he learnt at school. He was nine, and today he was so fascinated by electromagnetism and how a compass aligns within an electric field. His parents were quiet. Moments after, his father pointed the Polaris. "Son, do not let any interferences affect you. Make your dreams a Pole Star and let it guide you. Never forget that even if it's cloudy, rays from the Sun and the Moon will always reach you." And they always did. My parents. Without their support and parenthood, I wouldn't have reached a plethora of milestones, including the completion of this endeavor. With their love and guidance, their zeal for education and excellence, I managed to accomplish this task. From helping me with homework when I was little to driving me to classes when I was a teenager, and from paying for my undergraduate education to sharing with me the beauty of the world, I owe them a lot. But parents they are, they were simply happy when new experiences, new aromas, filled my life.

Once, a young man named Alexander said "I am indebted to my parents for my life, but to my teachers for the quality of my life". Years after, history called him Great for disseminating the Greek spirit to other nations. Indeed my quality of life and scientific training are affected by my teachers. For that, first and foremost I would like to thank Dr. J. Manuel Perez; my advisor. His patience and mentorship helped me throughout this process. His office, a refuge to protect me from the turmoil, was always open, with him ready to hear my worries and give advice. I do thank him not only for the technical training he provided me with, but also for the opportunities he gave me to sharpen my

your backyard barbequing, teasing a guy in black with the name of Johnnie, and discussing about science, politics, and philosophy were so valuable to me; balsam for the spirit and nourishment for the mind. Diana, I thank you for the endless discussions on Life. Having coffee and examining the present under the lenses of great educators made me appreciate life's timbre and decipher Dostoevsky's "Beauty will save the World". It was my privilege to meet you at a Phoenician trading station, enriching this journey with pearls and perfumes.

I do want to acknowledge the educational system of Cyprus that embraces humanism. The values obtained through it were beacons in this journey. Concluding, I thank both you – the reader – and science for letting me be part of the eternal process of discovery and expansion, seeking the Truth.

TABLE OF CONTENTS

LIST OF FIGURES

LIST OF TABLES

LIST OF ACRONYMS/ABBREVIATIONS

AFM	atomic force microscopy
Ag-NP	silver nanoparticles
Au-NP	gold nanoparticles
CD	Crohn's disease
CFU	colony forming units
Con A	Concanavalin A
Ctb	cholera toxin B subunit
dH$_2$O	deionized water
DI	Deionized
DLS	Dynamic light scattering
ELISA	enzymed-linked immunosorbent assay
FR	folate receptor
FT-IR	Fourier transform infrared spectroscopy
IONP	iron oxide nanoparticles
K_m	Michaelis constant
MAP	*Mycobacterium avium* spp *paratuberculosis*
MIC	minimum inhibitory concentration
MRI	magnetic resonance imaging
MRnS	magnetic relaxation nanosensors
MRSA	methicillin-resistant *Staphylococcus aureus*
nPCR	nested Polymerase Chain Reaction
PAA	polyacrylic acid
PBS	phosphate buffered saline
PCR	polymerase chain reaction
Qdots	quantum dots
R1	spin-lattice relaxivity
R2	spin-spin relaxivity
RAPID-PCR	random-primed polymerase chain reaction
SE	standard error
SQUID	superconducting quantum interference device
T2	spin-spin relaxation time
TEM	Transmission electron microscopy
TMB	3,3',5,5'-tetramethylbenzidine
UV-vis	ultraviolet-visible
V_{max}	maximum reaction rate
XDR-TB	extremely drug-resistant *Mycobacterium tuberculosis*

ΔT2   change in spin-spin relaxation time

CHAPTER I: GENERAL INTRODUCTION UNWRAPING THE BOX OF BACTERIAL PATHOGENESIS
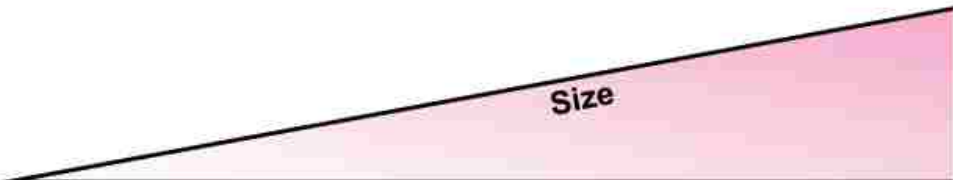
Bacteria and other infectious agents inflict human pathogenesis and mortality throughout the world, exceeding cardiovascular diseases and cancer[1]. Despite the great progress in sanitation, as well as identification and control of several infections diseases in developed countries, problems persist with food contamination, hospital-acquired pathogens, and sexually transmitted diseases[2, 3]. In the developing countries of sub-Sahara Africa and Southeast Asia, but even in remote areas of Western countries, infectious diseases primarily occur due to poor sanitation and lack of sensitive and efficient technologies to rapidly identify and treat these conditions[2, 3]. Additional reasons that contribute to the extensive transmission of infectious diseases include living close to infected animals and contaminated water, and the socioeconomic trends and political instability often observed in many developing nations[4]. Therefore, upgrading the living conditions and diagnostic protocols in poor rural areas is critical in controlling the spread of disease before becoming pandemic. Also, as modern global traveling facilitates the spread of disease faster than ever, developing fast, simple and accurate methods to identify infectious diseases at the points-of-care is of major importance.

Bacteria, as well as other infectious agents, are capable of causing disease with symptoms that can be manifested within minutes, or after a couple of hours to days or even years after the initial infection. These pathogenic agents are subject to transmission from either an infected individual or vector (such as ticks and birds) to a healthy individual[4]. The complexity and plethora of pathogens that cause disease, in addition to the prolonged incubation time before manifestation of clinical symptomology, make the

diagnosis of some of these conditions challenging. In general though, infectious agents

can be classified within groups, depending on their nature, size, phenotype, transmission

routes and genetic makeup (Table 1 and Figure 1).

Table 1 The repertoire of infectious agents.
Differences in size, morphology, infection mode, pathogenesis mechanisms, clinical
symptomology and disease highlight the need for development of sensitive and specific
pathogen identification modalities in diverse settings.

	Prions	Viruses	Bacteria	Fungi	Protozoa	Parasitic worms
Major Characteristics	- Misfolded proteins - No autonomous replication	- Capsid-coated genome - Host-dependent replication	- Unicellular prokaryotes - Autonomous metabolism and replication	- Osmotrophic eukaryotes - Environmental or animal infection	- Single cell - Heterotrophic eukaryotes - Water and soil infection	- Eukaryotes - Residence inside the body
Transmission	- Contaminated food/fluids	- Contaminated blood/body fluids/ aerosols	- Contaminated food/aerosols - Environment - Hospitals	- Environment - Vectors	- Environment - Vectors	- Vectors
Biomarkers	- Misfolded proteins	- Epitopes - Genomic sequences - Circulating antibodies	- Epitopes - Toxins - Genomic sequences - Circulating antibodies	- Toxins - Circulating antibodies	- Epitopes - Proteins	- Epitopes - Proteins
Disease	- Creutzfeldt – Jakob - Scrapie - Bovine spongiform encephalopathy	- Hepatitis - AIDS - Hemorrhagic fever	- Intoxication - Meningitis - Tuberculosis	- Candidiasis - Cryptococcosis - Sporotrichosis	- Malaria - Toxoplasmosis - Dysentery	- Schistosomiasis - Lymphatic filariasis

Current technologies for bacterial diagnosis and their limitations

Traditionally, the presence of bacteria in a clinical sample is determined via microscopy usually after growth in pure culture, followed by growth in differential media and biochemical tests to confirm the microorganism's identity. Despite their specificity, these methods have limitations. For instance, samples with high pathogen loads are needed for microscopy-based methods. Second, growth pattern methods require at least a 24-hour incubation period to provide results. Third, as some microorganisms cannot grow easily in culture, their identification is daunting.

In order to circumvent these limitations, with the discovery of DNA and the development of Polymerase Chain Reaction (PCR), microbiologists adopted a molecular-based diagnostic frameset in the last quarter of the 20th century. Specifically, instead of looking for the microorganism as an entity itself, they started looking for genes associated with its virulence and disease patterns. Consequently, there was a rise in genome sequencing and the deposition of the annotated genome in databases[4]. Based on this information, DNA microarrays have been developed, identifying DNA segments corresponding to an organism's genome. These methodologies are highly sensitive and selective, achieving detection down to the single pathogen. Despite this, the major limitation of the gene chip is that it cannot provide critical information about the pathogen's specific RNA (transcriptional) and protein (translational) levels. Furthermore, it cannot address how these parameters are modulated by factors and processes that may alter the microorganism's growth, as well as how the host's immune response affects the microorganism's expression patterns at the transcriptional and translational levels. Apart from PCR, several other molecular diagnostic methods have been introduced, such as

RAPID-PCR, checkerboard hybridization, ligase chain reaction, ribotyping using restriction length polymorphisms, and pulsed-field gel electrophoresis[4]. Despite their distinct advantages, all of these methods require undamaged and highly pure microbial DNA and have to be performed in a laboratory setting by experienced personnel using expensive instrumentation and reagents. Therefore, the associated cost of these molecular diagnostic modalities is high enough to prohibit their wide-scale use at the points-of-care and in developing nations.

In addition to microscopy- or nucleic-acid-based techniques, the identification of a pathogen can be achieved via immunoassays targeting specific proteins or carbohydrates moieties unique to the pathogen. Such methods include agglutination tests, fluorescent immunoassays, enzyme-linked immunosorbent assays (ELISA) and Western blot analyses[4]. Although these methods are very sensitive, they detect a pathogen's molecular 'fingerprints', such as proteins and cell wall epitopes. Hence, as these assays do not provide any direct information about the presence and metabolic state of a microorganism, the administration of suitable antibiotics or other therapeutic agents cannot be achieved. Additionally, as these methods regularly utilize an antibody for the recognition of bacterial targets, proper handling and storage is needed in order to prevent antibody denaturation. Furthermore, these assays are affected by the clinical sample's nature, because the specimen, for instance blood, often times needs to undergo processing before being analyzed. Similarly, flow cytometry [5-7] and phage typing [6] face limitations imposed by the sample's characteristics, as optically opaque or viscous samples can interfere with the readout, whereas the assay's portability is hindered by the bulky instrumentation. Likewise, magnetic micro-beads have been used for the magnetic

separation and identification of microbes through PCR and flow cytometry[7, 8], yet these methods require several intermediate steps and have limited capabilities in complex biological samples.

Pathogenesis caused by intracellular pathogens, such as *Mycobacterium tuberculosis* among others, relies on the survival of the microorganism within host cells, including macrophages, dendritic cells and T helper cells[9]. This mode of infection and the frequent absence of clinical symptomology hamper these pathogens' detection and prevent treatment and containment. Consequently, the physician cannot proceed to the assignment of an appropriate treatment course, delaying the clearance of the pathogen from the body. Current tests cannot detect intracellular pathogens in biological fluids, such as the blood and lymph fluid, as most of these tests are based on fluorescence emission in the absence of optical interference. Hence, the need for developing optical-independent diagnostic modalities is pivotal for the detection of intracellular pathogens in body fluids and biopsies, with no or minimal sample preparation steps. Furthermore, these modalities should be able to facilitate multi-sensing capabilities, detecting not only the microorganism per se, but its genomic fragments and protein markers. This could corroborate bacterial identification and prevent misdiagnosis due to cross-reactivity [4] that tends to be common in serological assays.

The challenge of detecting toxins

Toxins are virulence factors that affect the host cell's physiological processes and plasma membrane integrity, causing cytotoxicity[10]. For instance, toxins, like listeriolysin O from *L. monocytogenes*, create pores in and disrupt the phospholipid bilayer, causing host cell's lysis[11]. Other toxins, such as Shiga toxin, inhibit protein synthesis, which in

turn activate apoptotic and necrotic cascades[12, 13]. Furthermore, toxins, like anthrax and botulism, alter the host cell's signal transduction cascades. These alterations initiate the disease state and ultimately lead to the host cell's death[14]. Hence through exploitation of numerous mechanisms, bacterial toxins affect host cell's homeostasis and induce cell death, aiming to the release of nutrients needed for microbial survival and colonization. Particularly, intracellular pathogens that have a potent toxin in their virulence repertoire utilize the toxin as a key exit mechanism, a tool for further infection and manifestation within the body.

As toxins can cause significant pathogenesis, developing sensitive, fast and reliable diagnostics methods could minimize their harmful effects. Most importantly, toxins might remain in environmental, food or clinical samples long after the corresponding pathogen secreted them. Therefore, screening these samples for the presence of active toxins is   highly important to minimize intoxication and economic losses, particularly during a pandemic. Current toxin detection methods utilize antibody-antigen interactions in ELISA[15], Western blots[16, 17], antibody microarrays[18], surface plasmon resonance biosensors[19], and antibody-coated polystyrene microbeads[20]. These methods are relatively sensitive and have multiplexing capabilities, but require homogeneous or purified samples. Although time-consuming and laborious, these purification procedures are critical for assay sensitivity and specificity, as they minimize background noise. A major limitation of these assays is their spectrophotometric or fluorimetric determination mode. Thus, limited biological and environmental samples can be screened. To circumvent this obstacle, toxin detection techniques that utilize mass spectrometry, such as Liquid Chromatography Mass Spectrometry (LC-MS) [21]and

Multidimensional Protein Identification (MudPIT)[22], have been developed and achieved high sensitivities. However, the lack of portability and user-friendliness, as well as the sophisticated instrumentation, prevent the broader use of these diagnostic methods.

Limitations of current technologies and the rise of nanotechnology

Conventional molecular diagnostic techniques are widely used in laboratories throughout the world to identify pathogenic agents with high sensitivity and reproducibility. However, most of these techniques cannot be utilized in the field (e.g. airports and food distribution centers) or in developing countries where resources are scarce, because they require sophisticated, expensive instrumentation that needs to be used by trained personnel. Additionally, the high cost and short shelf life of some reagents, such as enzymes and DNA primers, limit the application of most conventional pathogen detection techniques in developing nations. Furthermore, despite their sensitivity, current technologies, like ELISA and PCR, require extensive sample preparation and have long readout times, which delay prompt response and disease containment.

Hence considering these, nanotechnology presents a great opportunity to develop fast, accurate and cost effective diagnostics for the detection of pathogenic infectious agents[23, 24]. Due to the presence of unique properties in nanoscale materials, devices able to report the presence of a pathogenic agent in clinical or environmental samples can be designed. The properties observed in nanomaterials are different from those observed in the bulk (micron-size) material due to their small size (1-100 nm) and large surface area, resulting in enhanced surface reactivity, quantum confinement effects, increased

7

electrical conductivity and improved magnetic properties, among others[24]. Most importantly, modifications of the nanostructures' surface can alter dramatically some of their properties[25, 26]. Hence, a single binding event can be potentially recorded.

Apart from striving for sensitivity and speed, nanotechnologists have geared their efforts towards the development of nanotechnology-based systems that are affordable, robust and reproducible, making them suitable for applications even in rural areas of developing nations. For instance, researchers try to formulate cheap and stable nanoparticles via novel facile synthetic routes, making nanoparticle-based diagnostic assays globally accessible and deliverable. Moreover, using innovative approaches, nanotechnology has the potential to build assays that can be performed in opaque media, like blood and milk, without any sample preparation, providing fast and reliable results in simple and user-friendly formats.

Popular nanotechnologies

The properties of the nanomaterials can be tailored by changing the size, shape, composition and surface modification of the nanomaterial. Particularly, their electronic, spectroscopic (emissive, absorptive), light scattering and conductive properties can be modified by engineering the nanoparticles' structural parameter, including their size, composition, self assembly and binding properties[24]. Below, some of the most commonly used nanosystems are described. It should be noted that a particular nanosystem, for example a nanoparticle of 100 nm in size including its coating and targeting ligands, can be designed to sense targets that might be smaller (i.e. lipids), bigger (i.e. bacteria) or of equal size (viruses) to the nanoparticle (Figure 1).

8
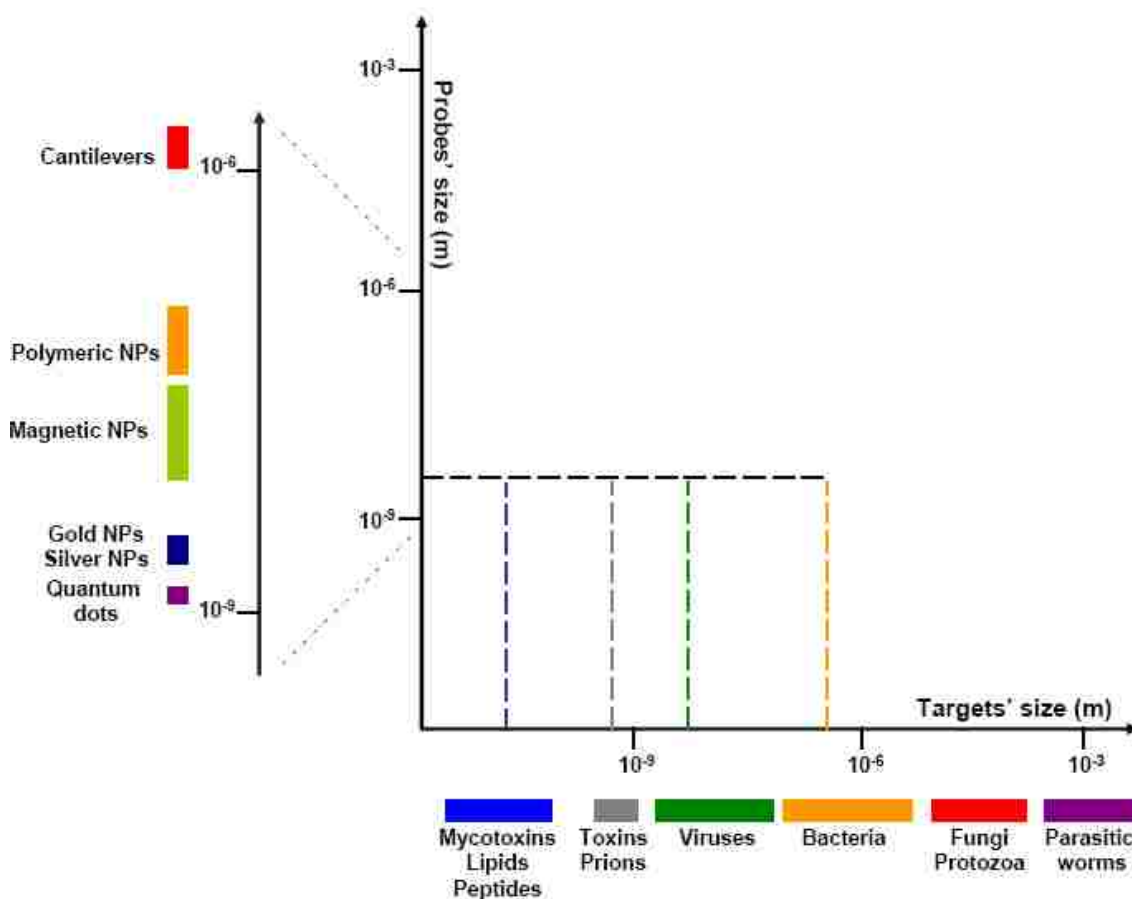
Figure 1. Size distribution of widely used nanosystems in comparison with the most common types of infectious disease agents.
A particular nanoparticle (represented by a black horizontal dashed line) could interact with targets of various sizes, such as peptides, toxins, viruses and bacteria (blue, grey, green and orange dashed lines, respectively). In this particular case, the nanoparticle has a size of 100 nm, whereas virulence factors and disease markers are smaller (e.g. lipids, peptides, DNA, toxins), and pathogens can be of roughly equal (e.g. most viruses) or bigger size than the nanoparticle (e.g. bacteria, fungi).

Gold nanoparticles

Gold nanoparticles (Au-NP) can be synthesized either in an aqueous or organic environment[27]. Conventional techniques for aqueous synthesis involve the reduction of AuCl$_3$ with trisodium citrate, followed by the addition of a capping agent to stabilize the Au-NP by introducing adequate electrostatic repulsion between individual particles to

keep them well dispersed in the medium[27]. Alternatively, organic-based Au-NP synthesis offers excellent control and improved size uniformity[27]. Surface chemistries of Au-NP can be controlled by grafting functionalized organic thiol molecules or thiol-containing polymers, as the gold surface exerts strong affinity towards sulfhydryl groups leading to the formation of relatively strong covalent bonds. Hence, further surface modification can be done simply by using thiolated functional molecules, facilitating conjugation of various probes, including antibodies and nucleic acids. Successful formation of Au NPs is associated with the presence of a surface plasmon band in the preparation's UV-vis absorbance profile. The surface plasmon band arises from the coherent existence of free electrons in the conduction band, due to the small particle size. The band shift depends on the particle size, chemical surrounding, adsorbed species on the surface, and dielectric constant[28]. Changes in the local dielectric constant of the nanoparticles by absorbed biomolecules or the biomarker-induced agglomeration of the nanoparticles cause plasmonic band shifts[28]. Hence, this unique characteristic of gold, as well as silver, nanoparticles allows the use of the surface plasmon band shifts changes for several diagnostic applications by recording the alterations in the UV-vis absorbance spectrum. Apart from absorption, gold nanoparticles were used as tags for the detection and quantification of numerous targets using fluorescence, Raman scattering, electrical conductivity, atomic and magnetic force techniques[23, 24].

Silver nanoparticles

Silver nanoparticles (Ag-NP) were first used as a new generation of antimicrobial agents to prevent infections[29]. Generally, these nanoparticles can be synthesized using methods yielding spherical, elongated (rod-shaped) or truncated (triangular)

nanoparticles[29]. Initially, silver seeds can be prepared by rapidly injecting 10 mM $NaBH_4$ into an aqueous solution of 10 mM $AgNO_3$ and 1 mM sodium citrate and aged for 1.5 h[29]. Spherical silver nanoparticles can be prepared by reducing an aqueous solution of $AgNO_3$ (1 mM) by adding silver seed solution and aqueous solution of sodium citrate, under boiling conditions until the color of the solution becomes greenish-yellow[29]. Similarly, the elongated and triangular shaped silver nanoparticles can be prepared by adding silver seed, 0.1 M ascorbic acid, 0.1 M CTAB and 1 M NaOH solution to the aqueous solution of $AgNO_3$ (10 mM) to accelerate particle growth[28, 30]. The *in situ* reduction of Ag^+ ions and introduction of surface functional groups can be achieved in one-pot reactions, using various biopolymers. Other than small reducing agents, such as sodium citrate and hydrazine hydrate, various functional polymers, including poly(acrylonitrile), poly(N-vinyl pyrrolidone), poly(vinyl alcohol), polyacrylic acid and polyacrylamide, were used for the reduction and surface coatings of the silver ions[31]. Hence, these functional Ag-NP can perform conjugation chemistries to connect various targeting ligands, such as proteins, antibodies, peptides, oligonucleotides and small molecules. Ag-NP exhibit a surface plasmon band, usually at 422 nm for spherical nanoparticles, which can be used for colorimetric detection and quantification of targets. Also, these nanoparticles can be used for the microscopic identification of targets using either high angle annular dark field (HAADF) or scanning transmission electron microscopy (STEM), and electrochemical approaches.

Quantum dots

Fluorescent quantum dots (Qdots) are semiconductors with unique optical properties when compared to conventional semiconductors, organic fluorescent dyes and proteins[24]. Qdots can be prepared using a variety of methods ranging from molecular beam epitaxy and electron beam lithography, yet colloidal synthesis is the most common technique for Qdots preparation. Specifically, in the case of hot solution phase synthesis, periodic group II and VI (CdSe, CdTe, ZnSe, etc) or III and V elements (InP, InAs, etc), are dissolved in a solution with a stabilizing agent or polymer. Thus during the synthesis procedure, these salts enter into a phase where they associate, leading to the formation of core-shell Qdots capped with either a polymer or a stabilizer[32]. Furthermore, a simple 'cap exchange' approach can be used to anchor for instance bifunctional mono- or di-thiols to the Qdot surface, where the remaining functional end-group can be used for further functionalization and conjugation. Mechanistically it is the band-gap that determines in which frequencies the Qdot will respond to. Hence, by engineering their band-gap (such as by changing their size), Qdots can emit light in different wavelengths upon excitation, having broad and diverse applications. For instance, simply by modulating their size, Qdots can be excited at a given wavelength and have tunable emission from the ultra-violet (UV) to the near infra-red (NIR) region. Apart from being tunable, Qdots are highly bright and extremely photostable, making them suitable for various biomedical applications, such as sensing and detection of biomarkers, immunolabeling of cells and tissues, detection of cancer *in vitro* and *in vivo*[33-37]. Qdot-based FISH (Fluorescence In Situ Hybridization) probes have been widely used for the detection of the Y-chromosome in fixed human sperm cells[38]. Furthermore, Qdot-FRET-

based nanosensors mediated the ultrasensitive detection of low concentrations of target DNA in the diagnosis of genetic diseases[39, 40].

Fluorescent polymeric nanoparticles

Polymeric nanoparticles are easily prepared using a linear or branched polymer that promotes the encapsulation of a fluorophore within the nanoparticle's cavity or hydrophobic microdomains[41-43]. Several synthetic routes can be utilized yielding stable monodispersed nanoparticles in aqueous media. The resulting nanoparticles, such as fluorescent silica ones, can be filtered and concentrated. Since the presence of the polymeric coating protects the fluorophore, these nanoparticles are stable under diverse conditions[41-43], surpassing organic dyes in photostability and versatility. Additionally the presence of functional groups on the polymer coating, including amines, carboxylic acids and esters, confers facile attachment of probes. Surface functionalization and targeting can be achieved via numerous conjugation chemistries, including "click" and carbodiimide[44]. Detection is mainly achieved with the use of a fluorescence spectrometer, flow cytometer, and fluorescence-recording microtiter plate reader[41-43].

Nanochips and Nanoarrays

Nanochips can be prepared for the fast identification of biomolecules, using Au-NP or Ag-NP supported on thin silicon layers[23, 24]. Following sample incubation, the nanochips are subjected to different procedures in order to achieve signal amplification. Due to their small size and use of currently available instrumentation, nanochips can screen samples in a high-throughput format requiring minute sample volumes[23, 45].

Furthermore, apart from quantifying a target, nanochips can identify if proteins undergo post-translational modifications, such as proteolytic cleavages and phosphorylation, using matrix-assisted laser desorption/ionization-time-of-flight mass spectrometry (MALDI-TOF-MS)[23].

In addition to nanochips, nanoarrays have been used to further expand the emerging field of DNA arrays[23, 24, 46]. Through different manufacturing approaches, nanoarrays have been fabricated using inkjet printing, electrochemistry, microfabricated surface patterning, or photolithography with either pre-assembled masks or micromirror-based apparatus[23]. Specifically, the nanoarray can be constructed on diverse surfaces, such as silicon, silanes, hydrogels, metallic and polydimethylsiloxane (PDMS), among others. Hence, detection of a target can be achieved with atomic force microscopy (AFM), surface plasmon resonance, optical waveguides, nanowires, microfluidics and electrical current detectors. The nanoarray can utilize various probes, including antibody, nucleic acid and small molecule, which can be either deposited in 1 – 30 µm droplets or via fluidics-enhanced molecular transfer operation[46]. In addition to these entities, colloids and Qdots can be further applied leading to the construction of multiplexed nanoarrays capable of screening minute samples in large libraries of potential pathogenic agents or therapeutics.

Fiber-optic-based biosensors

For the rapid detection of analytes, researchers have modified traditional ELISA plate assays, developing sandwich-format fiber-optic-based platforms[47-49]. Immobilization of a capturing moiety (antibody, aptamer, ligand) to a fiber optic or capillary tube mediates the capturing of the molecule of interest, whereas a secondary

probe (i.e. antibody) conjugated to a fluorophore facilitates target detection. Following fluorophore excitation, the emitted light is recorded by portable instrumentation, which can quantify the target based on the fluorescence intensity[48].

Cantilever-based arrays

Due to their high sensitivity, cantilevers can be used for the detection of molecular targets. These cantilevers resemble AFM tips and can be decorated with nucleic acids, small molecules and antibodies[23, 24]. Upon binding of a target, the cantilever deflects a couple of nanometers, facilitating detection. Since the deflection is proportional to the amount of target binding, cantilever-based arrays are quantitative[23, 24]. Advantages of these arrays include the absence of any enzymatic amplification steps such as PCR, the detection of nucleic acids and proteins without the need of labels (i.e. fluorophores), and the ability to be used in microfluidic setups.

Magnetic nanoparticles

Magnetic nanoparticles have been used for a long time in the clinic and the molecular biology laboratories[23, 24]. For instance, superparamagnetic iron oxide nanoparticles, composed of a magnetite/maghemite core, have been utilized as contrast agents for magnetic resonance imaging (MRI). Also, magnetic nanoparticles conjugated to antibodies have been used for the immunomagnetic separation of nucleic acids, proteins, viruses, and cells[23, 24]. Iron oxide nanoparticles are primarily synthesized via water-based protocols, involving the alkaline precipitation of iron salts. To enhance water stability and add surface functionality, often times the iron oxide core is coated with polymers, such as dextran, polyacrylic acid and silica. Further surface modification can

15

facilitate the addition of functional groups, such as amino and carboxylic acids, making subsequent conjugations easy. Hence, iron oxide nanoparticles can carry diverse ligands, such as peptides, small molecules, proteins, antibodies and nucleic acids. Iron oxide nanoparticles have been used for the identification and quantification of several targets, including mRNA, DNA, and viruses[50-52]. Furthermore, enzymatic activities were monitored with these nanoparticles[53, 54]. Detection with magnetic nanoparticles can be achieved with the use of magnetometers or superconducting quantum interference device (SQUID), which record alterations in the magnetic properties of the particles upon molecular interactions with a target[55-57]. Also, detection and quantification can be accomplished with magnetic relaxometers and magnetic resonance imaging (MRI), by monitoring the changes in the spin-spin relaxation time (T2) of the solution's water protons due to nanoparticle association with a target[50, 52, 58].

CHAPTER II: DEVELOPMENT OF MRnS FOR BIOMEDICAL APPLICATIONS

Introduction

Iron oxide-based magnetic nanoparticles have been widely used in a variety of biomedical applications, including magnetic separation, magnetic resonance imaging, hyperthermia, magnetically-guided drug delivery, tissue repair, and molecular diagnostics[50-52, 59-63]. For most applications, a polymeric coating is needed to improve the nanoparticles' aqueous stability, biocompatibility and conjugation properties. For instance, dextran-coated iron oxide nanoparticles have been successfully used as magnetic resonance imaging (MRI) contrast agents, due to their strong ability to dephase water protons in surrounding tissue, which results in a decrease in the MRI signal[50]. An interesting feature of these nanoparticles is that the dextran coating can be crosslinked and functionalized with amino groups to facilitate the conjugation of targeting ligands for MRI and *in vitro* diagnostics applications[64]. Generally, current synthetic procedures for polymer-coated iron oxide nanoparticles involve the formation of the iron oxide core in the presence of the polymer that serves as a stabilizer and capping agent in an alkaline solution[65]. Under these *in situ* conditions, the nature, quality and amount of the polymer modulate the nucleation, growth and size of the newly formed iron oxide nanocrystal. Hence, understanding the polymer's potential role on the iron oxide nanoparticles' intrinsic properties during a stepwise synthesis may be equally important, as it could potentially facilitate the formation of application-tailored iron oxide nanoparticles.

Considering these, we optimized the water-based synthesis of polymer-coated iron oxide nanoparticles (IONP) and investigated how their properties are affected by their polymeric coating. Among the physical parameters studied were the size, shape, and spin-spin relaxivity (R2). Lastly, we examined whether the nanoparticles' polymeric coating could modulate their enzyme-mimicking activity, paving the road for nanoparticle-based immunoassays.

Materials and Methods

Reagents.

Iron salts ($FeCl_2$. $4H_2O$ and $FeCl_3$. $6H_2O$), polyacrylic acid (1.8 kDa), Concanavalin A and TMB (3,3',5,5'-Tetramethylbenzidine) were purchased from Sigma. Dextrans (10 kDa) were received from Amersham Biosciences/Pharmacosmos and Sigma. TEOS: tetraethylorthosilicate (Fluka), APTS: 3-(amino-propyl)triethoxysilane (Aldrich) and THPMP: 3-(trihydroxysilyl)propylmethyl-phosphate (Gelest Inc.) were used as received from the suppliers.

Synthesis of iron oxide nanoparticles.

An acidic solution of iron salts containing 0.203 g $FeCl_2$. $4H_2O$ and 0.488 g $FeCl_3$. $6H_2O$ in HCl solution (88.7 µl 12 N HCl in 2 ml water) was mixed with ammonium hydroxide (830 µl NH_4OH in 15 ml DI water) under stirring conditions. The reaction mixture turned black instantaneously, and after 30 seconds of stirring dextran (5 g in 10 ml DI water) was added to yield dextran-coated IONP. Likewise, for the synthesis of polyacrylic-acid-coated IONP, polyacrylic acid (820 mg in 5 ml DI water) was added to the iron salt solution 30 seconds after addition of ammonium hydroxide. For silica-coated IONP, a

18

TEOS-THPMP-APTS solution was added (6180 µl THPMP, 2680 µl TEOS, 670 µl APTS) 20 seconds after initiation of the iron oxide nanocrystal formation. The resulting solutions were stirred for 1 hr and then centrifuged at 13,000 rpm for 30 minutes to remove large particulates. Finally, the supernatant was collected, washed several times with distilled water and concentrated through an Amicon 8200 cell (Millipore ultrafiltration membrane YM – 30 k)..

Characterization.

The particles were characterized using HRTEM (FEI TECNAI F30), a PDDLS CoolBatch 40T instrument with the Precision Deconvolve 32 software, and a Perkin-Elmer Spectrum 100 FT-IR spectrometer using samples spotted on plastic cover slips. T2 was measured using a Bruker Minispec mq20 NMR analyzer operating at 0.47 T.

Kinetic assay of iron oxide nanoparticles' peroxidase activity.

The peroxidase activity of the IONP was evaluated via steady-state kinetic assays at room temperature. Specifically, serial dilutions of TMB were prepared in citrate buffer (pH 4), and 100 µl aliquots were dispensed in a 96-well plate. Subsequently, aliquots of the polymer-coated IONP, having equal iron concentrations (2 µg per ml), were added to the corresponding wells. After addition of 25 µl H_2O_2 (30%), each well's absorbance was recorded at 652 nm, using the time-scan mode of a Synergy HT microtiter plate reader (Biotek). The kinetic parameters were determined via the Michaelis-Menten equation:

$$v = V_{max} \times [S]/(K_m + [S]),$$

where v is the initial rate of reaction, V_{max} is the maximum rate of reaction, [S] is the substrate's concentration, and K_m is the Michaelis constant.

Results

In our first set of experiments, we optimized the synthetic protocol, determining the optimal addition time of the polymer. Our water-based synthetic protocol involved an acid-base reaction between an acidic solution of iron salts and a basic solution of ammonium hydroxide. Upon mixing, the resulting solution became alkaline (pH = 9.0), facilitating the formation of iron oxide nanocrystals. This initial formation of nanocrystals can occur either in the presence (*in situ*) or absence (stepwise) of a polymer. Since most synthetic procedures that yield stable and monodispersed nanoparticles use an *in situ* approach, we opted to follow this approach first, yet obtaining spherical nanocrystals of 20 ± 5 nm in diameter with poor R2 relaxivity (< 1 mMs^{-1}).

As this poor relaxivity contrasts with the relaxivity obtained with published *in situ* procedures ($60 - 100$ mM^{-1}s^{-1}), we investigated if a stepwise approach could result in larger iron oxide nanocrystals with improved R2 relaxivities. In this approach, the polymer solution was added at a particular time after initiating the nucleation of the iron oxide crystals. Following this approach, we obtained polymer-coated nanoparticles with different sizes, but comparable R2 relaxivities (Table 2). Notably, silica- and PAA-coated IONP had diameters of 145 and 60 nm respectively, and intriguingly high spin-spin relaxivities (R2 > 200 mM^{-1}s^{-1}) (Table 2). Therefore, as these nanoparticles have readily available surface functional groups (amines for silica and carboxylic acid for PAA), their

conjugation could be facile and allow the formation of MRnS libraries with diverse

probes.

Table 2: Physical properties of various preparations of polymer-coated IONP.
(Dextran: 10 kDa dextran, Silica: tetraethylorthosilicate (TEOS), and PAA: 1.8 kDa poly(acrylic) acid)

Polymer-coated IONP			
Coating	Dextran	Silica	PAA
Size (nm)	135	145	60
R2 ($mM^{-1}s^{-1}$)	> 200	225	206
Conjugation	Difficult	Easy	Easy

Next, the presence of dextran on the IONP's surface was confirmed through

clustering experiments with Concanavalin A (Con A). Specifically, the presence of

dextran on nanoparticles can be identified via the Con A-induced nanoparticle clustering,

due to the strong affinity and multivalency of Con A towards carbohydrates, such as

dextran[69, 70]. Dynamic light scattering (DLS) experiments revealed a time-dependent

increase in particle size distribution upon Con A addition, due to formation of

nanoparticle assemblies (Figure 2A). Most importantly, a fast and reproducible change in

the T2 relaxation time was observed (Figure 2B), not only indicating the association of

dextran with the nanoparticle, but also hinting the potential use of the dextran-coated rod-

shaped IONP as magnetic relaxation nanosensors (MRnS). FT-IR experiments (Figure

2C) further confirmed the presence of the characteristic dextran peaks on these

nanoparticles.
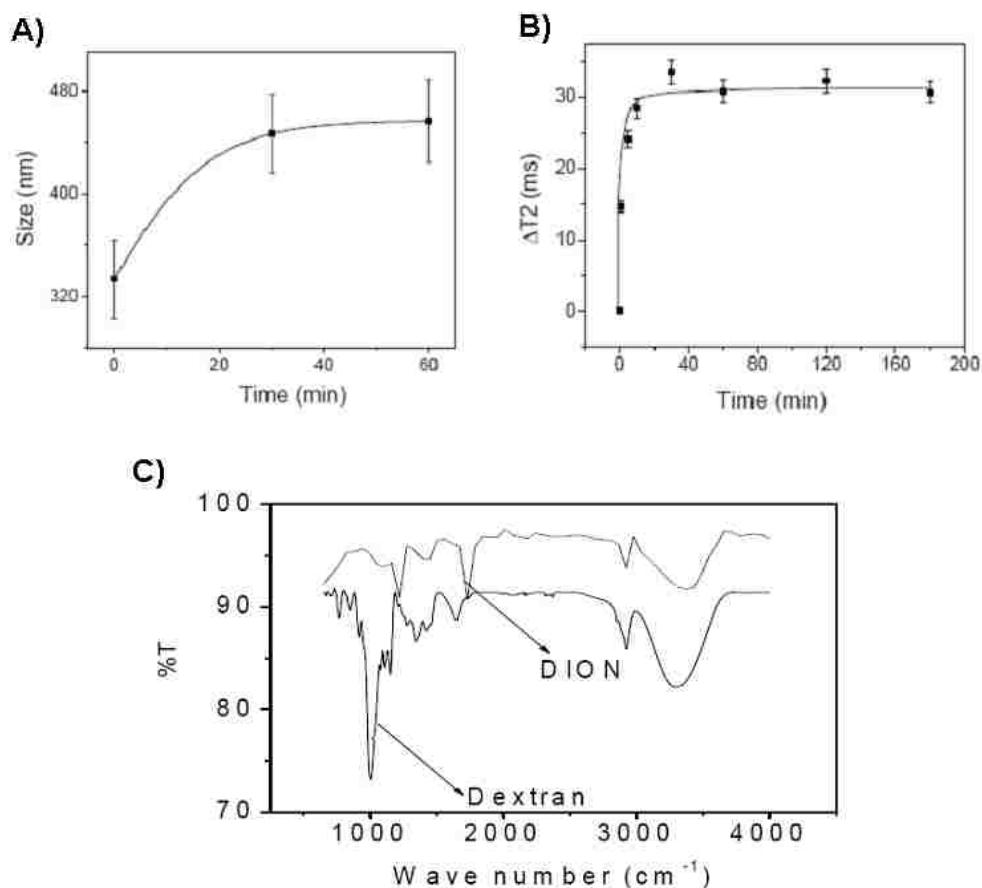
Figure 2: Confirmation of the presence of dextran on IONP.
A) Dynamic-light-scattering-based and **B)** T2-relaxation-based monitoring of the Concanavalin A (Con A)-induced clustering of the nanoparticles (200 µL, 2 µg Fe/mL) after treatment with 10 µL Con A ([Con A]$_{in}$ = 1 µg/µL in 1X PBS). **C)** Fourier Transform infrared spectroscopy of dextran and dextran-coated IONP (DION).

One of the most interesting properties of nanomaterials is the enhanced catalytic activities that some of these materials exhibit. Recently, the peroxidase activity of IONP has been reported[71, 72]. Therefore, we decided to investigate if our IONP possess similar peroxidase activity. In these experiments, we incubated the IONP (2 µg Fe/ml) with the peroxidase-sensitive dye 3,3',5,5'-tetramethylbenzidine (TMB, 0.4 mM), which develops a blue color upon oxidation in the presence of hydrogen peroxide and a peroxidase.

Results showed that the dextran-coated IONP possess peroxidase activity as judged by their ability to oxidize TMB in the presence of hydrogen peroxide within 30 minutes (Figure 3A). The observed peroxidase activity of the IONP is pH-dependent, as no oxidation of the dye is observed at pH 7 or even in DMF-water mixtures (Data not shown). These results are in line with those recently reported, however it is worth mentioning that our nanoparticles are more magnetic than those previously used[71]. Furthermore, we determined the kinetic parameters of the dextran-coated IONP's peroxidase activity, utilizing TMB as the peroxidase substrate. Specifically, a Michaelis constant, K_m of 0.5 mM and a maximal reaction velocity (V_{max}) of 11.6×10^{-8} M/s were obtained from the corresponding Lineweaver-Burk plot (Figure 3B). Notably, these nanoparticles' V_{max} is higher than that of previously reported iron oxide nanoparticles and horseradish peroxidase (20% and 33% respectively), while having TMB as the peroxidase substrate[71]. Furthermore, their affinity towards TMB is 300 times higher than that of previously reported nanoparticles, which had a (K_m) of ~ 150 mM[71]. Taken together, these data demonstrate the enhanced intrinsic peroxidase activity of our dextran-coated nanoparticles. Subsequently, we investigated if the polymer plays a role in the IONP's peroxidase activity, as previous reports demonstrated that the stabilizer or capping agent affects the physiochemical properties of nanomaterials[73,74]. Hence, similar characterization of the silica- and PAA-coated IONP indicated that these nanoparticles exhibited peroxidase-mimicking activity, yet with significantly lower V_{max} and K_m, suggesting the role of the polymeric coating in the modulation of these parameters (Table 3).
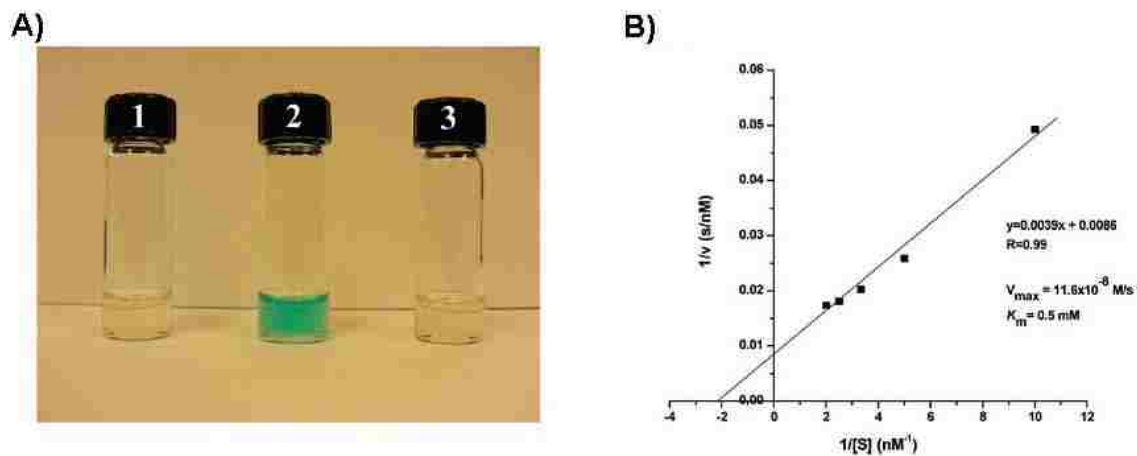
Figure 3: Peroxidase-like activity of dextran-coated IONP.
A) Visual confirmation. TMB in citrate buffer (pH 4) was treated with H_2O_2 (**1**) only as a control, with H_2O_2 and dextran IONP (**2**), and with only dextran IONP and no H_2O_2 (**3**). **(B)** Kinetics of peroxidase activity of dextran-coated IONP prepared from a 10 kDa dextran.

Table 3: Modulation of the IONP's peroxidase-mimicking activity by the polymeric coating.

Polymeric coating	V_{max} (M/s)	K_m (mM)
Dextran	12×10^{-8}	0.50
Silica	1×10^{-8}	0.15
PAA	4×10^{-8}	0.10

Conclusion

➢ We have optimized the stepwise synthesis of various polymer-coated IONP, including silica- and PAA-coated nanoparticles.

➢ The nanoparticles exhibited high R2 relaxivities and demonstrated enhanced peroxidase-mimicking activity, with improved K_m outperforming previously reported iron oxide nanoparticles.

➢ Silica- and PAA-coated IONP can be used as building blocks for the development of sensitive MRnS, due to the presence of readily available functional groups on their surface.

➢ Dextran-coated IONP may be used as carbohydrate MRnS utilizing their Con A-induced clustering.

Discussion

Iron-oxide-based magnetic nanoparticles are among the most widely used nanoparticles in the clinic and the lab. Apart from being used as MRI contrast agents and effective vehicles in immunoseparation assays, iron oxide nanoparticles have been recently used as sensitive probes for molecular recognition events. Despite their enhanced sensitivity and their numerous biodiagnostics applications, little effort has been made to the optimization of these nanoparticles' properties. As most contemporary synthetic protocols utilize an *in situ* methodology, we hypothesized that an alternative stepwise approach may facilitate the formation of robust IONP with improved R2 relaxivities and peroxidase-mimicking activities. Plausibly, a stepwise approach should have facilitated

the effective nucleation initiation process and uniform crystal growth, which can be successfully arrested by the addition of the polymer leading to the formation of monodispersed preparations.

Utilizing a facile, aqueous-based and room temperature stepwise synthesis protocol, we prepared dextran-, silica- and PAA-coated IONP. The as-synthesized nanoparticles had different sizes, but all exhibited enhanced R2 relaxivities and peroxidase-like enzymatic behavior. Hence, this indicates that a stepwise approach is advantageous over an *in situ* methodology, primarily due to the improved nanoparticle formation dynamics that the former method incorporates. Since the silica- and PAA-coated IONP exhibit high R2 relaxivities and carry native functional groups on their surface, these nanoparticles could be ideal for the formation of MRnS libraries by easily conjugating biomolecules to the nanoparticles.

Overall, we have demonstrated that application-tailoring of the IONP's properties can be modulated by the nanoparticles' polymeric coating. It is anticipated that the dextran-coated iron oxide nanoparticles, as well as the other polymer-coated IONP, may find use in numerous applications, ranging from magnetic-relaxation-based sensing and diagnostics to hyperthermia, and from MR imaging to catalytic oxidations. Lastly, the fabrication of devices and nanocomposites with dual magnetic and catalytic activities is foreseen.

CHAPTER III: IDENTIFICATION OF BACTERIA VIA BIOMARKER-SPECIFIC MRnS

Introduction

Bacterial infections are the fifth cause of mortality in the US, and their economic impact on the industrial, agricultural and healthcare sectors is significant[4]. Headlines in the press about the presence of enterrohemorrhagic *E. coli* O157:H7 in tainted produce, the identification of the extremely cytotoxic Subtilase AB_5 toxin in *E. coli* O113:H21, the aftermath of the *B. anthracis* attacks in 2001, and the recent identification of drug resistant *Mycobacterium tuberculosis* (XDR-TB) in Africa sparked public concern. Therefore, the need for developing fast, sensitive and reliable detection methods for bacteria in food, environmental and clinical samples is crucial in order to safeguard public health. Traditionally, the presence of a bacterium is detected microscopically, usually after growth in culture. Confirmation is based on growth patterns in various media and biochemical tests. These methods, although highly specific, have some drawbacks. First, they usually take more than 24 hours and lack sensitivity due to the amount of bacteria needed, whereas not all microorganisms can grow in culture. More recently, other methods involving polymerase chain reaction (PCR) and fluorescent immunoassays have been developed. However, despite their enhanced sensitivity and specificity, these methods are costly, time consuming and need to be performed by trained and experienced personnel. Thus, developing assays for faster and sensitive identification of bacteria at multiple levels is critical.

Nanotechnology offers an attractive alternative for the identification of diverse molecular targets *in vitro* and *in vivo*, requiring smaller samples and less preparation time, without compromising sensitivity [24, 33, 75, 76]. Recently, superparamagnetic iron oxide nanosensors have been designed to quantify biomolecular targets in cell lysates and tissue extracts, demonstrating high sensitivity[50-52]. The principle underlying the detection mechanism of these nanosensors is based on their ability to switch from a dispersed to a clustered (or assembled) state upon target interaction, with a concomitant change in the spin-spin relaxation time (T2) of the solution's water protons. Based on changes in T2 (ΔT2) various molecular targets, such as nucleic acids (DNA and mRNA), proteins and even viruses have been detected. These targets have in common the fact that they are smaller (e.g. DNA and proteins) or of equal size (e.g. virus) to the nanoparticles. However, the use of superparamagnetic nanoparticles for the detection of larger biological targets, such as a bacterium in solution, has not been examined before. We hypothesized that the presence of multiple bacterial epitopes should compensate for the size difference between the probe and the target, promoting nanoparticle assembly on the bacterial surface and consequently resulting in a dose-dependent change in ΔT2 (Figure 4). It was also hypothesized that the lower the number of bacteria in the solution, the higher the ratio of nanoparticles available to bind and self assemble on the surface of the bacterium, resulting in higher values of ΔT2 (Figure 4). As the number of bacteria in solution increases, it was expected that the resulting higher number of bacterial epitopes will compete with the available number of nanoparticles in solution, therefore causing the nanoparticles to bind to the bacteria in a more dispersed-like state (Figure 4). Such a nanoparticle-based bacteria detection system would be highly sensitive, particularly at

low target concentrations. Also, we reasoned that MRnS, being part of a homogeneous assay, could be able to detect bacteria at the organism and genomic levels via a single methodology and instrumentation, without the need of multiple protocols and instruments. Furthermore, apart from multilevel confirmation, achieving specific and sensitive detection is critical whenever antibodies cannot differentiate between virulent and avirulent strains, thus relying on genetic markers. Additionally, the abundance, stability and quality of epitopes can affect a microorganism's detection, whereas DNA-based assays have the ability to circumvent these problems, providing important clinical information usually with lower cost.
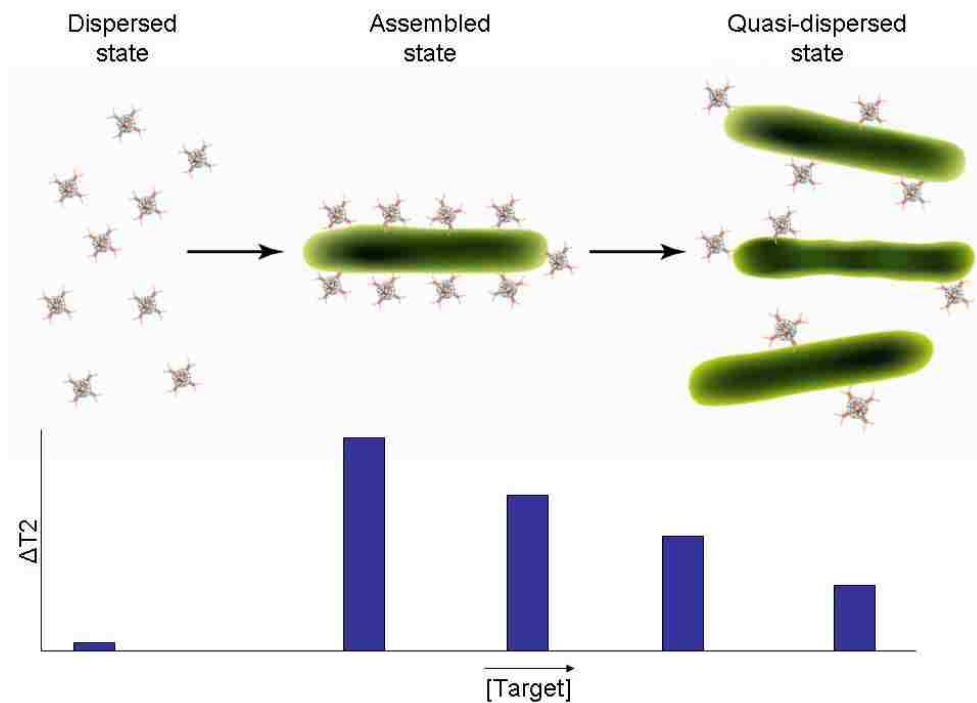
Figure 4: Proposed detection mechanism of bacterial targets using spherical surface-marker-specific MRnS.
Dispersed nanoparticles in solution self-assemble on the surface of a bacterial target inducing large changes in T2. As the number of bacteria increases, the number of nanoparticles interacting per target decreases, resembling a more dispersed-like state with concomitant smaller changes in T2.

29

Materials and Methods

Bacterial cultures, isolates and homogenized tissue.

Lab strains of MAP and clinical isolates were grown in 12B* BACTEC bottles (Becton Dickinson, Franklin Lake, NJ, USA) as described[78]. Quantification of MAP grown in the BACTEC bottles was assessed with the BACTEC 460 TB Analyzer (Becton Dickinson). Heat-inactivation of MAP was performed by autoclaving the BACTEC bottle for 10 minutes. *Proteus vulgaris* #8427, *Staphylococcus aureus* #33862, *Pseudomonas aeruginosa* #27853, *Enterococcus faecalis*, *Escherichia coli* #8739, and *Serratia marcescens* were grown in culture tubes with nutrient broth, and bacterial growth was monitored spectrophotometrically. Heat inactivation of these bacteria was performed by autoclaving the culture tubes for 10 minutes. Upon inactivation, all bacterial stocks were placed in a Fisher Isotemp freezer (Fisher Scientific, Hampton, NH), until further use. Clinical isolates and tissue preparations from Johne's disease and healthy cattle were prepared and coded by an investigator unaffiliated with this study.

Preparation of MAP MRnS.

The MAP nanosensors were prepared using Protein G-coated magnetic nanoparticles as described[52]. Briefly, the Protein G nanoparticles were incubated with rabbit anti-*Mycobacterium avium* spp *paratuberculosis* (MAP) polyclonal antibody, which was raised and purified as described in literature[79]. Results from preliminary optimization experiments showed that formation of stable nanoparticle conjugates can be easily achieved by overnight incubation at 4 $^{\circ}$C of 1 µL of antibody with 2 µL nanoparticle preparation (1.04 mg Fe/mL) in a total volume of 1 mL 1X PBS, pH 8. These nanoprobes were stable at room temperature and 37 $^{\circ}$C, and no precipitation was observed. Whole

milk (Velda Farms, Plant #12293, Lakeland, FL) and 2% milk (Publix, Lakeland, FL) were stored at 0 – 4 ^{o}C, and were used prior to their expiration date. Blood from bacteremia-free Crl:CD(SD)IGSBR female rats (Charles River Laboratories) was stored at -20 ^{o}C. Clinical isolates and animal tissue were treated and handled according to institutional IRB regulations.

Sample preparation for MAP MRnS.

Serial dilutions of the bacterial stocks were performed after thawing the original stock, vortexing, and diluting it to the corresponding medium. Aliquots of the nanoparticle suspension were mixed with the sample in eppendorf tubes, and a micropipette was used to homogenize. With a Pasteur pipette, the sample was transferred to a relaxometer tube. The samples were incubated at room temperature or 37 ^{o}C while into the relaxometer tubes. Incubation at 37 ^{o}C was performed utilizing an Eppendorf Thermomixer R (Eppendorf, Westbury, NY). For the specificity assay, 200 µL of nanoprobe solution (2 µg Fe/µL) were incubated with inoculated samples at 37 ^{o}C for 30 minutes. Quantification of MAP in whole milk was facilitated by incubating 200 µL nanosensors (2 µg Fe/µL) with inoculated sample at room temperature or 37 ^{o}C for 30 and 60 minutes. Under interference conditions ($\sim 10^9$ CFUs non-MAP organisms), MAP was quantified using MAP-specific nanoparticles (2 µg Fe/µL) and 10 µL inoculated whole milk, incubated at 37 ^{o}C for 30 minutes. T2 measurements were taken immediately or after a subsequent 45-minute cool-down to room temperature.

Preparation of IS900-specific MRnS.

The IS900 MRnS were prepared from propargylated PAA-coated iron oxide nanoparticles, utilizing literature available protocols[44]. Conjugation of the azide-terminated 15-bp AV1 oligonucleotide (5'-ATGTGGTTGCTGTGT-3') was achieved via "click" chemistry, as previously described[77]. Briefly, 400 µL propargylated IONP were resuspended in 1,100 µL $NaHCO_3$ buffer (0.1 M, pH 8.4). To this, we added 200 µL of 10 mM TCEP (tris(2-carboxyethyl)phosphane hydrochloride, Sigma) as a reducing agent. Twenty µL of 6.3 M AV1 were diluted in 80 µL $NaHCO_3$ buffer (0.1 M, pH 8.4) and added to the nanoparticle solution. The reaction was initiated with the dropwise addition of 150 µL Cu(II)-TBTA complex (tris(benzyltriazolylmethyl) amine, 10 mM, Sigma), which was previously prepared in DI water and t-butanol (9:1). The reaction was incubated at room temperature under continuous mixing for 3 hours, followed by overnight incubation at 4 °C under constant mixing. The resulting IS900 MRnS were dialyzed against DI water using a 6,000 – 8,000 MWCO membrane (Spectrum), followed by magnetic separation with an LS25 MACS column (Miltenyi). Determination of the MRnS's oligonucleotide concentration was achieved by monitoring the absorbance at 260 and 305 nm (background), using a Nanodrop 1000 spectrophotometer (Thermo Scientific). The MRnS were stored at 4 °C until further use.

Extraction of pure and crude bacterial DNA.

DNA was extracted from cultured bacteria in a class II biosafety cabinet, according to previously reported procedures[78]. One mL of bacterial cultures were aseptically transferred to microcentrifuge tubes, followed by centrifugation at 13,200 rpms. The resulting pellets were resuspended in 120 µL sterile TE buffer (10 mM Tris, 1 mM

EDTA, pH 8.0) and incubated in a dry heat bath at 100 ^{o}C. Samples without further processing were used as crude DNA extracts in MRnS and nPCR studies. In order to obtain pure bacterial DNA, after heating the samples, we placed them on ice for 15 minutes and then centrifuged them at 12,000 rpm for 10 minutes at 4 ^{o}C. The supernatants were transferred to Phase-lock gel tubes (Eppendorf), which were supplemented with 200 µL of phenol/chloroform/isoamyl alcohol (1:1:24 v:v, Acros). The tubes were centrifuged for 5 minutes (12,000 rpm, 4 ^{o}C), and the supernatants were precipitated using 400 µL 100% ethanol cooled to -20 ^{o}C. The precipitated DNA was washed, dried, and finally reconstituted in 50 µL sterile water. Pure and crude bacterial DNA was stored at 4 ^{o}C until further analysis, whereas spectrophotometric quantification of DNA content was achieved using a compact spectrophotometer (Nanodrop 1000, Thermo Scientific). Crude and pure DNA extractions from clinical isolates were similarly performed.

IS900 MRnS and nested PCR experiments.

Serial dilutions of bacterial DNA were prepared in TE buffer. For the relaxation-mediated experiments, 200 µL of the nanoparticle suspension (6 µg Fe/mL in 0.1 M phosphate buffer, 0.1 M NaCl, pH 7.4) were incubated with 1 µL of bacterial DNA or control (TE buffer). The samples were heated twice for 3 minutes at 95 ^{o}C. After this, the samples were transferred to relaxometer tubes and let cool down at room temperature, while taking relaxation measurements using a magnetic relaxometer. For the specificity assays using a synthetic target (AVT, 5'-TCCTTCGGCCATCCAACACAGCAACCACAT-3'), 1 µL of AVT (1.1 M) was added to the MRnS mycobacterial samples containing the same DNA concentration (3.5 ng/µL).

Similar DNA concentration was used for the specificity experiment utilizing other Gram positive and Gram negative bacteria and MRnS (3 µg Fe/mL). Nested PCR (nPCR) was performed as previously described[78], where the nPCR for the pure extracted MAP DNA was performed by an investigator unrelated to the MRnS study (Dr. George Ghobrial).

Measurement of proton relaxation times.

Spin-spin relaxation times (T2) were measured using a 0.47 T mq20 NMR analyzer (Minispec, Bruker, Germany). T2 values were obtained before and after addition of the sample, and through the time course of the study. All experiments and measurements were carried out in triplicate and data were expressed as mean ± standard error, unless otherwise denoted. The data were fitted on a sigmoidal curve, using Origin 7.5 (OriginLab, Northampton, MA).

Results

In our studies we used *Mycobacterium avium* spp. *paratuberculosis* (MAP), as our model organism. We selected this bacterium because its growth in culture is difficult and its identification with current methods is not easy[78-81]. In addition, MAP is the known pathogen causing Johne's disease in cattle, an economically devastating disease[82-84]. MAP-infected animals show severe intestinal inflammation, which can be degenerative, and the infection of healthy animals is high, resulting in the herd's annihilation to prevent further transmission[82-84]. Apart from causing disease in cattle, there is association between MAP and Crohn's disease in humans, as this microorganism has been isolated from the blood, breast milk and intestinal lesions of Crohn's disease patients[78-80, 85]. Herein, we demonstrate the development of MAP-specific nanosensors that can detect

MAP at the organism and genomic levels, even in complex media (whole milk and blood) with high specificity and sensitivity.

First, we prepared antibody-carrying MAP MRnS by conjugating anti-MAP antibodies[79] that recognize MAP surface epitopes to superparamagnetic iron oxide nanoparticles via Protein G, as described before[52]. These antibody-coated nanosensors were stable for months, after storage at 4 $^{\circ}$C. Preliminary studies in phosphate buffered saline (PBS) demonstrated that the nanosensors responded in a dose-dependent fashion upon addition of MAP. Formation of the bacterial-induced nanoassembly was detected upon addition of the bacteria, and this assembly was stable over a 3 hour-long incubation. For the first set of experiments in complex media, we compared the specificity of our nanosensors towards MAP, by adding spiked whole milk into 200 µL of MAP-nanosensors. The sample that had MAP alone (115 Colony Forming Units [CFUs] in 10 µL) had the highest change in T2, while the samples that had other bacteria (~10^6 CFUs in 10 µL) demonstrated minimal T2 changes (Figure 5). More importantly, the sample containing a mixture of bacteria, including MAP (77.5 CFUs in 10 µL), was identified as MAP-positive despite the presence of interference, underlying the specificity of our antibody-carrying nanosensors.
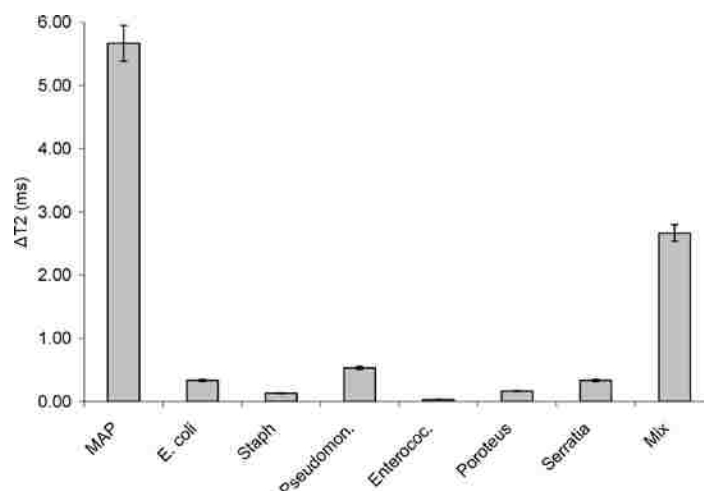
Figure 5: Specificity of MAP MRnS towards MAP and not other Gram positive and Gram negative bacteria.
MAP: *Mycobacterium avium* spp *paratuberculosis*, E. coli (*Escherichia coli*), Staph (*Staphylococcus aureus*), Pseudomon. (*Pseudomonas aeruginosa*), Enterococ. (*Enterococcus faeacalis*), Proteus (*Proteus vulgaris*), Serratia (*Serratia marcescens*) and Mix (MAP in the presence of the other six non-MAP species 50:50 v/v).

In addition, to verify if the observed changes in T2 were due to antibody-mediated interactions and not to non-specific nanoparticle aggregation, the bacteria were pre-incubated overnight with anti-MAP antibody before performing sensing experiments with the MAP MRnS. Results showed that the ΔT2 was abrogated in the bacterial sample pre-incubated with free MAP antibody (ΔT2 = 0.20 ms ± 0.1 ms), due to the inability of the MAP MRnS to bind to the bacterial epitopes. In contrast, a control bacterial sample that has not been pre-incubated with MAP antibody had significant T2 changes (ΔT2 = 8.90 ms ± 0.3 ms) at the same experimental conditions. To bolster the specificity of the MAP MRnS, milk samples spiked with 200 CFUs of MAP clinical isolates and other mycobacteria were screened, obtaining significant T2 changes in the MAP-containing samples as opposed to the other microorganisms (Figure 6). Furthermore, the T2 of the MAP MRnS was measured at 25, 30 and 35 °C, without any temperature-dependent

statistical differences. This implied that the nanoparticles' performance was steady in temperatures relevant to those at the points-of-care and that the observed changes in T2 were due to specific antibody-mediated interactions with the MAP bacterium.
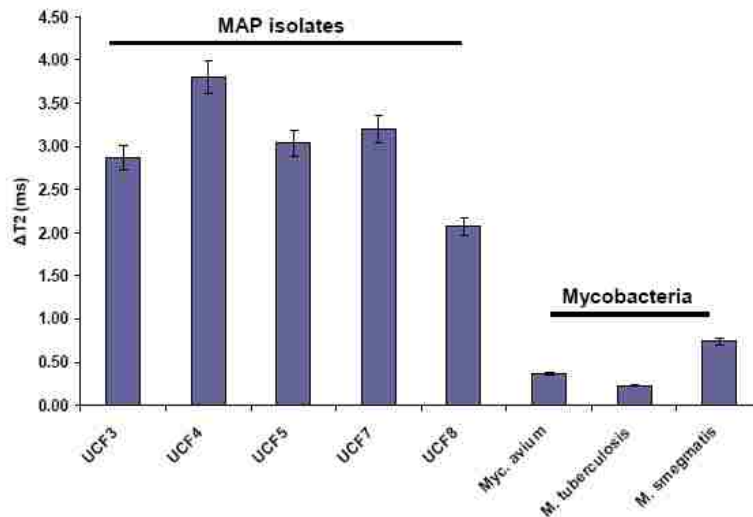
Figure 6: Specificity of MAP MRnS towards MAP isolates and not other mycobacteria.
UCF3, UCF4, UCF5, UCF7 and UCF8 represent different MAP clinical isolates. Myc. avium: *Mycobacterium avium*, M. tuberculosis (*Mycobacterium tuberculosis*), M. smegmatis (*Mycobacterium smegmatis*).

Next, we utilized the MAP MRnS for the detection of MAP in milk, as this bacterium was found in milk from Johne's disease cattle as well as in the breast milk of Crohn's disease patients[80]. Detection and quantification of MAP in milk was done by incubating MAP-spiked whole milk with MAP nanosensors. We found that the change in T2 was indirectly proportional to the MAP concentration (Figure 7), supporting our proposed detection model that predicted quasi-dispersion of the MRnS at higher target concentrations (Figure 4). Reliable quantification of MAP from 15.5 to 775 CFUs (R^2=0.93) was achieved with the MAP MRnS after a 30-minute incubation at room

temperature (Figure 7), whereas in control experiments using nanoparticles with no MAP antibody minimal changes in T2 were observed. It is interesting to note that the MAP MRnS could identify the bacterium in milk at low CFUs (<15.5 CFUs), even though they could not quantify it. This offers the ability to assess if a sample is MAP-positive or MAP-negative at low concentrations (< 15.5 CFUs). Using the same conditions and setup, MAP was quantified with good correlation in milk at 37 $^{\circ}$C. Notably, the described trend between ΔT2 and MAP's concentration was sustained, even after an hour-long incubation, regardless of the incubation temperature. Detection and quantification of MAP was achieved with high sensitivity in 2 % milk as well, after incubation at 37 $^{\circ}$C.
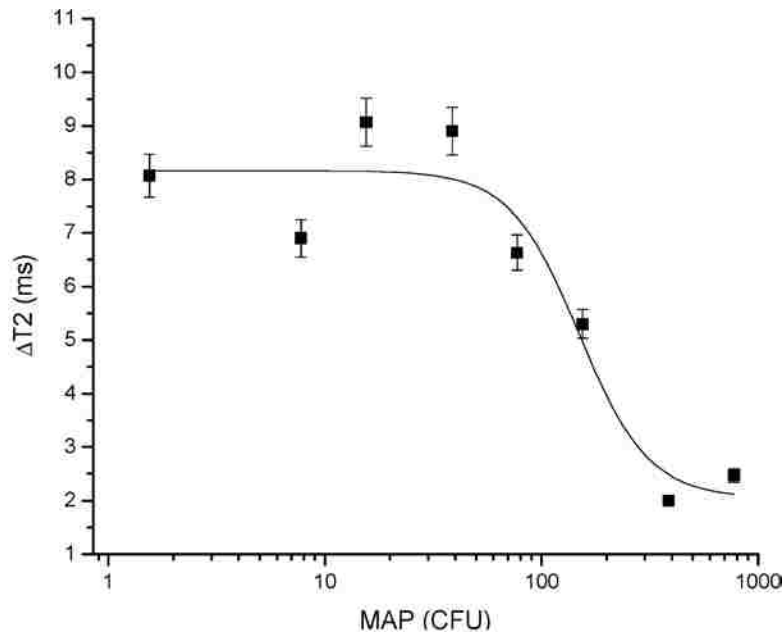
Figure 7: Concentration-dependent behavior of MAP-specific MRnS in whole milk at room temperature.

We next investigated if the presence of other bacteria would interfere with quantification of MAP. In these experiments, we quantified MAP in whole milk and in

the presence of six different bacterial species. After a 30-minute incubation at 37 °C, we were able to determine if a particular sample had the bacteria (MAP positive), and even determine the actual MAP concentration, having 15.5 CFUs as the assay's detection limit under these heavy interference conditions ($R^2 = 0.86$). However, when the incubation was followed by a 45-minute cool-down to room temperature, the correlation improved ($R^2 = 0.96$), due to the stronger binding and hybridization of the bacterium – nanoparticle system, yet the detection limit increased to 38.75 CFUs (Figure 8).
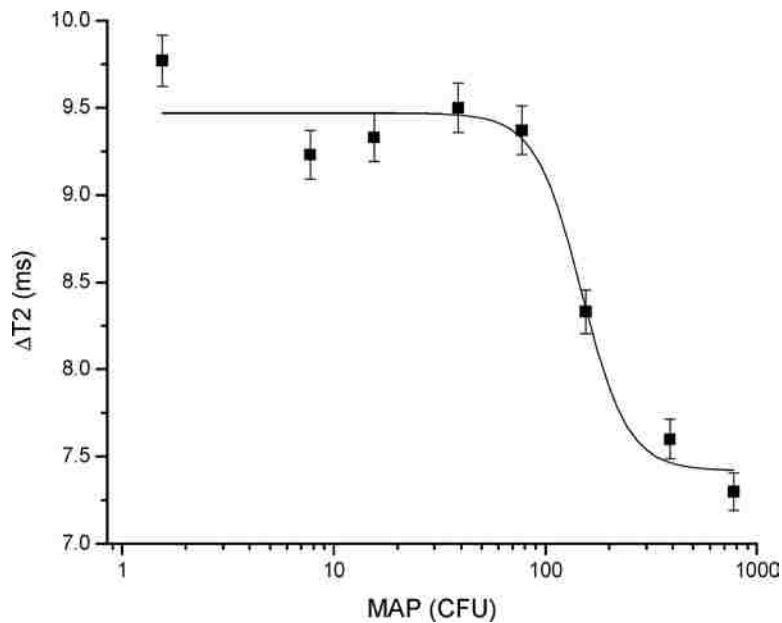
Figure 8: Quantification of MAP in whole milk using MAP-specific MRnS under interference conditions.

Since MAP has been found in the blood of Crohn's disease patients[78] and bacteremia (presence of bacteria in the blood) is a critical pathological state that requires fast detection and prompt medical attention, we performed experiments in blood samples.

In these experiments, we added 20 µL of whole blood containing increasing amounts of bacteria to 200 µL of the MRnS. Our MAP nanosensors were able to detect and quantify MAP in a concentration-dependent trend, in accordance to our hypothesis (Figures 9A and 9B). The assay was sensitive enough to detect MAP after a couple of minutes (Figure 9A), as well as after a 30-minute incubation at 37 ^{o}C (Figure 9B), making the assay relevant to clinical sample conditions.
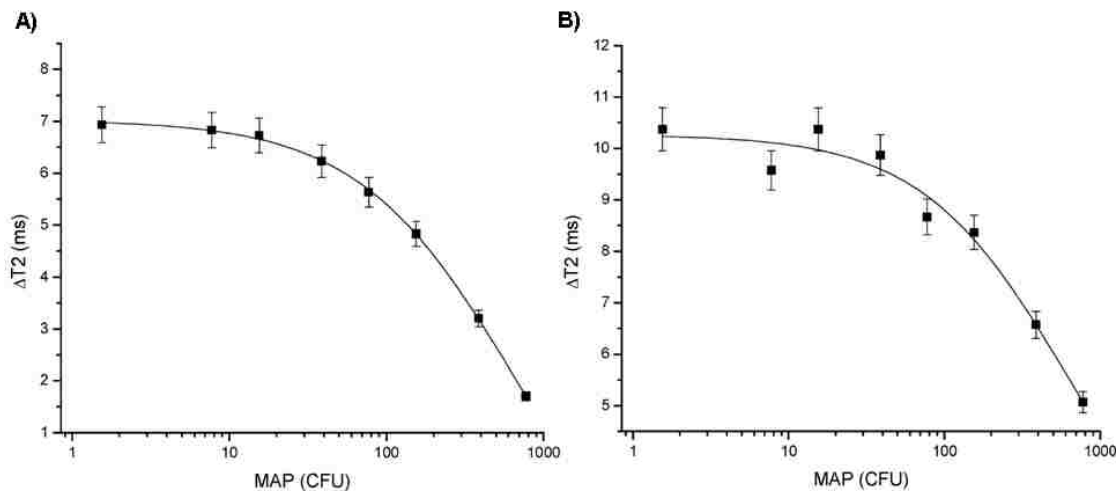
Figure 9: Quantification of MAP in blood using MAP-specific MRnS.
A) Upon sample preparation and **B)** after a 30-minute incubation at 37 ^{o}C.

In subsequent studies, we utilized the MAP MRnS for the screening of clinical isolates from Crohn's disease patients, as well as from two patients with ulcerative colitis and inflammatory bowel syndrome. In these studies, 10 µL aliquots of the isolates were added to the MAP MRnS followed by a 30-minute incubation at 37 ^{o}C. Interestingly, the MRnS provided a positive ΔT2 signal for all samples with clinical symptomology, whereas the sample from a healthy individual exhibited nominal changes in the T2 relaxation times (Figure 10). Independent confirmation of the MAP MRnS findings was

achieved by performing DNA extraction and nested PCR analysis for the detection of MAP's IS900. Hence, these findings are of major clinical importance, as the MAP MRnS were able to identify the presence of MAP in isolates within just 30 minutes, as opposed to the 2-day-long DNA extraction followed by a 6-hour-long nested PCR analysis.
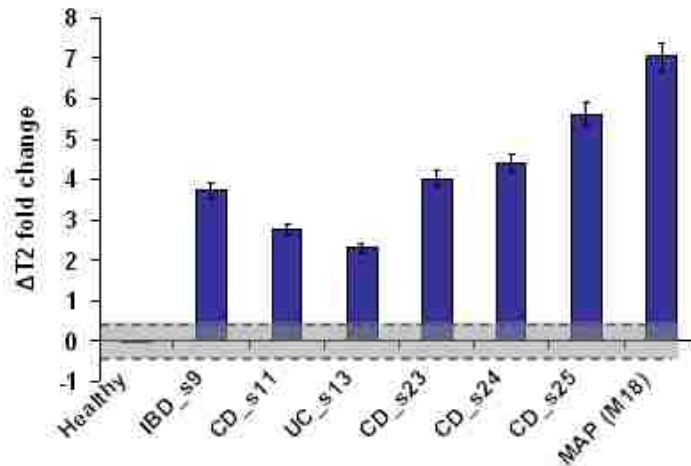
Figure 10: Detection of MAP in clinical isolates using MAP-specific MRnS.
Healthy: culture from a healthy individual, IBD: inflammatory bowel disease patient, CD: Crohn's disease patients, and MAP (M18): laboratory-cultured MAP serving as positive control.

Considering the promising MRnS results of clinical isolates and acknowledging the need for developing reliable methods for bacterial identification in food, we used the MRnS for the detection of MAP in homogenized tissues from Johne's disease cattle. Similar to our previous studies, 10 µL aliquots of various tissues were thoroughly resuspended in 200 µL of the MAP MRnS followed by a 30-minute incubation at room temperature. Small, yet reproducible, changes in the T2 relaxation times were recorded in the various tissues obtained from infected animals (Figure 11A), demonstrating that the MAP MRnS can quickly detect MAP in environmental and clinically relevant samples

via a positive/negative assay. To investigate if the 30-minute-long MAP MRnS results were valid, we performed longer incubations. Notably, after overnight incubation at 4 ^{o}C large changes in the ΔT2 were observed, where homogenized lymph nodes, inside and outside round had comparable levels of MAP as indicated by their similar ΔT2s (Figure 11B). The differences in the ΔT2 among the various samples after overnight incubation might be attributed to the fact that either the spatial concentration of MAP differs among the various tissues due to Johne's disease pathophysiology or due to the homogenization protocol not effectively facilitating the release of MAP from its potential intracellular residence, like macrophages. Overall though, these results indicate that MRnS can be used for the screening of various samples with minimal or no sample preparation, preventing epidemics and supporting clinical decision making.
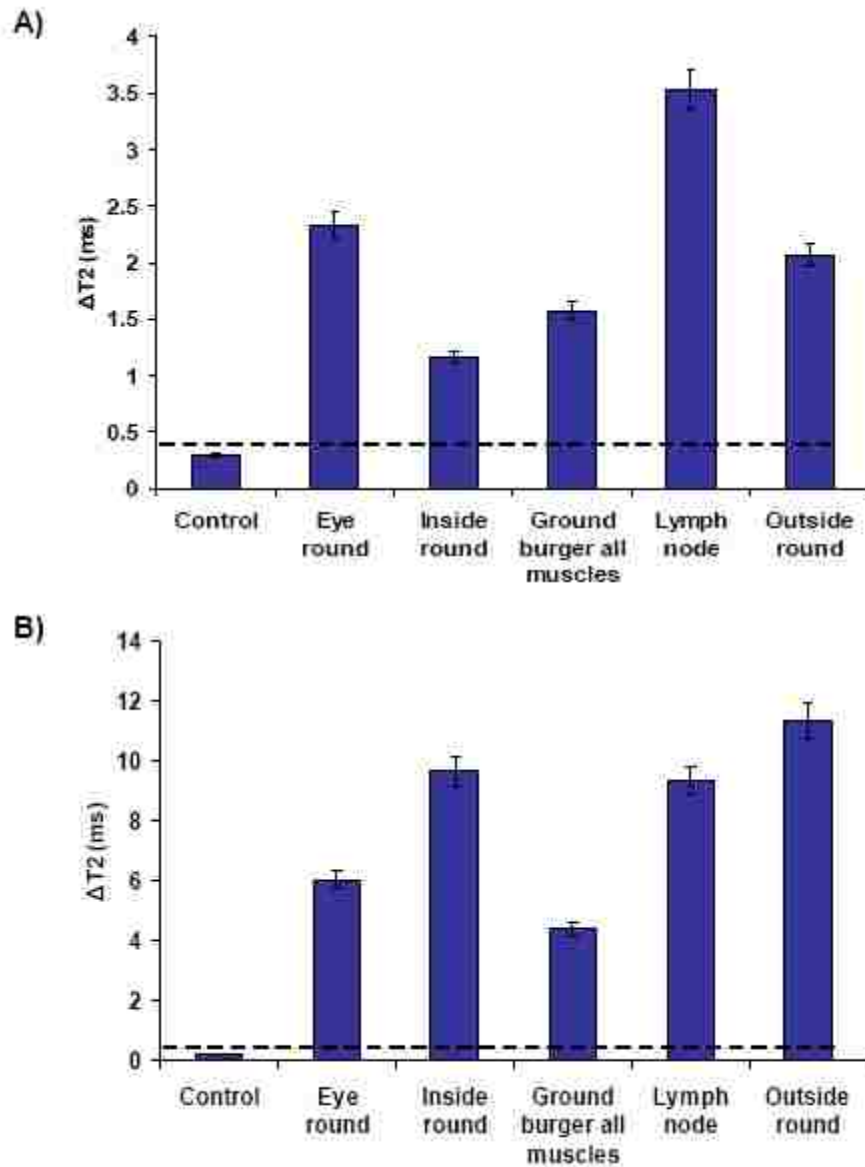
Figure 11: Detection of MAP in homogenized tissue from Johne's disease cattle using MAP-specific MRnS.
A) After a 30-minute incubation at room temperature the nanosensors identified MAP in homogenized tissues, but not in ground burger from healthy animals (control). **B)** Prominent T2 changed were observed after overnight incubation at 4 °C.

Figure 12: Synthesis of IS900-specific MRnS for the detection of MAP DNA.
"Click" conjugation of alkyne-functionalized PAA-coated IONP and azide-terminated AV1 oligonucleotide.

After establishing that the antibody-utilizing MAP MRnS could detect MAP at the organism level through surface epitope recognition, we prepared MRnS for the detection of MAP at the genomic level (IS900 MRnS), in order to potentially achieve multiplexed pathogen identification with even single pathogen sensitivity threshold. To recognize MAP's unique genomic IS900 element, the IS900 MRnS were synthesized using alkyne-carrying PAA-coated IONP as precursors for the "click" conjugation of the azide-terminated oligonucleotide AV1, which is complementary to IS900 (Figure 12). To examine the specificity of the IS900 MRnS, we prepared pure DNA extracts from various mycobacteria, including MAP. Aliquots of the extracts were incubated with the IS900 MRnS for two 3-min incubation rounds at 95 $^{\circ}$C, followed by cooling to room temperature. Within 30 minutes, results indicated that only samples containing MAP DNA exhibited a high ΔT2 signal, as opposed to the other mycobacterial samples (Figure 13). Interestingly, a mixture of MAP with other bacteria (50:50 v/v), resulting dilution of the MRnS was also identified as positive, and had a ΔT2 that was roughly half the ΔT2 of the sample containing only MAP. This indicates that the IS900 MRnS still exhibit their

44

property to alter the solution's T2 relaxation times in an iron-concentration-dependent fashion, and are not affected by the presence of complex biomolecules (mycobacterial DNA). Furthermore, to confirm the specificity of the IS900 MRnS, samples were incubated with MRnS and excess of a synthetic target (AVT) that was complementary to the nanoparticles' AV1 probe. This caused signal abrogation, due to the interaction between the MRnS and AVT preventing the MRnS – bacterial DNA association (Figure 13).
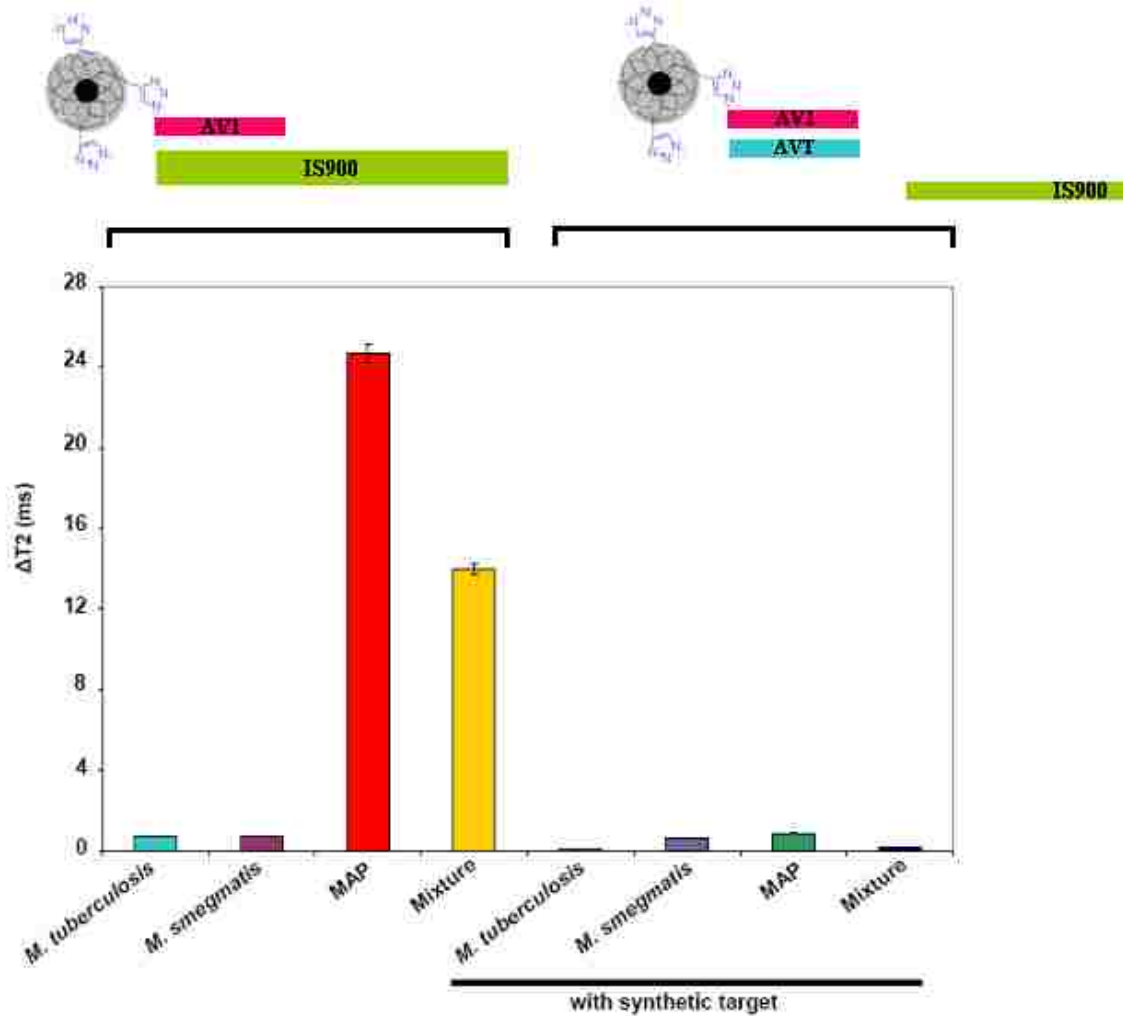
Figure 13: Specificity of IS900 MRnS towards MAP and not other mycobacteria.
Pure mycobacterial DNA extracts were subjected to two consecutive 3-minute incubations at 95 °C with the nanoparticles, followed by cooling at room temperature for 30 minutes. Mixture indicates a sample consisting of MAP DNA and *M. tuberculosis/M. smegmatis* 50:50 v/v. In the presence of a synthetic target (AVT) corresponding to a complementary sequence to AV1, the signal was abrogated.

Often times in clinical and environmental samples other microorganisms might be found, thus we examined if the IS900 MRnS could differentiate between MAP and some common Gram positive and Gram negative bacteria. Only the sample containing MAP yielded a high ΔT2, whereas the other bacterial DNA samples exhibited ΔT2 proximal to that of the sterile control (Figure 14). These data hint the potential use of the IS900

46

MRnS at the points-of-interest without requiring extensive sample preparation and bacterial isolation, due to the high specificity of the IS900 MRnS. Additionally, the findings that the diluted IS900 MRnS (Figure 14) had comparable $\Delta T2$ to that of the MAP mixture (Figure 13) further confirmed that the MRnS maintained their R2 relaxivity.
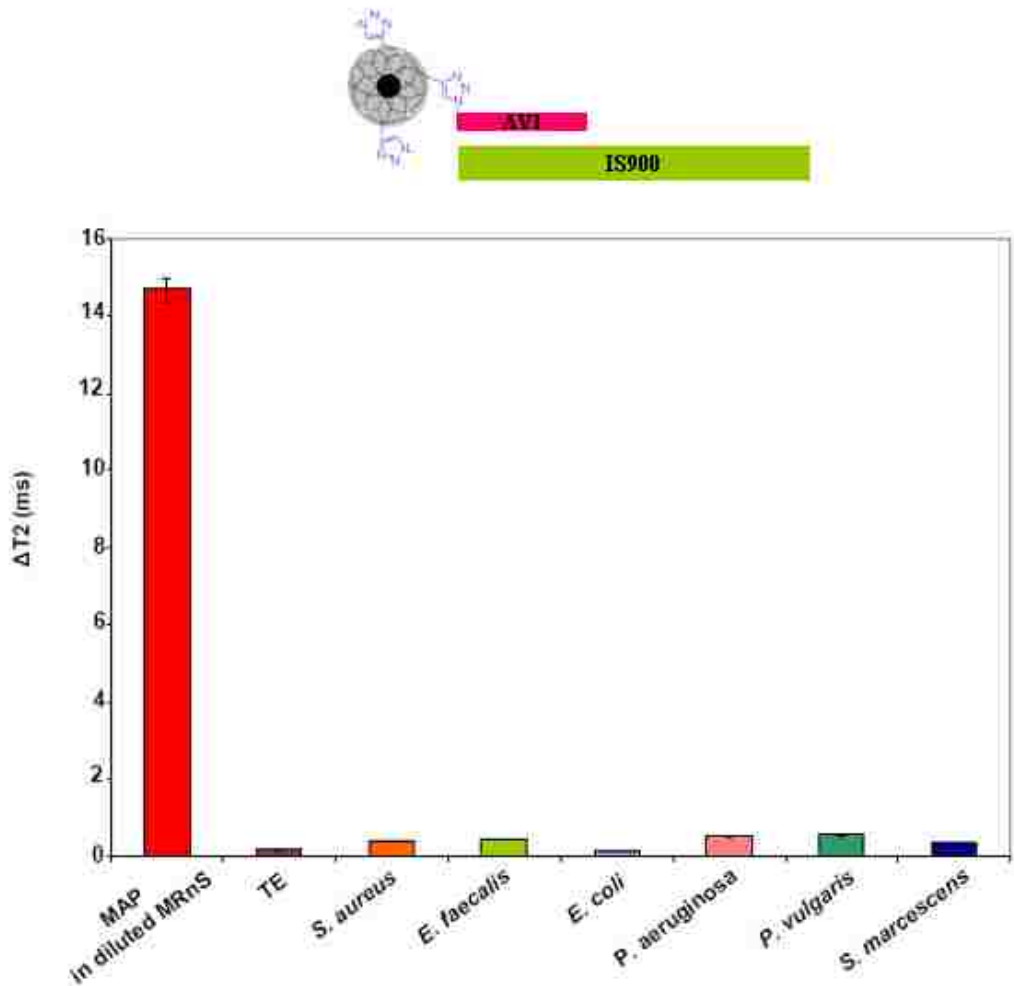
Figure 14: Specificity of IS900 MRnS towards MAP and not other Gram positive and Gram negative bacteria.
TE: TE buffer (Tris:EDTA), and pure DNA extracted from *S. aureus* (*Staphylococcus aureus*), *E. faecalis* (*Enterococcus faeacalis*), *E. coli* (*Escherichia coli*), *P. aeruginosa* (*Pseudomonas aeruginosa*), *P. vulgaris* (*Proteus vulgaris*) and *S. marcescens* (*Serratia marcescens*).

In subsequent studies, we determined if the IS900 MRnS could quantify MAP DNA. MAP DNA was isolated using either a 2-day-long extraction protocol or a 30-minute boiling-based methodology, yielding pure and crude DNA respectively. Following incubation and cooling within 30 minutes, both DNA preparations exhibited concentration-dependent changes in the T2 (Figures 15A-B). Although higher changes were observed in samples with pure MAP DNA, both DNA extraction methodologies had equivalent detection thresholds, approaching the low femtogram (10^{-15}) regime. We then examined whether nested PCR (nPCR) can achieve comparable sensitivity, amplifying crude MAP DNA. After two 3-hour-long cycles and electrophoresis, nPCR was not able to detect IS900 in samples containing crude MAP DNA (Figure 16). This demonstrates the sensitivity and robustness of IS900 MRnS to rapidly detect their target even under conditions of interference, which prevent the use of traditional enzyme-based methods.
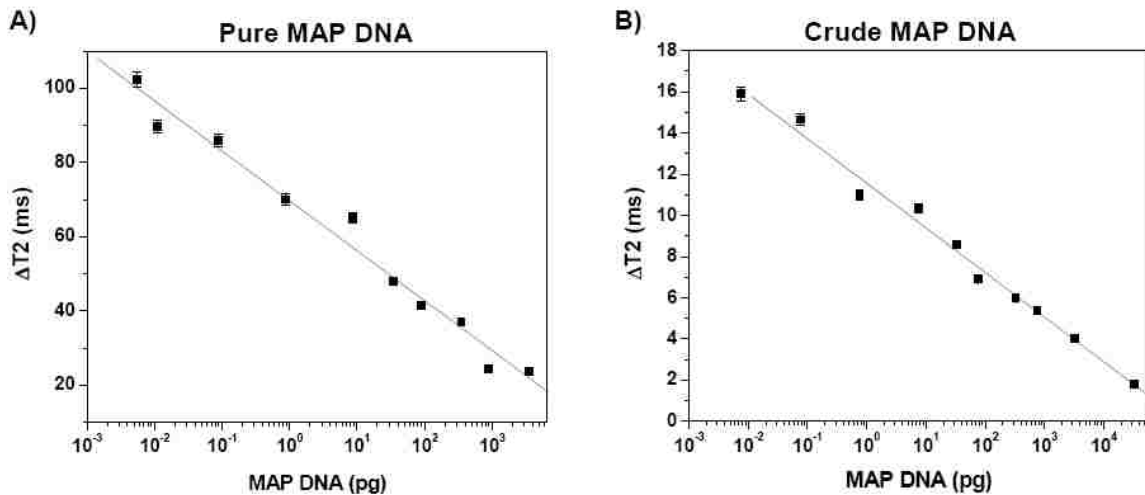
Figure 15: Quantification of MAP DNA using the IS900 MRnS.
A) Pure MAP DNA and **B)** crude DNA extracted via a 30-minute boiling were quantified within 30 minutes after two 3-minute-long incubations at 95 °C.
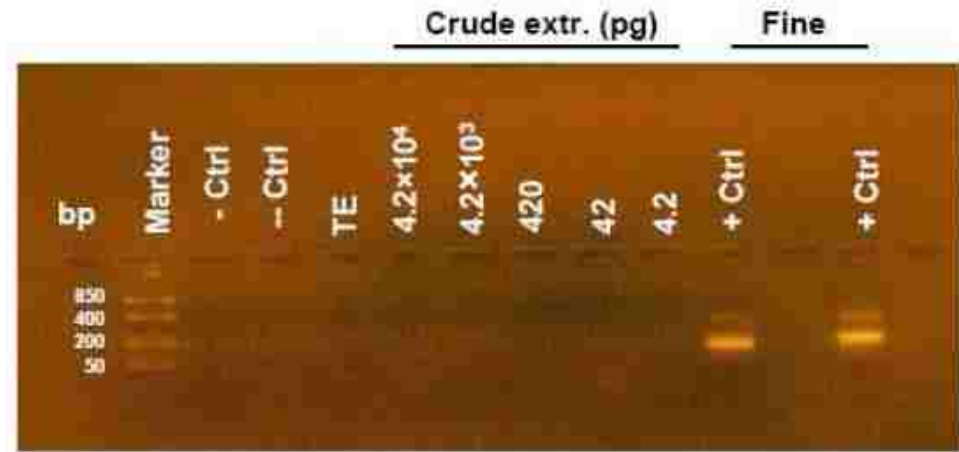
Figure 16: Inability of nested-PCR (nPCR) to quantify crude MAP DNA.
– Ctrl: negative control (dH$_2$O) of the first nPCR round, -- Ctrl: negative control (dH$_2$O) of the second nPCR round, TE: TE buffer, + Ctrl: two controls of pure extracted MAP DNA.

In an effort to determine the sensitivity of the IS900 MRnS, we compared MRnS and nPCR using pure DNA extracts. Also considering the size of MAP's genome (4,829,781 bp) and the average molecular weight of a basepair (MW: 650), we calculated the mass of a single MAP genome copy to be equal to 5.2 fg, and accordingly prepared serial dilutions of MAP DNA with known genome copy numbers. Using these calculations, the MAP IS900 MRnS were able to quantify and detect a single copy of MAP DNA within half an hour (Figure 17A), whereas nPCR was able to detect 5 bacteria only after the second amplification round (Figure 17B). This translates to a total readout time for nPCR to more than 6 hours, with the need of more reagents such as primers and enzymes, as well as labor and equipment time. Intriguingly though, extrapolating the results of the IS900 MRnS with pure MAP DNA (Figure 17A), one could infer that these MRnS have similar detection threshold when crude MAP DNA is used (Figures 15A-B). Overall, these data demonstrate that IS900 MRnS can achieve single MAP genome

detection even in crude DNA samples, outperforming nPCR in readout time, sensitivity and robustness.
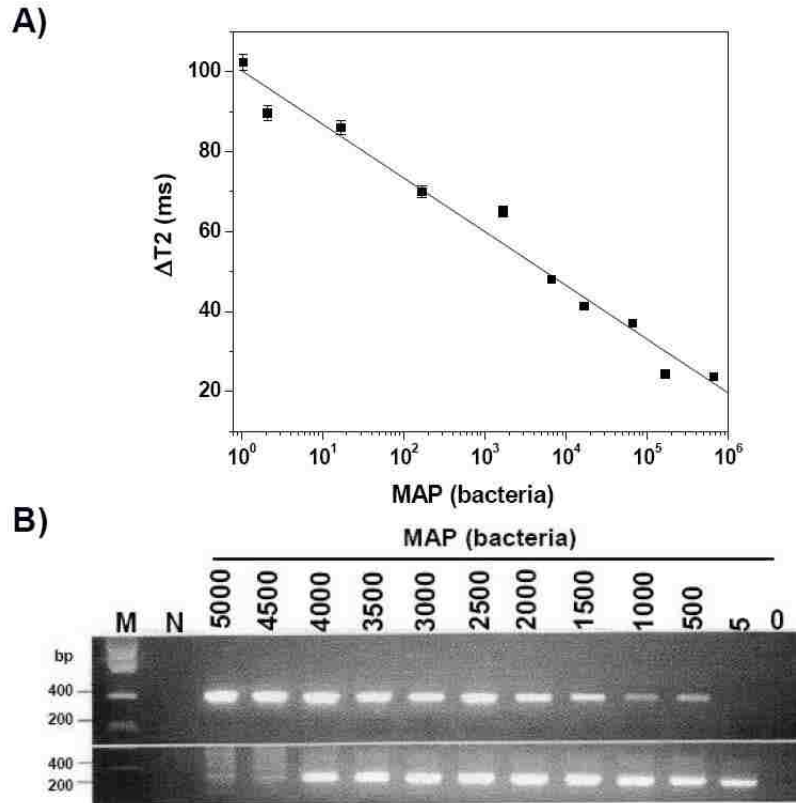
Figure 17: Comparison of the sensitivity of the IS900 MRnS and nPCR.
A) Single MAP bacterium can be detected with the IS900 MRnS within 30 minutes, whereas **B)** comparable sensitivity is achieved after the second nPCR round using pure MAP DNA. (Upper gel image: first nPCR round, lower gel image: second nPCR round, N: negative control (dH_2O) and 0: sterile TE buffer).

Finally, encouraged by the previous studies, we screened clinical isolates from Crohn's disease patients with the IS900 MRnS and compared our results with nPCR. Specifically, the DNA used for the relaxation-based measurements was crudely extracted, whereas for the nPCR pure DNA was used, after establishing that the latter method cannot utilize crude DNA (Figure 16). Following similar procedures to the

50

aforementioned studies, IS900 MRnS were able to rapidly detect MAP in several clinical isolates (Figure 18A), with good correlation to nPCR (Figure 18B). Based on the relaxation changes, quantification of MAP can be achieved, whereas the current nPCR format is not quantitative. Interestingly, one sample deriving from a culture of an ileal biopsy (GN2') was identified as positive by the IS900 MRnS, yet negative by nPCR. This may be justified by either the presence of interferences or poor DNA quality, preventing nPCR detection. Overall though, these results suggest that IS900 MRnS can be used for the screening of not only environmental samples, but also clinical ones, significantly reducing readout time, and eliminating extensive sample preparation steps and the need for expensive labile reagents.
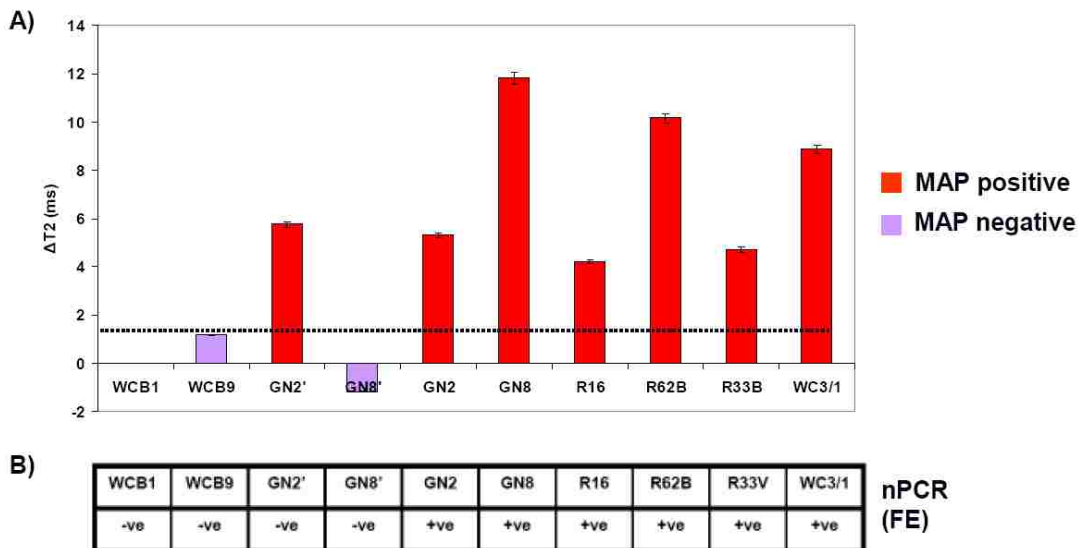
Figure 18: Screening of clinical isolates using IS900 MRnS.
A) Relaxation-mediated detection of MAP in clinical isolates 30-minutes after crude DNA extraction, and **B)** screening and confirmation using nPCR after a two-day DNA extraction and 7 hours of result readout. All isolates were from blood samples from Crohn's disease patients, apart from GN2' and GN8' that correspond to ileal biopsies.

Conclusion

> ➤ Anti-MAP antibody-carrying MRnS and IS900 MRnS can specifically identify MAP, distinguishing it from Gram positive and Gram negative bacteria, as well as other mycobacteria.

> ➤ MRnS can quickly quantify a bacterial target (MAP) in milk and blood with high sensitivity via magnetic relaxation.

> ➤ MRnS can quantify their target under conditions of heavy interference.

> ➤ MRnS can rapidly detect MAP in clinical isolates and homogenized tissue without extensive sample preparation, outperforming current diagnostics methodologies.

Discussion

Rapid and reliable identification of bacteria is critical. Although microbiological approaches utilizing antibodies and nucleic acid markers are very sensitive and specific, their clinical and field application is hindered, as they cannot be performed in crude or minimally processed samples. For instance, isolation and growth require extensive methodology that frequently yields results after a couple of days. Thus, clinical decision making and public healthcare policing are limited, thus delaying proper course of actions, including treatment and produce recall. Furthermore, apart from being time consuming, these methods are costly and have to be performed by trained and experienced personnel, mainly in a laboratory setting.

With the recent advancements in nanotechnology and compact diagnostic equipment, nanosensors can be devised for the identification of biological targets. Apart from being sensitive, the use of minute sample volumes with minimum processing, the

low reagent cost and the faster readout, nanosensors can achieve sensitive detection in remote areas and at the points-of-care. Among the most promising nanosensors are MRnS, which were used for the detection of subcellular entities and viruses in complex media. Little attention has the development of bacterium-specific MRnS received. This was mainly due to the fact that bacteria are significantly larger than the iron oxide nanoparticles, potentially causing the nanosensors to be insensitive to a bacterial recognition event.

Considering this literature gap and the need for sensitive diagnostic modalities in diverse media, we demonstrated that MRnS can be used for the detection of bacteria in complex media, such as milk and blood, through magnetic relaxation. Additionally, the MRnS were able to identify their bacterium target in clinical isolates, achieving comparable reliability to nested PCR yet obtaining results within a fraction of the time needed for this method. Notably, homogenized tissues from infected cattle were identified as MAP positive, hinting the use of the MRnS for food safety monitoring, and environmental and clinical sample screening..

Furthermore, we achieved fast detection of MAP at the genomic level within half an hour, using IS900 MRnS. As detection of a pathogen is critical to be achieved in multiple levels allowing determination of specific biomarkers and virulence factors, we utilized IS900 MRnS for the quantification of MAP DNA in crude and pure DNA extracts. The IS900 MRnS were equally sensitive to both DNA preparations, while not being susceptible to interferences. Single MAP genome copy was detected, surpassing nPCR in sensitivity and readout time. Moreover, clinical isolates were screened and the IS900 MRnS had good correlation with nPCR. Based on these findings, the potential use

of these MRnS in conjunction with other methodologies should be foreseen, allowing quick assessment of microbial identification and directing treatment routes.

Overall, as the MRnS approach apart from sensitive and fast, it is independent of the sample's optical properties, requires minimum sample preparation and can be performed without extensive end-user training, it will be ideal for point-of-care usage. Furthermore, these MRnS can be easily adapted for the high-throughput and expedite screening of samples from animals, humans, and food. Considering the latest advancements in NMR technology with compact and sensitive instrumentation[86], the high-throughput and/or portable analysis of multiple samples in complex media should be doable, even outside of the typical laboratory setting. This method provides a novel approach for microbial detection that can potentially expedite decision making in a broad range of fields including the clinical, environmental and agricultural sectors.

CHAPTER IV: THE ROLE OF NANOPARTICLE VALENCY IN THE DETECTION OF BIOLOGICAL ENTITIES VIA MRnS

Introduction

The enhanced binding of multiple ligands to a particular cellular target is a common approach in nature to fine-tune molecular and cellular recognitions with increased specificity[87-96]. This kind of multivalent binding strategy can offer unique advantages for developing selective and highly sensitive nanoparticle-based diagnostics and effective therapeutics. Nanoparticles with multiple targeting ligands offer the advantage of a surface-mediated multivalent affinity, resulting from multiple interactions between the high local concentration of binding ligands on the nanoparticle's surface and epitopes on the corresponding target. In particular, the conjugation of multiple targeting ligands to iron oxide nanoparticles (IONP) has allowed the creation of multivalent magnetic relaxation nanosensors (MRnS) for the detection of molecular targets and events, such as DNA, RNA, proteins, enzymatic activity, small molecule, viruses, and enzymatic activity[50-54]. Detection is achieved by changes in the solution's water relaxation times ($\Delta T2$), as these nanosensors self-assemble upon interaction with the specific target. However, all these cases shared a common target characteristic; the target was smaller than or had roughly the same size (in the case of a virus) with the nanosensor. Recently, the detection of a bacterium, a much larger target compared to the nanosensor, was reported (Chapter III)[97]. It was found that the use of a multivalent entity (bacterium) as a biological target compensated for the size difference between the nanoprobe and the target, promoting nanoparticle assembly on the bacterial surface with

55

concomitant target-concentration-dependent changes in $\Delta T2$. It was speculated that these differences may have been attributed to the ratio of nanoparticles interacting per target, hinting that at low bacterial concentrations more nanoparticles self-assembled on the surface of the bacterium (hence higher $\Delta T2$), whereas at high bacterial concentrations fewer nanoparticles interacted per target to result in lower $\Delta T2$.

We hypothesized whether the nanoparticles' valency may affect the MRnS detection limit, allowing the engineering of ultrasensitive probes to accommodate a particular cellular concentration range. We reasoned that nanoparticles with low amounts of ligand conjugated on their surface (low valency) would assemble on the cell's surface, resulting in prominent shifts in the $\Delta T2$ (Figure 19A). As the cell concentration increases, the low valency nanoparticles would switch to a quasi-dispersed state, due to their limited interaction with target moieties on discrete cells, thus causing smaller changes in the $\Delta T2$ (Figure 19A). This mechanism would be in line with the reported spherical MRnS-mediated detection of bacteria (*Mycobacterium avium* spp *paratuberculosis* – MAP) using IONP conjugated with anti-MAP polyclonal antibodies, where prominent $\Delta T2$ was observed at low MAP amounts and low $\Delta T2$ was recorded at high MAP concentrations[97]. In contrast, we reasoned that high valency nanoparticles should not cluster in the presence of cells at low concentrations. Instead, the multiple ligands present on the high valency nanoparticle can interact with several receptors on the cell surface (Figure 19B). Therefore, the interaction between high valency nanoparticles and cells at low concentration would result in a less pronounced $\Delta T2$, because fewer nanoparticles may simultaneously interact with multiple receptors on a given cell. Alternatively, as the cell concentration increases, the probability of high valency nanoparticle binding to surface

56

receptors in multiple cells increases. This should facilitate the binding of numerous ligands on the same nanoparticle with many receptors on different cells, causing extensive clustering of the nanoparticles and an increase in $\Delta T2$ as the number of cells increases. (Figure 19B).
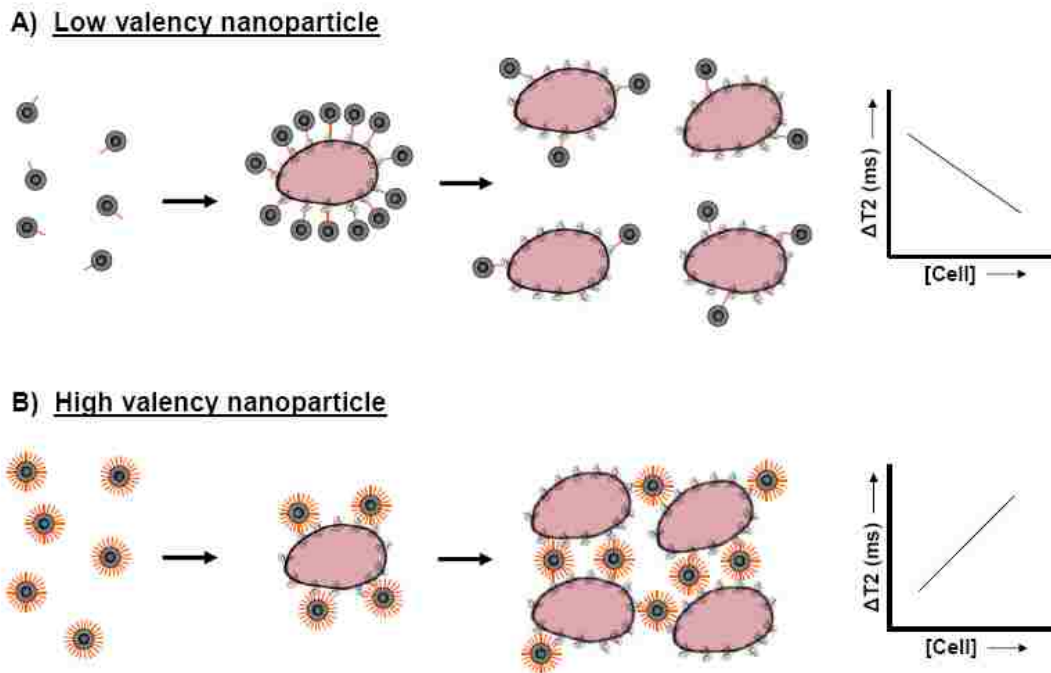
Figure 19: MRnS's valency facilitates distinct magnetic relaxation sensing trends.
A) At low target concentrations, nanoparticles with low valency readily assemble on the target and cause large shifts in the $\Delta T2$, whereas **B)** fewer nanoparticles with high valency interact per target resulting in lower $\Delta T2$. At high target concentrations, the nanoparticles with **A)** low valency switch to a dispersed-like state with a concomitant $\Delta T2$ reduction, but **B)** the ones with high valency bind and cluster between multiple targets, facilitating prominent $\Delta T2$ changes.

Hence, the lack of a comprehensive study addressing how multivalency affects the nanoparticles' cell surface assembly (e.g. bacterium or cell) and the corresponding MRnS response prompted us to utilize MRnS with engineered valency towards the detection of cancer cells in blood samples. We selected cancer cells as a model target, because it has been recently reported that viable tumor-derived epithelial cells found in circulation (circulating tumor cells) are a novel class of cancer biomarkers, participating in the initiation of the process of metastasis[98-100]. Current molecular diagnostic techniques cannot detect low concentrations of cells in biological media (i.e. blood)[100], because of the matrix's optical properties and complexity. Furthermore, commonly used cytological and immunocytochemical techniques require the cell's isolation, purification, fixation and quantification using fluorescent probes and microscopic examination, which prevent propagation of the cells for further analyses[101, 102]. All of the above highlight the importance of developing nondestructive methods for the sensitive detection of circulating tumor cells in blood samples. For our studies, we decided to use a small molecule as opposed to an antibody, because its small size could guarantee higher nanoparticle multivalency and its stability would lead to the development of robust field-deployable nanosensors that are not susceptible to thermal denaturation. As a model small molecule ligand, we chose folic acid (folate), which is the canonical affinity ligand of the folate receptor (FR) that is overexpressed in some tumor cells[103]. Although circulating tumor cells more prevalently overexpress other cell surface markers, such as EpCAM[99], recent studies indicate that the folate receptor (FR) is overexpressed in numerous cancers, including ovarian, testicular, breast and lung[103]. Furthermore, as the expression of FR is upregulated during metastasis, this receptor is a good marker for

58

diagnosis, targeted imaging and drug delivery. As our cellular target, we used A549 lung cancer cells, because lung cancer is among the most common sites of origin of metastatic cancer through migration of lung cancer cells via the circulation[104], and this cell line is known to overexpress the folate receptor[103]. Therefore, we investigated if the folate nanoparticle preparations, and particularly the high-folate ones, can be used for the quantification and sensitive detection of single FR-expressing A549 cells in complex media, via magnetic relaxation.

Materials and Methods

Reagents.

All reagents were of AR (Analytical Reagent) grade. Iron salts ($FeCl_2.4H_2O$ and $FeCl_3.6H_2O$) were obtained from Fluka. Polyacrylic acid (MW 1.8 kDa), ammonium hydroxide, hydrochloric acid, folic acid, N, N'-dimethylformamide (DMF), *N*-hydroxysuccinimide (NHS), cholera toxin B subunit (Ctb) and 3-(4,5-Dimethylthiazol-2-yl)-2,5-diphenyltetrazolium bromide (MTT) were purchased from Sigma-Aldrich. The dialkylcarbocyanine fluorophore DiI (D282) and the nuclear stain DAPI (4', 6-diamidino-2-phenylindole – D1306) were purchased from Invitrogen. EDC (1-Ethyl-3-[3-dimethylaminopropyl] carbodiimide hydrochloride) and Protein G were obtained from Pierce Biotechnology, whereas the polyclonal rabbit anti-human folate receptor antibody (FL-257) was purchased from Santa Cruz Biotechnology. The polyclonal anti-MAP antibody was a gift from Dr. Saleh Naser (Burnett School of Biomedical Sciences, College of Medicine, UCF).

Synthesis of propargylated polyacrylic-acid-coated iron oxide nanoparticles.

The polyacrylic-acid-coated iron oxide nanoparticles were synthesized using the alkaline precipitation method, as recently reported[44]. Briefly, the nanoparticles were prepared by rapidly mixing a Fe^{+3}/Fe^{+2} solution with an ammonium hydroxide solution for 30 seconds, before adding the polyacrylic acid (PAA) solution. The nanoparticles were washed, concentrated and finally reconstituted in phosphate buffered saline (pH = 7.4), using a KrosFlo Research II TFF system equipped with a 10 kDa column (Spectrum Labs). Propargylation of the as synthesized nanoparticles was achieved with carbodiimide chemistry, as previously reported[44]. The propargylated nanoparticles were magnetically separated and characterized, following published protocols[44].

Synthesis of folate-carrying MRnS with different nanoparticle valency using "click" chemistry.

To synthesize folate-conjugated nanoparticles, propargylated nanoparticles (13 mg, 1.69 mg/mL) were added to azide-functionalized folic acid (folate~N_3), according to the literature[44]. Different levels of nanoparticle valency were achieved by varying the stoichiometric ratio of nanoparticle ligand to nanoparticle concentration. For the preparation of low-folate nanoparticles, 0.4 µg of folic acid (0.8×10^{-2} µmol) were used, whereas for the high-folate nanoparticles 4 mg (8×10^{-2} mmol) of folic acid in DMSO. The reaction was initiated at room temperature in the presence of catalytic amount of CuI (0.01 µg, 0.6×10^{-10} mmol), in 125 µL of bicarbonate buffer (pH 8.5), and further incubated for 12 h at room temperature ("click" chemistry). The final reaction mixture was purified with a magnetic column, and finally dialyzed using a 6,000 – 8,000 MW cutoff dialysis bag, against deionized water and phosphate buffered saline (PBS). The

folate nanoparticle preparations were stored at 4 °C until further use. Confirmation of the successful conjugation of folate to the nanoparticles was achieved through UV-Vis and fluorescence emission spectroscopy. In order to make our nanoparticles multimodal, we loaded them with a lipophilic fluorophore. Dye-doped folate-conjugated iron oxide nanoparticles were prepared by the drop-wise addition of DiI (0.1 µg/µL in DMF) in 4.5 mL of the nanoparticle suspension ([Fe] = 1.69 mg/mL), as described in literature[44]. The nanoparticles were magnetically separated, and the complete removal of free (non-encapsulated) dye was confirmed through fluorescence emission spectroscopy, demonstrating a single red-shifted emission maximum. Finally, the nanoparticles were stored in dark at 4 °C until further use.

Synthesis of antibody-carrying MRnS with different nanoparticle valency.

For the conjugation of Protein G to the nanoparticles, polyacrylic-acid-coated nanoparticles ([Fe] = 0.25 mg/mL) were taken in 2 mL MES buffer (pH = 6), and to this we added EDC (1 mg, 0.11 mmol) and NHS (0.8 mg, 0.15 mmol). This reaction mixture was incubated for 3 minutes, followed by drop-wise addition of Protein G (1.5 mg, 60 µmol) in DI water (0.5 mL). Next, the solution was incubated for 30 min at room temperature under continuous mixing, followed by overnight incubation at 4 °C. In order to remove any Protein G molecules that did not conjugate to the nanoparticles, we performed magnetic separation using a 1X-PBS-equilibrated LS25 column. Protein quantification revealed that the nanoparticle preparation's Protein G concentration was 0.1 µg/µL. Subsequently, we conjugated either anti-FR or anti-MAP antibodies to the Protein G-carrying nanoparticles, as previously reported[52]. However, in order to engineer the nanoparticle valency, the Protein G nanoparticles (250 µL) were incubated with

different antibody amounts (5 µg anti-FR, 0.5 ng anti-FR, 5 µg anti-MAP or 0.5 ng anti-MAP), yielding either anti-FR or anti-MAP MRnS with different degrees of valency, which was assessed in accordance to the literature[105, 106].

Synthesis of dextran-coated and galactose-carrying MRnS preparations.

Dextran-coated MRnS were prepared as previously reported[107]. Aminated PAA-coated IONP were synthesized in accordance to the literature[44], and conjugation of galactopyranosyl nonanoic acid (Toronto Research Chemicals) was achieved via carbodiimide chemistry. Specifically, 1,000 µL of aminated PAA-coated IONP ([Fe] = 2.5 µg/µL) were reacted with the carboxylated galactose (33 mg in 1,000 µL DI water – DMSO 50:50 v:v) in the presence of EDC and NHS (9.5 and 5.5 mg respectively in 1,000 µL MES buffer). The reaction was carried out overnight at 4 ^{o}C under constant mixing, followed by dialysis (6,000 – 8,000 MWCO) and magnetic separation.

Nanoparticle characterization.

The size of the folate-conjugated MRnS was determined through dynamic light scattering (DLS), using a PDDLS CoolBatch 40T instrument and the Precision Deconvolve 32 software. Iron concentration was determined spectrophotometrically after acid digestion of the nanoparticles' suspension as previously reported[44, 107], whereas R1 and R2 relaxivity measurements were obtained using a 0.47T mq20 NMR analyzer (Minispec, Bruker). Zeta potential measurements were performed on a Nano-Z zetasizer (Malvern), operating at 25 ^{o}C. To determine the presence of propargyl groups on the surface of the propargylated nanoparticles, FT-IR was performed on a PerkinElmer Spectrum 100 FT-IR spectrometer, and to confirm the successful conjugation of folate to the folate

nanoparticles' surface UV-Vis absorbance and fluorescence emission profiles were obtained, using a Cary300 spectrophotometer (Varian) and a NanoLog-3 fluorimeter (Horiba Jobin-Yvon). Similarly, the folate nanoparticles' fluorescence emission associated with the encapsulated DiI was determined with the NanoLog-3 fluorimeter. Protein G and antibody quantification was achieved colorimetrically through the BCA assay (Pierce) in accordance to the supplier's protocol, and determination of the amount of folate and antibody per nanoparticle was determined as described in literature [52, 105, 106].

Mammalian cell cultures.

Cancer human alveolar cells (A549) and normal (non-cancer) rat cardiomyocytes (H9c2) were obtained from ATCC, and maintained in accordance to the supplier's protocols. Briefly, the A549 cells were maintained in a 5%-FBS-containing DMEM medium supplemented with antimycotic/antibiotic, whereas the H9c2 cells were propagated in a 10%-FBS-containing MEM medium containing antimycotic/antibiotic. All cell cultures were grown in a humidified incubator at 37 $^{\circ}$C under a 5% CO_2 atmosphere.

Hemocytometer-mediated cell quantification.

After detaching the cells from the culture plate using trypsin and suspending them in growing medium, the cellular suspension was centrifuged at 1,000 rpm for 8 minutes and the pellet was re-suspended in 2 mL of the corresponding medium. Ten µL aliquots of the resulting cell suspensions were thoroughly mixed with 10 µL trypan blue solutions. Quantification was performed using a hemocytometer and a phase-contrast microscope.

63

Serial dilutions of stock mammalian cellular suspensions.

After determining the cell concentration of the stock suspensions, serial dilutions were prepared in 1X PBS, 5% PBS-diluted blood or whole blood, using aseptic techniques. Fresh blood was a gift from Dr. James Hickman (UCF NSTC), obtained from bacteremia-free Crl:CD(SD)IGSBR female rats (Charles River Laboratories). All serial diluted samples were used immediately after preparation.

Fluorimetry-based determination of MRnS – mammalian cell association.

One mL cellular suspensions (10^3 and 10^6 A549 cells) in PBS, were incubated with 1 μL folate-carrying nanoparticles ([Fe] = 1.69 µg/mL) for 60 minutes at room temperature, under continuous mixing (300 rpm). To remove any unbound nanoparticles, the samples were centrifuged three times at 1,000 rpm for 8 minutes, each centrifugation round followed by washing with 1X PBS. The resulting cell pellets were resuspended in 1 mL 1X PBS, and fluorescence emission spectra were recorded using a NanoLog-3 fluorimeter (Horiba Jobin-Yvon).

Confocal laser-scanning microscopy.

A549 cells were grown overnight on culture dishes, before treatment. After incubation with the nanoparticles, the cells were washed three times with 1X PBS, fixed with 5% formalin solution, and stained with DAPI (Molecular Probes). Subsequently, the cells were examined with a Zeiss LSM 510 confocal microscope equipped with a 40X objective.

Dynamic light scattering (DLS) of MRnS – mammalian cells.

One mL cellular suspensions in PBS, either with 10^3 or 10^6 A549 cells, were incubated with 1 µL folate-PAA-IONP ([Fe] = 1.69 µg/mL) for 60 minutes at room temperature, under continuous mixing (300 rpm). The alterations in the nanoparticle size distribution were monitored through the PDDLS CoolBatch 40T instrument and the Precision Deconvolve 32 software.

Magnetic-relaxation-mediated mammalian cell detection.

Ten µL aliquots of cell suspensions were incubated with 190 µL of nanoparticle working solutions ([Fe] = 0.01 µg/µL) at room temperature. Spin-spin relaxation times (T2) were recorded over time via the 0.47T mq20 NMR analyzer (Minispec, Bruker, Germany), operating at 40 ^{o}C.

Magnetic isolation of A549 cells and detection of the expression of the folate receptor.

After screening samples via magnetic relaxation, they were incubated with various concentrations of folate-PAA-IONP for 30 minutes at 37 ^{o}C. Subsequently, each sample was passed through a 1X-PBS-equilibrated LS25 MACS$^{®}$ column (Miltenyi Biotec). After removing the column from the magnet, the eluate was captured in culture dishes with 5%-FBS-containing DMEM medium. The dishes were placed in a humidified incubator (37 ^{o}C, 5% CO_2) for 24 h, as according to the supplier the doubling time of A549 cells is 18 h. Then, the cells were washed three times with 1X PBS and fresh medium was added. Cells were quantified using the hemocytometer method and 500-cell aliquots of either A549 or H9c2 cells were seeded into a 96-well microtiter plate. After

65

overnight growth, the cells were incubated for 1 h with different nanoparticle concentrations at 4 °C. Then, the cells were washed three times with 1X PBS in order to remove any unbound nanoparticles, and 100 µL of 0.2 mM TMB in citrate buffer pH 4.0 (3, 3', 5, 5'-tetramethylbenzidine, Sigma) as well as 10 µL H_2O_2 (Acros) were added. Twenty minutes after, absorbance was recorded at 652 nm, using a µQuant 200 microtiter plate reader (Biotek).

Flow cytometry.

A549 and H9c2 cells were grown until reaching confluence. After detachment and centrifugation at 1000 rpm, the cell pellets were collected and resuspended in 1X PBS. The resulting cell suspensions were incubated with the anti-folate-receptor antibody (0.5 µg/mL) for 30 min at 4 °C, under continuous mixing. After the incubation with the primary antibody, the cells were centrifuged and resuspended in PBS three times, followed by a 30-min incubation at 4 °C with an FITC-conjugated goat anti-rabbit-IgG antibody (0.5 µg/mL). The FITC-conjugated antibody was a gift from Dr. James Hickman (Nanoscience Technology Center, UCF). Finally, the cells were centrifuged and resuspended in PBS three times, and the cellular suspensions were examined using a FACSCalibur flow cytometer (BD Biosciences).

Cell viability studies.

Equal populations of A549 cells either magnetically isolated using the folate-carrying iron oxide nanoparticles or readily harvested, which had been quantified with a hemocytometer, were seeded in 96-well plates. After overnight growth in a 5%-FBS-containing DMEM medium at 37 °C, 5% CO_2 in a humidified incubator, the cells were

washed three times with 1X PBS and treated with 20 µl MTT (5 µg/µl, Sigma-Aldrich) for 2 hours. Using acidified isopropanol (0.1 N HCl), the formazan crystals were dissolved and the absorbance was recoded at 570 nm and 750 nm (background) via a Synergy µQuant microtiter plate reader (Biotek).

Bacterial stocks.

Serial dilutions of heat inactivated *Mycobacterium avium* spp. *paratuberculosis* (MAP) in 1X PBS and anti-MAP antibody were a gift from Dr. Saleh Naser (Burnett School of Biomedical Sciences, College of Medicine, UCF).

Magnetic-relaxation-mediated bacterial cell detection.

Similar to the mammalian cell (A549) protocol, ten µL aliquots of cell suspensions were incubated with 190 µL of nanoparticle working solutions ([Fe] = 0.01 µg/µL) at room temperature. Spin-spin relaxation times (T2) were recorded over time via the 0.47T mq20 NMR analyzer (Minispec, Bruker).

Dynamic light scattering (DLS) of MRnS – bacteria.

Similar to the corresponding mammalian studies, one mL MAP bacterial suspensions in PBS, either with 500 or 5 CFUs (Colony Forming Units), were incubated with 1 µL anti-MAP-PAA-IONP ([Fe] = 0.50 µg/mL) for 60 minutes at room temperature, under continuous mixing (300 rpm). The alterations in the nanoparticle size distribution were monitored through the PDDLS CoolBatch 40T instrument and the Precision Deconvolve 32 software.

Surface Plasmon Resonance (SPR) studies for the toxin-sensing MRnS.

GM1-coated slides were prepared by applying 50 µL of the ganglioside (3 ng/µL, Sigma) directly to the apical surface of the gold plate. The plate was allowed to air dry for 30 minutes at room temperature. Afterwards, the Ctb pentamer was appended to the GM1-coated SPR sensor slide by diluting 2 µL Ctb (1 µg/µL, Sigma) to 50 µL 1X PBST (Phosphate buffered Saline Tween-20, Fisher), and the slide was stored at 4 ^{o}C until further use. The SPR experiments were performed on a Reichert SR7000 SPR refractometer (Depew, NY). Before adding the experimental samples, PBST (pH 7.4) was perfused over the sensor slide for 5 minutes, in order to establish a baseline reading. The samples, diluted accordingly to 1X PBST, were then flowed over the sensor slide, where the potential ligand binding to the toxin-coated sensor slide led to an increase in the mass on the slide. Subsequently, this shift in mass generated a change in the resonance angle of the reflected light, which was recorded as a change in the refractive index. After each reading, the bound ligand was removed from the sensor slide by PBST washing for 5 minutes. The SPR studies were based on a blind setup, hence performed by an investigator unrelated to the MRnS study (Dr. Tuhina Banerjee).

Magnetic-relaxation-mediated detection of the Cholera toxin B subunit (Ctb).

Serial dilutions of Ctb were prepared in DI water. Five µL aliquots of Ctb were incubated with 195 µL of either galactose-carrying or dextran-coated MRnS working solutions ([Fe] = 0.001 µg/µL) at room temperature. Spin-spin relaxation times (T2) were recorded over time via the 0.47T mq20 NMR analyzer (Minispec, Bruker).

Data analysis.

All experiments were performed at least three times, and during each experiment three measurements were taken for each experimental condition. Each graph dataset contains the obtained averages of the corresponding study. Total fluorescence intensity per mL (Total FI_{mL}) is defined as the summation of each 1-mL sample's fluorescence intensities from 570 to 640 nm. For the magnetic relaxation quantification plots, the best model fit was achieved using either linear or sigmoidal fit (OriginPro 7.5, Origin Lab Corp, MA, USA). As we previously reported, $\Delta T2$ is defined as the average $T2_{sample,i}$ minus the average $T2_{control,i}$ at time i, where for the control sample sterile, non-spiked medium (blood or milk) was used. To determine cell viability, we subtracted the background absorbance at 750 nm from the absorbance at 570 nm, as previously reported. The percentage cell viability for the cells isolated was calculated using the formula: $\Delta A_{570-750sample}/\Delta A_{570-750control} \times 100$, where the corresponding control for the cells isolated with low- and high-folate nanoparticles were harvested cells seeded in low and high population counts (Control low and Control high).

Results

To examine our hypothesis, we prepared polyacrylic-acid-coated iron oxide nanoparticles with different ligand valency by varying the stoichiometry of the conjugation reaction. These polymer-coated nanoparticles had an average hydrodynamic diameter of 90 nm, ζ potential of -82.6 ± 2.4 mV, spin-lattice (R1) and spin-spin relaxations (R2) of 53 $mM^{-1}s^{-1}$ and 206 $mM^{-1}s^{-1}$, respectively. "Click" conjugation of targeting moieties to the nanoparticles' surface was achieved by incorporating alkyne

groups via carbodiimide chemistry (Figures 20 and 21), having a ζ potential of -62.6 $\pm$ 2.9 mV.
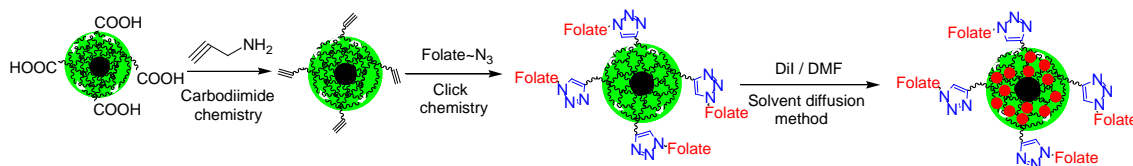
Figure 20: Schematic representation of the surface modification and folate conjugation to polyacrylic-acid-coated IONP.
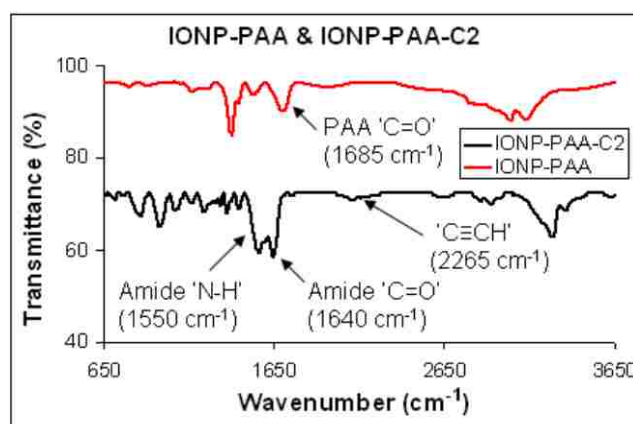
Figure 21: FT-IR spectra of the unmodified and alkyne-modified polyacrylic-acid-coated IONP.
IONP-PAA: unmodified PAA-coated IONP; IONP-PAA-C2: alkyne-modified PAA-IONP

As a model targeting moiety, we used folic acid (MW: 441.4), which is the affinity ligand of the transmembrane folic acid receptor (FR) that is overexpressed in several cancers[103]. Hence, azide-functionalized folic acid was conjugated to the alkyne-carrying polyacrylic-acid-coated nanoparticles via click chemistry, having different concentrations of folate while maintaining constant the nanoparticle concentration. The

70

presence of folate on the nanoparticles was corroborated by the presence of a 352 nm shoulder peak in the UV-Vis absorbance spectrum (Figure 22A) and a corresponding 446 nm peak in the fluorescence emission spectrum (Figure 22B). Using this spectrophotometric information and following published protocols[105, 106], we determined that the high-folate nanoparticles had on average 120 folic acid moieties per nanoparticle (ζ potential = -59.4 ± 3.6 mV), whereas the low-folate nanoparticles had on average 1 folic acid per nanoparticle (ζ potential = -53.5 ± 4.1 mV).
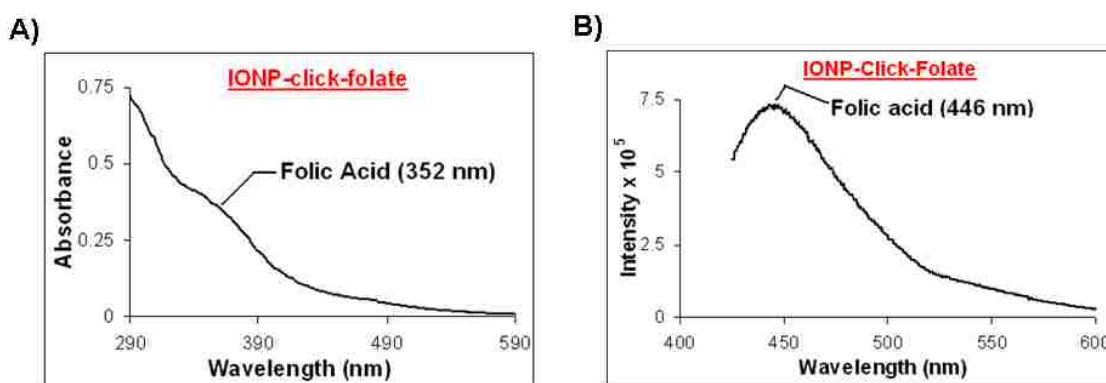
Figure 22: Spectroscopic characterization of the folate-carrying MRnS.
A) UV/Vis and **B)** fluorescence emission spectroscopy.

The folate-carrying nanoparticles were then doped with the fluorophore (DiI), resulting in fluorescently labeled nanoparticles (Figure 23), as recently reported[44]. Contrary to fluorophore conjugation to the nanoparticles' surface, this method facilitates fluorophore encapsulation within the polymeric coating's microdomains and does not compromise the nanoparticles' folic acid valency. Hence, this allows the use of these nanoparticles in confocal microscopy (Figure 24) and fluorimetric studies with folate-receptor-expressing cells (Figure 25).
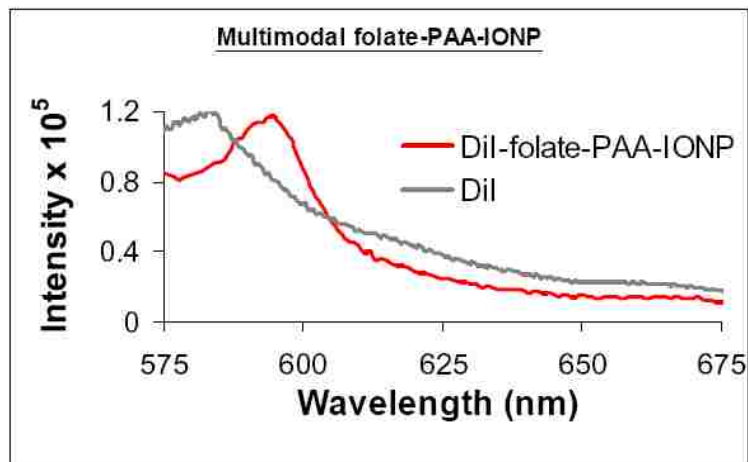
Figure 23: Fluorescence emission spectrum of the multimodal DiI-encapsulating folate MRnS.
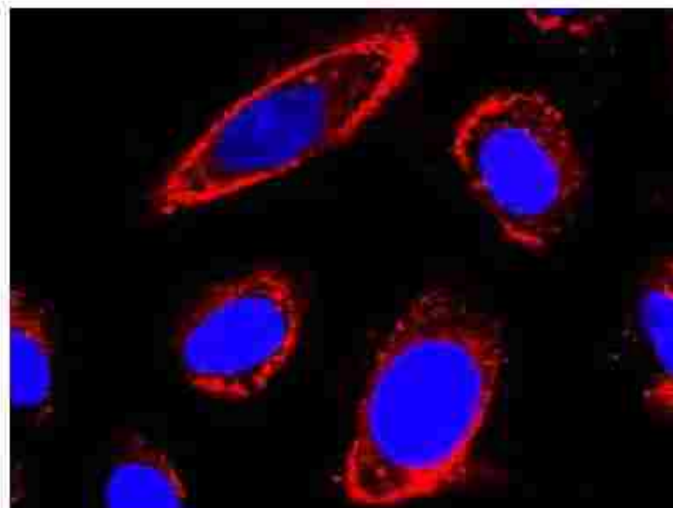
Figure 24: Confocal laser-scanning microscopy indicating the association of DiI-encapsulating folate IONP with FR-expressing cells.
A549 cells; Red: DiI, Blue: DAPI

In addition to the folate nanoparticles that carry a small molecule (folate), we synthesized nanoparticles with different levels of anti-folate-receptor (anti-FR) antibodies (MW: 150,000). Specifically, via carbodiimide chemistry, Protein G was conjugated to the as synthesized polyacrylic-acid-coated nanoparticles, which have readily available carboxylic acid groups. Following magnetic separation and nanoparticle-associated protein quantification (2 Protein G molecules per nanoparticle on average), the antibodies were conjugated to the Protein G nanoparticles through an overnight reaction carried at 4 ^{o}C. To engineer the valency and obtain nanoparticles with either low or high levels of conjugated antibodies, we varied the stoichiometry of the nanoparticle conjugation reaction, by modifying one of the reactant's concentration (either 5 µg anti-FR or 0.5 ng anti-FR) while keeping the Protein G nanoparticles' amount constant (250 µL). These conjugation reactions resulted in the formation of nanoparticles with high (4 anti-FR molecules per nanoparticle on average) and low (1 anti-FR molecule per nanoparticle on average) anti-FR levels, as determined with the BCA assay following literature available protocols.

To initially test our hypothesis, we investigated the MRnS – cell associations via fluorescence spectroscopy. Since our nanoparticles apart from magnetic are fluorescent, we employed this technique due to its enhanced sensitivity and spectral acquisition capability, allowing the determination of the nanoparticle – cell association and quantification of this interaction by recording the fluorescence emission from the isolated cells. Therefore, any fluorescence emission associated with the isolated cells should have been an indication of the degree of interaction between the nanoparticles' ligands and cell surface receptors. A major advantage of fluorescence spectroscopy in contrast to confocal

73

laser scanning microscopy is its ability to determine the cell – nanoparticle interaction in suspension, where confocal microscopy requires adherent cells. Additionally, although flow cytometry is an alternative solution-based technique, it was not employed because (i) large cell populations are required to obtain statistically significant results, (ii) it has limited sensitivity for fluorophores that weakly associate with cells or at low fluorophore concentrations (for instance few nanoparticles), and (iii) the compromised multispectral capability (restricted number of acquired wavelengths).

Thus for the fluorimetry studies, the two nanoparticle preparations having different folate levels (120 versus 1 folate molecule per nanoparticle) were incubated for 1 h at room temperature under constant mixing with folate-receptor-expressing lung carcinoma cells (A549) in suspension[103], followed by cell harvesting via centrifugation. The resulting cell pellets were washed with 1X PBS to remove any unbound nanoparticles and finally reconstituted in 1 mL 1X PBS, allowing the comparison of total fluorescence emission per mL (Total FI_{mL}) among the various samples. Interestingly, fluorimetry studies revealed that the total fluorescence emission from the low cell density sample incubated with low-folate nanoparticles was higher than that of the corresponding high cell density sample (Figures 25A and 25B). This difference may be attributed to the higher number of recognizable epitopes in the cell suspension, as a result of the higher cell density (more cells more folate receptors), mediating MRnS's quasi-dispersion with a concomitant reduction in cell-associated fluorescence.
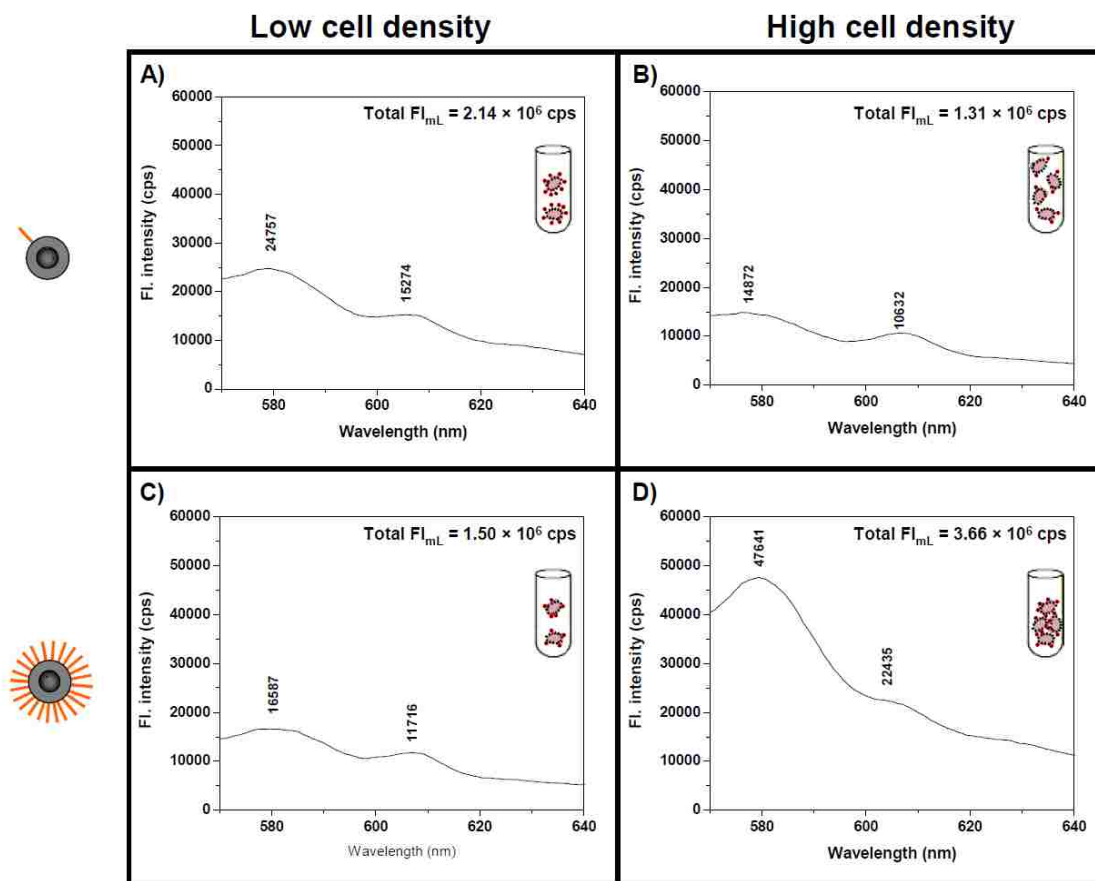
Figure 25: Distinct associations between fluorescent-labeled folate IONP and FR-expressing cells due to the nanoparticles' different valency.
A) Low and **B)** high cell density A549 cells incubated with DiI-encapsulating low-folate nanoparticles. **C)** Low and **D)** high cell density A549 cells incubated with the corresponding high-folate nanoparticles. (The two primary fluorescence emission peaks for DiI are indicated, as well as the total fluorescence emission per mL (Total FI_{mL}) of the acquired spectra. Insets diagrammatically represent the interactions between cells and the nanoparticles in equal-volume samples.)

Likewise, we assessed the high-folate MRnS interaction with A549 cells, by employing the same experimental approach. Contrary to what was observed with the low-folate nanoparticles, fluorimetry studies demonstrated that under conditions of low cell density the total fluorescence emission was lower than that from the high cell density sample (Figures 25C and 25D). It is plausible that at low cell density the nanoparticles'

higher valency may have facilitated the interaction of a given nanoparticle with multiple folate receptors found on the same cell. Consequently, this may have caused fewer high-folate nanoparticles interacting with a given cell, leading to less prominent cell-associated fluorescence. However, under high cell density, the high-folate nanoparticles multivalency could have promoted the nanoparticle's inter-cellular interaction with folate receptor epitopes found on adjacent cells in the nanoparticle's proximity, leading to enhanced fluorescence emission.

To further assess the interaction between MRnS and cells, DLS was used to determine how the nanoparticle valency differentially mediates the dispersion state of the nanoparticles in solution under varying target cancer cell concentrations. In the absence of any cell in solution, the nanoparticles were highly dispersed as 100% of the nanoparticles had a diameter below 100 nm, as previously reported.[44] When the low folate nanoparticles were added to a suspension of cells at low cell density (10^3 A549 cells/mL), 23% of these nanoparticles formed large nanoparticle aggregates while only 77% remained dispersed (Table 4). In contrast, only 14% of the high-folate nanoparticles formed nanoparticle aggregates at the same cell density (10^3 A549 cells/mL), in accordance with our hypothesis (Table 4). As stated before, this may be attributed to the fact that the high-folate nanoparticles' increased valency can facilitate the interaction of a nanoparticle with multiple target receptors on the same cell, similar to what was observed through fluorescence spectroscopy (Figure 25C). Interestingly, when we increased the number of cells in suspension to 10^6 cells/mL, the population of low-folate nanoparticles adopting a clustered state decreased from 23% to 13%, whereas the population of clustered high-folate nanoparticles increased from 14% to 35% (Table 4). These changes

76

are in line with the fluorimetry data, where similar changes were observed. Specifically, for the low-folate nanoparticles, DLS indicated a reduction by a factor of 1.77 versus 1.63 by fluorescence spectroscopy, whereas for the high-folate nanoparticles both methods provided comparable results (DLS increase by a factor of 2.5 vs 2.43 determined by fluorimetry). Taken together, the fluorimetry and dynamic light scattering results corroborate our model, and demonstrate that the nanoparticles' ligand valency modulates the differential interactions between folate MRnS. Hence, these distinct nanoparticle – cell associations in solution may facilitate different magnetic relaxation sensing dynamics and cell capturing capabilities.

Table 4: Size distribution of the folate nanoparticles in the presence of various A549 concentrations.
(Means ± SE)

Nanoparticle	Diameter (nm)	Cell density	
		Low	High
	> 100	23 ± 0.4%	13 ± 0.5%
	< 100	77 ± 0.3%	87 ± 0.2%
	>100	14 ± 0.2%	35 ± 0.3%
	< 100	86 ± 0.3%	65 ± 0.5%

Considering that detection with MRnS is governed by the degree of nanoparticle association[50, 52] with a target and in light of the aforementioned data, we reasoned that there could be dramatic differences in the magnetic-relaxation-mediated cell detection, attributed to the nanoparticles' valency. We anticipated that MRnS with high valency, due to the multiple specific interactions between their carrying ligands and cell epitopes, may achieve better detection sensitivity and even single cancer cell quantification. This is critical, as it was recently demonstrated that even a single metastatic cancer progenitor cell can successfully induce tumor formation[108].

Specifically, we utilized the folate MRnS preparations (1 versus 120 folate moieties per nanoparticle) and the anti-FR ones (1 versus 4 antibody molecules per nanoparticle), in order to assess the detection performance of these nanosensors. To demonstrate the potential ability of our nanosensors to detect circulating cancer cells in clinical samples, we detected A549 cells in blood diluted in phosphate buffered saline (PBS). In these studies, a stock cellular suspension of A549 cells was quantified using a hemocytometer, followed by the preparation of serial dilutions of the stock suspension in PBS-diluted blood. Subsequently, 10 µL aliquots of the resulting cellular suspensions were incubated with 190 µL of the corresponding nanoparticle working solution ([Fe] = 0.01 µg/µL) at room temperature, while monitoring the changes in spin-spin relaxation ($\Delta T2$) with a magnetic relaxometer operating at 0.47 T.

After a brief 1-hour-long incubation at room temperature under continuous mixing, distinct valency-dependent trends were observed (Figure 26A-D). We chose 1-hour-long incubation at room temperature in order to investigate the field applicability of our assay and its ability to provide fast and reliable results, whereas mixing of the

samples minimized the possibility of nanoparticle internalization via folate-receptor-mediated endocytic uptake. An increase in the $\Delta T2$ was observed as the number of A549 lung carcinoma cells increased in solution when both high valency nanoparticles (high folate and high ant-FR antibody) were used (Figures 26A-B), whereas the opposite trend was observed for the nanoparticles with low ligand levels on their surface (decrease in $\Delta T2$ when the cell concentration increased) (Figures 26C-D). These results supported our hypothesis and were in line with the DLS and fluorimetry data. Specifically, as the $\Delta T2$ for high cell counts (>1000) of the low-folate nanoparticles was 1.5 – 1.7 ms and the $\Delta T2$ for a single cell detected by the high-folate nanoparticles was 2.5 ms, this may be attributed to the fact that 13% of the low folate nanoparticles interacted with cells at high cell density versus 14% of the high valency nanoparticles associated with cells at low cell density, as determined through DLS (Table 4).
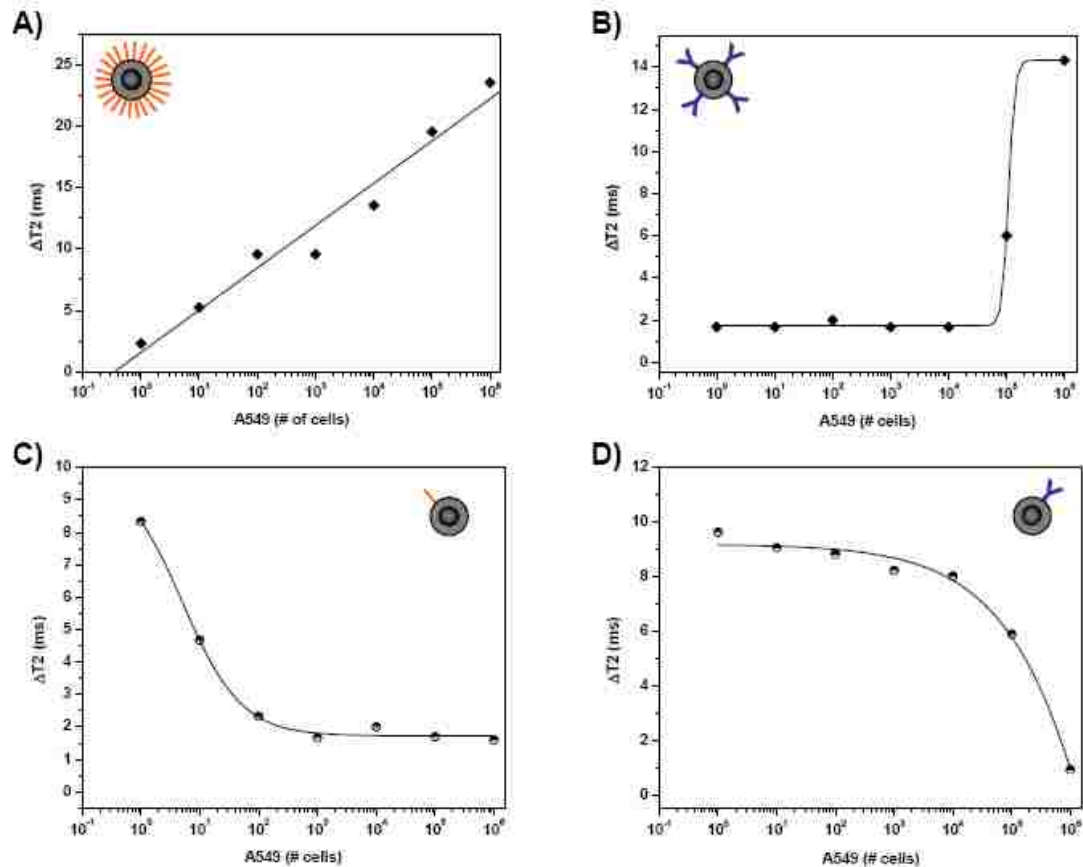
Figure 26: Relaxation-mediated detection of cancer cells in PBS-diluted blood after a 60-min incubation.
A) Using high-folate nanoparticles, **B)** high-anti-FR nanoparticles, **C)** low-folate nanoparticles and **D)** low-anti-FR nanoparticles. (Means ± SE; SE were within 1-2%, which are too small to be depicted)

Furthermore, our data suggest that in our previous report[97] the observed decrease in ΔT2 upon increase of the bacteria concentration was attributed to the nanoparticles' low antibody levels (low nanoparticle valency). This is corroborated by the detection pattern of the low-anti-FR nanoparticles (Figure 26D), exhibiting sigmoidal shape similar to our previous report using MAP bacteria and a corresponding low valency nanoparticle[97]. Although the detection threshold of the low valency anti-FR nanoparticles was 10^4 cells, the low-folate nanoparticles were more sensitive and able to detect a single

cell and quantify the target within the range of 1 to 10^3 cells, (Figure 26C). Most

importantly, the high-folate nanoparticles were able to detect and quantify cells within an

even wider dynamic range $(1 - 10^6)$ (Figure 26A), outperforming the high anti-FR

nanoparticles (Figure 26B) and demonstrating the versatility of small molecule ligands.

Performing the magnetic relaxation studies at shorter incubation times (15 minutes)

compromised data quality for the low-folate and both anti-FR nanoparticle preparations,

leading to poor correlation coefficients (Table 5). However, the high-folate nanoparticles

achieved good correlation coefficients $(R^2 > 0.9)$ even after a 15-minute incubation,

demonstrating the enhanced detection kinetics of the high-folate nanoparticles (Figure

27). Therefore in light of these results, valency plays a critical role in the detection profile

of cancer cells using magnetic relaxation, as multivalency achieved via small molecules

(folate) facilitates fast single cell detection in blood.

Table 5: Correlation coefficients of quantification curves from time-dependent magnetic relaxation studies.

Nanoparticle	Time (mins)			
	15	30	45	60
	0.79	0.84	0.87	0.99
	0.94	0.95	0.96	0.99
	0.76	0.89	0.94	0.99
	0.55	0.86	0.92	0.99
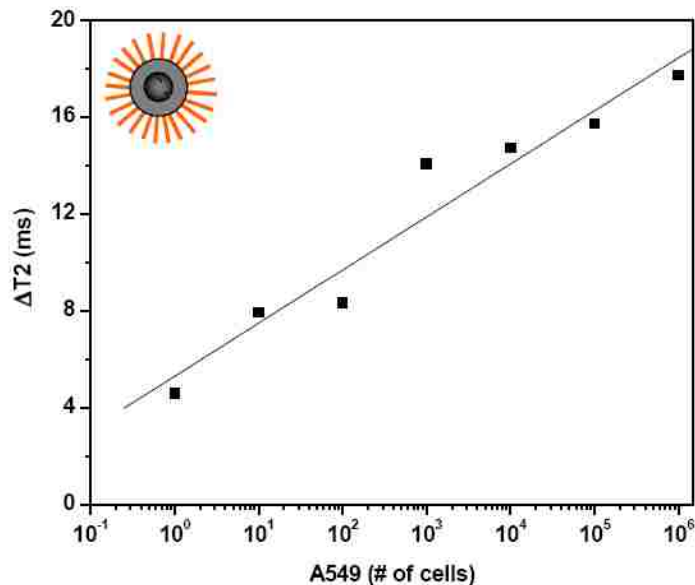
Figure 27: Relaxation-mediated detection of cancer cells in PBS-diluted blood after a 15-min incubation using high-folate nanoparticles.
(Means ± SE; SE were within 1-2%, which are too small to be depicted)

Next, we studied the specificity of our high-folate MRnS towards the folate receptor. Previously, it has been reported that antibody-carrying iron oxide nanoparticles can specifically detect bacteria[97, 107], whereas negative controls of Protein-G IONP yielded no changes in the relaxation times[107]. First, we saturated the nanoparticles' solution with excess folate (10 mg/mL), and data indicated that the folate nanoparticles could not detect the lung carcinoma cells (A549) under these conditions, as seen by the concomitant absence of significant changes between the samples screened (Figure 28A). Likewise, saturation of the culture medium with excess folate (10 mg/mL) prevented the nanoparticles' interaction with the cells' folate receptors (FR), as indicated by the absence of fluorescence emission from the plasma membrane (Figure 29A). Furthermore, we used cells that do not express the folate receptor (H9c2), which when incubated with

the nanosensors failed to induce any cell-concentration-dependent changes in the solution's T2 times (Figure 28B). Thus, these data support the hypothesis that the folate nanoparticles interact specifically with the folate receptor at the plasma membrane of cells expressing this receptor, facilitating magnetic relaxation detection and fluorescence imaging.
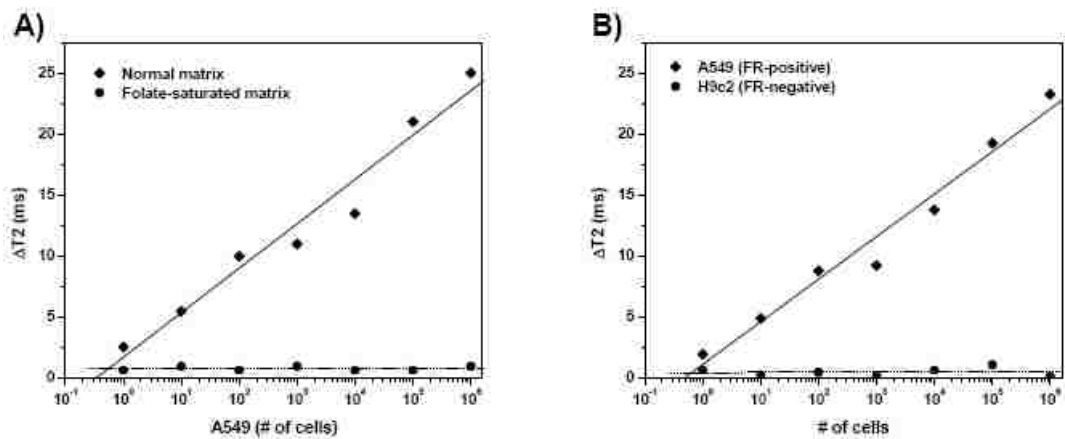
Figure 28: Determination of the folate nanoparticles' specificity.
A) Through either saturation of the matrix with excess folate, or **B)** folate-receptor (FR) negative cells. (Means ± SE; SE were too small to be displayed (1-2%))
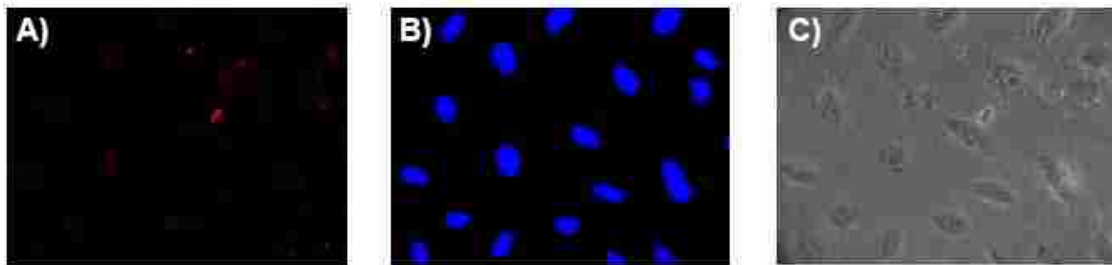
Figure 29: Saturation of the culture media with excess folate prevents the association of the dye-doped folate nanoparticles with A549 cells.
The cells were incubated with the nanosensors for 2 h at 37 ^{o}C, 5% CO_2. (**A**) Red channel – DiI, **B)** Blue channel – DAPI, **C)** Phase contrast).
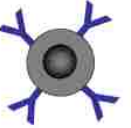
After elucidating the role of nanoparticle valency in the nanoparticle –
mammalian cell interaction in the target cells' magnetic relaxation detection trend and
sensitivities, we investigated if this behavior applied to other systems. Particularly, we
examined the role of the nanoparticle valency in the detection of bacteria. Hence for these
studies, *Mycobacterium avium* spp. *paratuberculosis* (MAP) was used, which is smaller
than mammalian alveolar cells (0.3 µm Vs 50 µm) and has dimensions comparable to
other clinically relevant pathogens. Recently, we reported the magnetic-relaxation-
mediated detection of MAP in complex media, observing that at low bacterial
concentrations high $\Delta T2$ values were obtained, whereas at high bacterial concentrations
$\Delta T2$ decreased[97]. To elucidate this phenomenon, we prepared two MAP-specific MRnS
that carried different levels of anti-MAP antibodies. Specifically, two anti-MAP
nanoparticle preparations with different valency levels were prepared, by varying the
stoichiomeric ratio of anti-MAP antibody to Protein-G nanoparticles (5 µg anti-MAP:250
µL Protein-G nanoparticles Vs 0.5 ng anti-MAP:250 µL Protein-G nanoparticles. The
resulting anti-MAP MRnS had either high (4 anti-MAP molecules per nanoparticle on
average) or low (1 anti-MAP molecule per nanoparticle on average) antibody levels per
nanoparticle.

Through DLS, we observed that the anti-MAP MRnS yielded similar results to
those obtained with the nanoparticles for the FR-expressing mammalian cancer cells
(Table 6). Likewise, a valency-mediated differential behavior was also observed when we
quantified MAP in whole milk using magnetic relaxation and the anti-MAP MRnS,
following literature available protocols[97]. In particular, the low-anti-MAP MRnS
exhibited high $\Delta T2$ at low bacterial concentrations, whereas at high bacterial

concentrations ΔT2 decreased (Figure 30A). These findings were in line with the aforementioned studies using low valency nanoparticles and our earlier report on bacteria detection[97]. On the other hand, the high-anti-MAP MRnS demonstrated low ΔT2 at low MAP concentrations, but as the target's concentration increased ΔT2 increased (Figure 30B). Overall, the anti-FR and anti-MAP MRnS demonstrated similar quantifying capabilities, despite performing these studies in different matrices (blood Vs milk). Specifically, the high-anti-FR and high-anti-MAP nanoparticles can both quantify a region of two orders of magnitude (10^4 – 10^6 A549 cells and 10 – 1000 MAP CFUs respectively). Likewise, the low-anti-FR and low-anti-MAP nanoparticles can roughly quantify an equivalent region of two orders of magnitude (10^4 – 10^6 A549 cells and ~30 – 1000 MAP CFUs), suggesting that this behavior may be attributed to the nature and dynamics of the antibody – antigen interaction.

Table 6: Size distribution of the anti-MAP nanoparticles in the presence of various MAP concentrations.
Means ± SE

Nanoparticle	Diameter (nm)	MAP concentration	
		Low	High
	> 100	29.9 ± 0.5%	18.4 ± 0.7%
	< 100	70.1 ± 0.4%	81.6 ± 0.3 %
	>100	17.8 ± 0.2%	22.7 ± 0.9%
	< 100	82.2 ± 0.5 %	77.3 ± 0.6 %
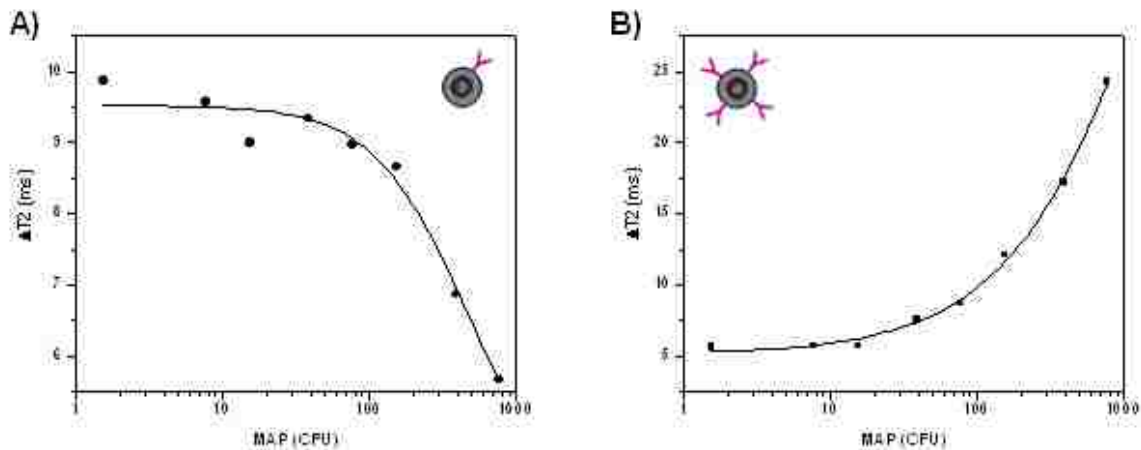
Figure 30: Relaxation-mediated detection of bacteria (MAP) in whole milk after a 60-minute incubation at room temperature.
A) Low-anti-MAP ($R^2 = 0.97$) and **B)** high-anti-MAP ($R^2 = 0.99$) nanoparticles. (Means $\pm$ SE; SE was within 1-2%, which cannot be depicted)

Based on the results of the mammalian cell and bacterial MRnS, we investigated if similar changes in the relaxation detection trends could be observed when a smaller target was used. For this purpose, we have utilized dextran-coated and galactose-carrying MRnS for the detection of the cholera toxin B (Ctb) subunit, as these carbohydrates are found on the GM1 ganglioside which is cholera toxin's cellular receptor. We anticipated that the galactose-carrying MRnS should have exhibited a different diagnostic pattern than the dextran-coated MRnS, as the latter nanoparticles' coating should intrinsically incorporate increased valency (multiple glucose moieties on the dextran-coated MRnS as opposed to a few conjugated galactose residues on the galactose-carrying MRnS). Experiments in water after a 5-minute incubation at room temperature revealed that the low-valency galactose-carrying MRnS demonstrated similar behavior to the other low valency MRnS (Figure 31A). On the other hand, the opposite trend was observed with the dextran-coated MRnS (Figure 31B). In order to confirm the interaction between Ctb and MRnS, we employed surface plasmon resonance analysis. Results indicated that both the

86

galactose-carrying and the dextran-coated MRnS interacted with Ctb (Figures 32B and 34D). Notably, the dextran-coated MRnS provided a more prominent plasmonic signal than the galactose-carrying MRnS, similar to what was observed via magnetic relaxation. Taken together, these data indicate that the multivalency of the dextran-coated MRnS is a critical contributor in the strong interaction between the MRnS and their target, and demonstrate the potential use of MRnS for the detection of toxins in environmental samples as part of bio-warfare and bioterrorism protection mechanisms.
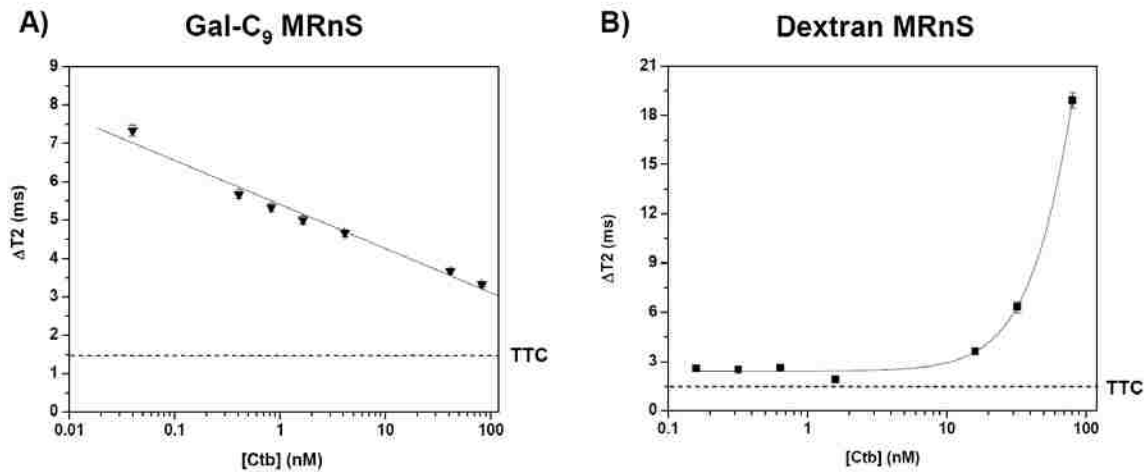
Figure 31: Relaxation-mediated detection of the Cholera toxin B (Ctb) subunit.
A) Galactose-carrying MRnS (Gal-C$_9$-IONP) and **B)** dextran-coated IONP (Dex-IONP). (Means ± SE; SE was within 1-2%).
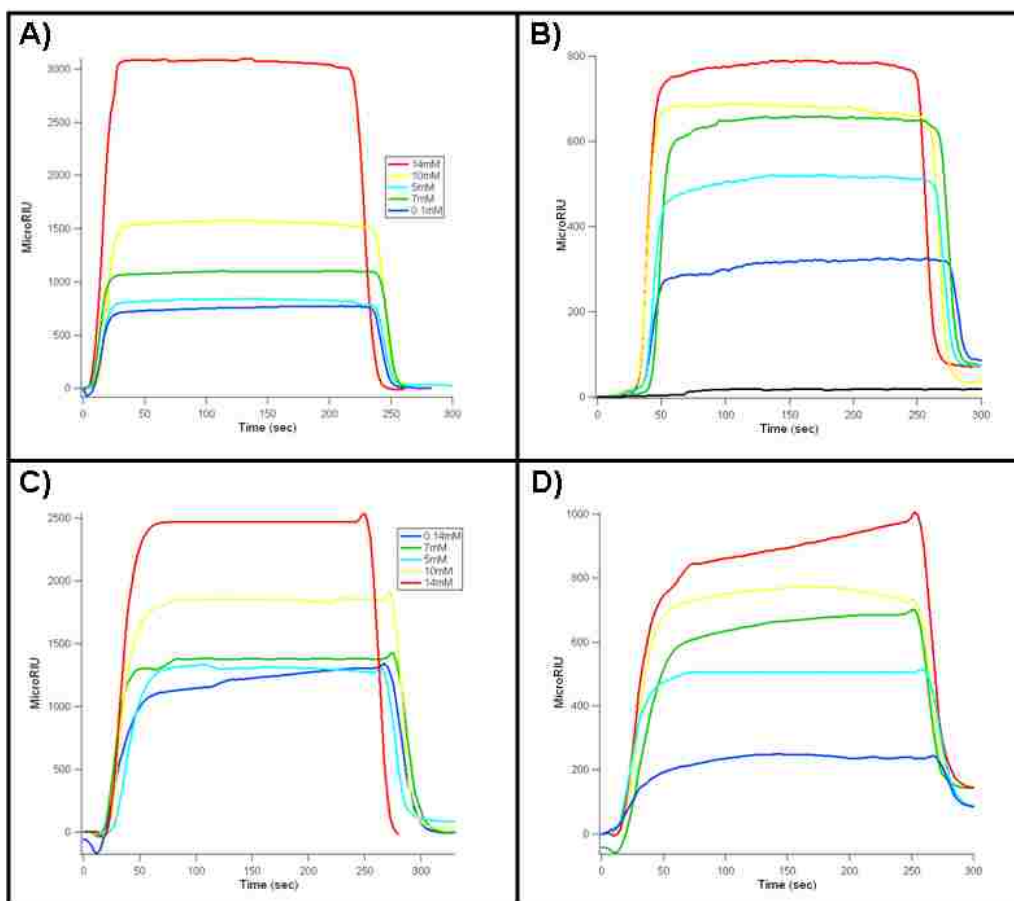
Figure 32: Surface Plasmon Resonance studies confirming the interaction between MRnS and Ctb.
A) Free nonanoic-acid-terminated galactose, **B)** galactose-carrying MRnS (Gal-C$_9$-IONP), **C)** free dextran (10kDa Dextran) and **D)** dextran-coated IONP (Dex-IONP).

Most importantly, these data suggest that the differential behavior of the nanoparticles is nanoparticle-valency-dependent, as neither the size of the ligands (small molecule Vs antibody) nor the size of the target (mammalian cell, bacterium, or toxin) governs the interaction of the nanoparticles with a target. This is supported by the magnetic relaxation, DLS and fluorimetry data, indicating that more high-valency nanoparticles associate with cells at high cell density, as opposed to lower cell density. If the nanoparticle size governed the interaction with cells, one would have expected

88

comparable levels of nanoparticles associating per target regardless of cell density and no differences between the low- and high-ligand nanoparticles detection patterns. Therefore, in light of these studies, our previously reported findings on bacteria detection[97] were indeed attributed to the nanoparticles' low valency. Taken together, the results of the bacterial studies corroborate what was observed with the mammalian cells (A549) and further support our hypothesis.

An interesting property of MRnS detection is that it is a nondestructive technique performed in suspensions causing no damage to the cells. Therefore, we reasoned that after MRnS identification, cells could be magnetically isolated and used for further assays. Particularly, we hypothesized that nanoparticles with high valency would be able to magnetically isolate a higher number of cells, due to the contribution of multivalent interactions between the nanoparticles and their corresponding cellular targets. Considering the folate nanosensors' MRnS detection sensitivity and their robustness as they do not carry any heat-labile antibodies, we studied the performance of the folate nanoparticle preparations with low and high multivalency to magnetically isolate lung cancer cells with an LS25 MACS® column (Miltenyi Biotec). Acknowledging the need for circulating tumor cell isolation and propagation in order to use these cells for further assays[99], samples of equal population A549 cells in PBS-diluted blood, which had been screened through magnetic relaxation, were effectively isolated with either the low-folate ([Fe] = 0.75 µg/µL) or high-folate nanoparticles ([Fe] = 0.75 µg/µL) and then propagated (Figures 33A-B). However, the nanoparticles with lower valency captured fewer cells than the high-folate nanoparticles, as indicated by the corresponding cell counts after a 24 h propagation at 37 $^{\circ}$C, 5% CO_2 (~45,000 cells for the low-folate nanoparticles Vs

~215,000 cells for the high-folate nanoparticles) (Figure 33C). In order to assess if the magnetic isolation of the cells compromised their cell viability, we utilized the MTT assay. Results indicated that the viability of the magnetically isolated cells was comparable to that of the corresponding controls (Figure 33D), demonstrating that the magnetic-relaxation-mediated detection and magnetic isolation of cells with the folate-carrying MRnS is non-destructive.
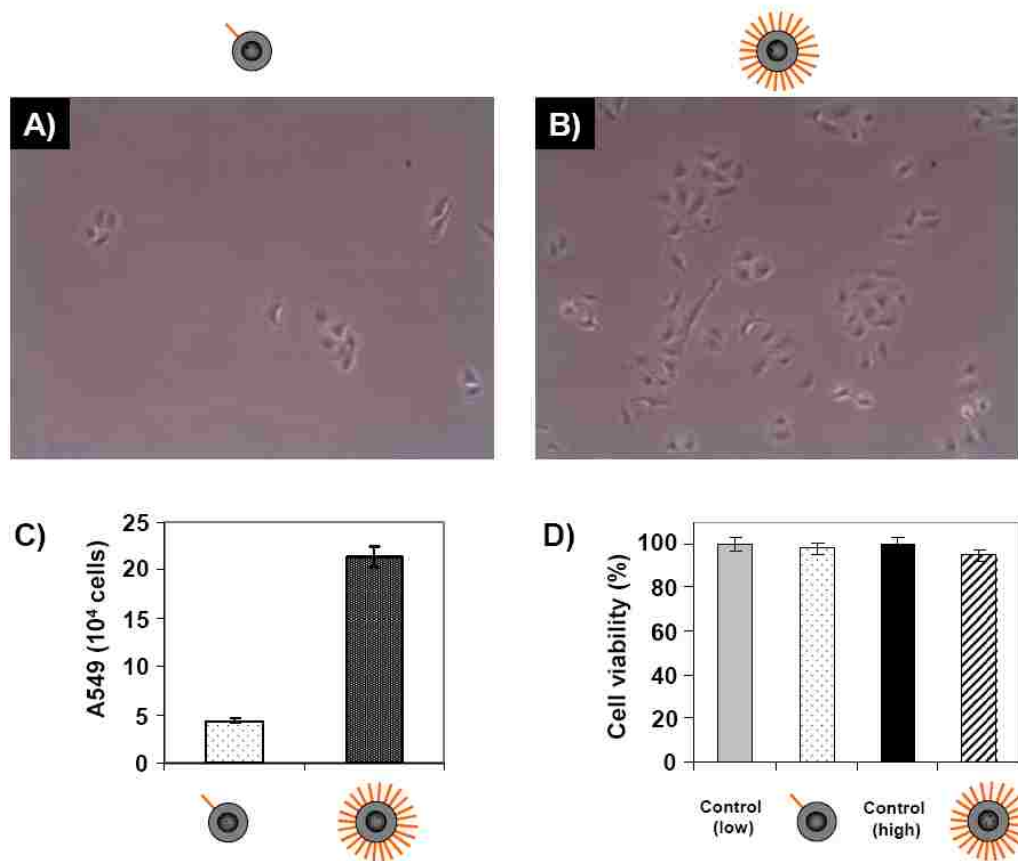
Figure 33: Nanoparticle-mediated magnetic isolation of FR-expressing cells.
A) Low- and **B)** high-folate nanoparticles. **C)** Hemocytomer-mediated quantification of the captured cells after 24 h propagation at 37 °C, 5% CO_2, **D)** Cell viability of cells magnetically isolated with the low- and high-folate nanoparticles (Control low – 45,000 seeded cells, Control high – 215,000 cells). (Means ± SE)

Next, we determined the magnetic cell-capturing efficiency of the high-folate nanoparticles, since these magnetic nanosensors exhibited enhanced detection sensitivity through magnetic relaxation and higher magnetic isolation of cells after analysis than the low-folate nanoparticles. Hence, after relaxation-mediated detection, the cell-containing PBS-blood samples were incubated with various iron concentrations of high-folate nanoparticles and then magnetically separated. Results showed that as little as 0.1 µg/µL Fe of folate nanoparticles captured viable A549 cells, reaching a plateau after 0.75 µg/µL Fe (Figure 34A-E). In contrast, when we used the non-functionalized nanoparticles, no cells were isolated (Figure 34F). Overall, these data indicate that our high-folate nanoparticle-based relaxation-mediated detection and subsequent magnetic isolation can be used in highly sensitive non-destructive assays.
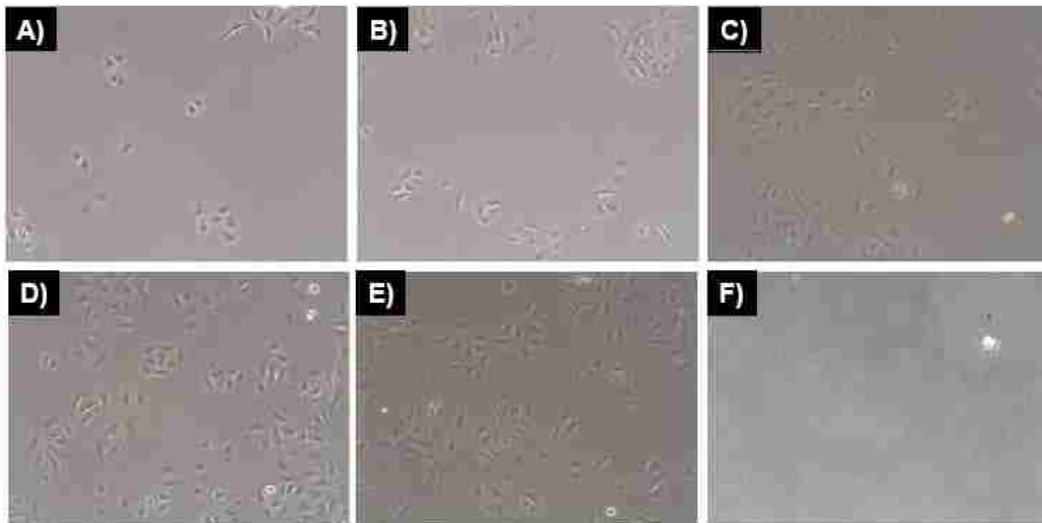
Figure 34: Folate nanoparticles facilitate the magnetic isolation of FR-expressing tumor cells.
The captured cells were grown at 37 $^\circ$C, 5% CO_2 atmosphere, and visualized 24 h after isolation. Isolation of folate-receptor expressing cells with high-folate nanoparticles (**A.** 0.1, **B.** 0.25, **C.** 0.5, **D.** 0.75 and **E.** 1 µg/µL Fe). (**F**) Absence of cell growth when non-functionalized nanoparticles were used (1 µg/µL Fe).

Lastly, we utilized iron oxide nanoparticles' intrinsic peroxidase activity[71, 72, 107] for the colorimetric high-throughput confirmation of the expression of folate receptor (FR) on the membrane of magnetically captured and propagated A549 cells (Figure 35A). For these studies non-fluorescent folate iron oxide nanoparticles were used. After magnetically isolating and re-growing the A549 cells, 500 of these cells were incubated with increasing concentrations of high-folate nanoparticles. We found that the A549 cells in the presence of H_2O_2 oxidized 3,3',5,5'-tetramethylbenzidine (TMB) (Figure 35B) in a nanoparticle-concentration-dependent fashion, indicating that the cells were viable and still expressing the FR. At nanoparticle concentrations above 1.2 Fe µg/µL, the absorbance reached a plateau. The control A549 cells, which were magnetically isolated with folate nanoparticles but incubated with non-functionalized nanoparticles, demonstrated nominal peroxidase activity. This indicates that the contribution of nanoparticles used for magnetic isolation is nominal towards the overall peroxidase activity. In contrast, the non-folate-receptor-expressing H9c2 cells lacked any peroxidase activity (Figure 35B), as the folate nanoparticles did not associate with these cells. Through flow cytometry, we confirmed the expression of the FR in the magnetically captured cells and its absence in the H9c2 control cells (Figure 36A), thus corroborating the findings of nanoparticle-facilitated peroxidase assay (Figure 35B).
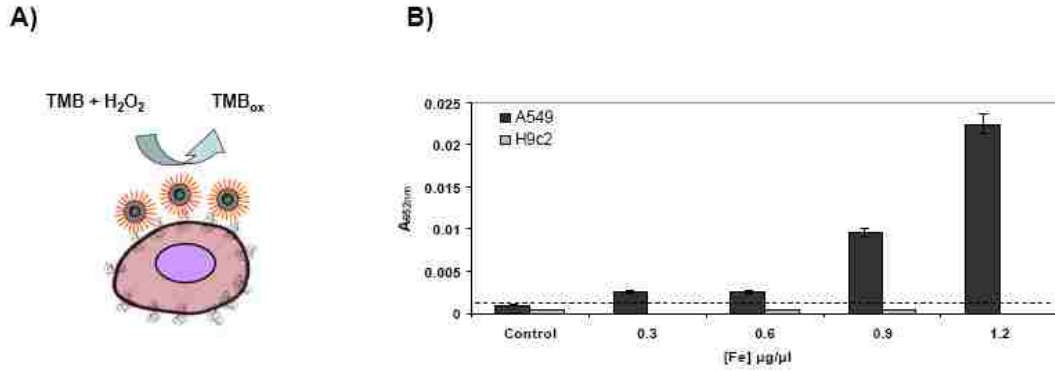
Figure 35: Folate nanoparticles confirm the expression of FR in vitro.
A) Detection of FR-expressing cells using the folate nanoparticles' peroxidase activity.
B) Carcinoma cells (500 A549 cells) oxidize TMB, whereas rat cardiomyocytes (H9c2)
do not. Cells were treated with non-functionalized nanoparticles (1.2 µg/µL Fe control) or
different concentrations of high-folate nanoparticles (Means ± SE).
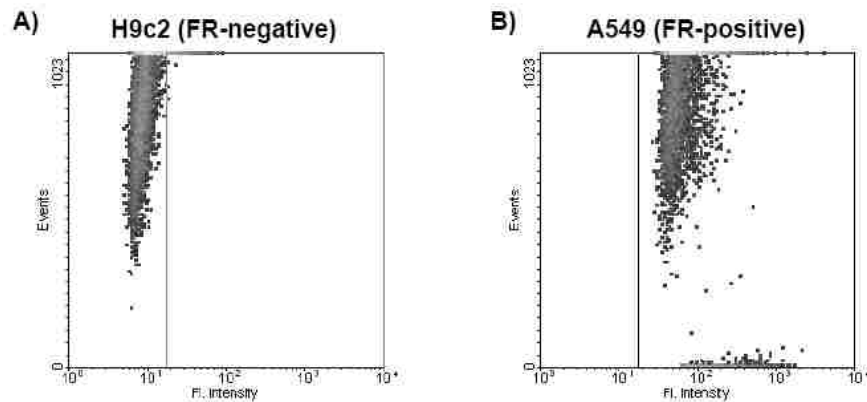
Figure 36: Flow cytometric determination of the expression of FR.
A) H9c2 and **B)** A549 cells.

Conclusion

➢ Small-molecule-carrying MRnS can rapidly detect a single cancer cell in blood, without sample processing.

➢ Receptor-mimicking MRnS can quickly sense the presence of toxins in aqueous media.

➢ MRnS can be used for the magnetic isolation of target cells for re-growth and further analyses.

➢ MRnS's intrinsic peroxidase activity can be used for the corroboration of the presence of molecular targets in cultured cells' plasma membrane through a high-throughput cellular ELISA format, with the use of a single reagent (MRnS) and hydrogen peroxide.

➢ The magnetic-relaxation-mediated detection pattern is governed by the MRnS's valency, but neither by the target's size, the sample's matrix nor the nature of the ligand.

Discussion

Nature widely employs highly selective multivalent interactions[87-96]. From enzymes and their substrates, to receptor – ligand pairs and antibody – antigen complexes, these associations are highly specific, despite being weaker than covalent interactions. For instance, the multivalent interaction between hemaglutinin of influenza virions and sialic acid moieties on bronchial epithelium cells mediates viral infection[92]. Specifically, recent studies indicate that multivalency, apart from participating in the initial attachment of a pathogen (i.e. virus, toxin) to a target cell, is critical for uptake via

94

complex, highly regulated endocytic processes, in addition to direct fusion[109]. In line with these observations, recently, a multivalent gold nanoparticle conjugate has been reported to transform a weakly binding and biologically inactive small molecule into a potent multivalent nanoagent that effectively inhibits HIV-1 fusion to human T cells[110].

Considering the importance of multivalency on molecular recognition events, it is critical to assess its role in the sensitivity and detection pattern of novel nanoparticle-based diagnostic methods. Hence, in this chapter we addressed the fundamental question of how the nanoparticle valency affects the interaction of MRnS with cells and what are the consequences in the magnetic-relaxation-mediated detection and magnetic isolation of these target entities. Our results indicate that nanoparticles with low valency switch from an assembled to a quasi-dispersed state as the target concentration increases, and this shift is accompanied with decrease in the ΔT2. On the other hand, nanoparticles with high valency move from a sparsely assembled to an extensive binding/clustered state, with a concomitant increase in ΔT2 that is observed during this transition. Interestingly, similar results were obtained when mammalian and bacterial cells were used, suggesting that the previously reported unique trend in the detection of bacterial cells was attributed to the different levels of antibodies conjugated to the nanoparticles[97, 107]. The aforementioned shift in the ΔT2 trend was also consistent when toxin-detecting MRnS were used, further supporting that it is the nanoparticle valency that modulates this behavior and not the target's size. Additionally, the shift in the relaxation detection pattern is valency-regulated, as neither the matrix (blood, milk or water), the ligand size (folate, galactose or anti-FR), nor the nanoparticle's coating (polyacrylic acid Vs dextran) affected the quantification trend. Hence, valency engineering should be a critical aspect

95

in the synthesis of sensitive MRnS and perhaps other nanoparticle-based diagnostic assays.

Another important element in the design of robust and affordable nanosensors is the utilization of non-labile and readily available probes. In our studies, nanoparticles with high small molecule valency (high-folate nanoparticles) facilitated single cell detection and quantification in whole erythrocyte-containing blood, outperforming their low valency counterparts (low-folate nanoparticles) and antibody-carrying nanosensors (low- or high-anti-FR nanoparticles). Therefore, as it was recently demonstrated that even a single metastatic cancer progenitor cell can successfully induce tumor formation[108], high-folate carrying nanoparticles may be used for the early detection of tumor cells in blood that overexpress the folate receptor. Furthermore, as the iron oxide nanoparticles can be easily conjugated via "click chemistry", other small molecules may be used for the synthesis of high-valency nanosensors, capable of detecting rare circulating tumor cell in blood that may express other biomarkers. Small molecules, apart from being cheaper and more robust than antibodies, can offer comparable specificity and can be easily utilized for the engineering of the nanoparticle valency, due to their minimal steric hindrance. Since small-molecule-carrying nanoparticles can sense single cells, as opposed to antibody-carrying nanoparticles, the wider utilization of small molecules in molecular diagnostics is expected. For instance, bacteria can be targeted with small molecules screened from combinatorial libraries, leading to the development of bacterium-specific small-molecule-carrying nanoparticles, which can achieve reliable and sensitive detection at the points-of-care and in the developing world[58].

96

CHAPTER V: ASSESSMENT OF BACTERIAL METABOLISM AND DRUG RESISTANCE VIA MRnS

Introduction

In the last 20 years, there has been a dramatic increase in the emergence of antibiotic-resistant bacteria, leading to elevated bacterial pathogenesis at the global level [111, 112]. In particular, the emergence of drug resistant strains of *Mycobacterium tuberculosis* (XDR-TB) and the increased occurrence of methicillin-resistant *Staphylococcus aureus* (MRSA) infections, indicate that drug resistance is a major public health issue[111, 112]. Recent reports indicate that in the United States MRSA infections cause more deaths than HIV/AIDS, whereas the development of new antibiotics has significantly slowed down since the early 1990s[111-113]. Therefore, developing sensitive and cost-efficient detection systems that can quickly identify if (i) a particular bacterium is resistant to antibiotics, (ii) the pharmacological agents which the microorganism is susceptible to and (iii) the agents' appropriate effective dosage is vital for successful treatment and prevention of epidemics. Traditionally, the determination of antimicrobial susceptibility to antibiotics is facilitated after isolation of the microorganism and examination of its growth in media containing various antimicrobial agents, in a process that can take up to 48 hours[114, 115]. Hence, developing fast and accurate antimicrobial susceptibility assays is important for the clinic and the pharmaceutical industry.

Nanotechnology offers a unique alternative for the development of detection methods for bacterial targets that require less preparation time and smaller sample volumes, while offering enhanced sensitivity and faster detection kinetics[24, 33, 75, 76, 97]. In

particular, nanosensors that not only directly detect the presence of a specific pathogenic agent, but can also make an indirect detection through the assessment of the pathogen's metabolic activity, e.g., via the monitoring of the rate of consumption of nutrients in solution, would be of great utility. The development of such nanosensors will be of significant importance, because they will be able to interrogate whether the pathogen is still metabolically active and reproducing in the presence of a particular antibiotic. Currently, most contemporary nanoparticle-based immunoassays cannot distinguish between metabolically active, senescent and dead pathogens[97, 116].

Considering these, we first utilized a novel gold nanoparticle-based method for the assessment of bacterial susceptibility via surface plasmon resonance shifts in transparent media. However, as microorganisms, like *Staphylococcus epidermidis* and *Neisseria* spp. among many others, can be present in the blood of infected patients (septicemia), requiring isolation and growth in blood-containing media, we designed MRnS for the assessment of antimicrobial susceptibility in blood[117, 118]. We reasoned that MRnS could be a more robust system, quickly determining bacterial susceptibility independent of the solution's optical properties via water relaxation[50, 52]. According to the literature, it is widely acknowledged that a major benefit of using magnetic relaxation methods is that molecular detection can be achieved in opaque media, such as cell lysates, tissue extracts and complex biological fluids, notably blood, with high specificity and sensitivity[50, 52, 97]. Therefore, we hypothesized that bacterial-susceptibility-monitoring MRnS could be designed to differentially respond to the presence of various concentrations of nutrients, such as complex carbohydrates (e.g. starch). Although superparamagnetic nanoparticles have been used as magnetic relaxation sensors for the

98

detection of various targets[50-53, 70, 97, 119-122], these nanoprobes have not been previously utilized for the detection of metabolic activity, which might lead to the potential development of nanosensors capable of determining antimicrobial susceptibility in complex media.

Materials and Methods

Synthesis of Dextran-coated Gold Nanoparticles.

To 100 ml of a 1% aqueous solution of Dextran T – 10 (10 kDa, GE/Pharmacosmos), 1 ml of 10^{-2} M HAuCl$_4$ (Sigma) was added and stirred while heating. The solution was allowed to boil until its color turned pink, indicating the formation of gold nanoparticles in solution.[123]. The reaction mixture was boiled for 30 more minutes. Then, the solution was cooled down to room temperature and washed three times with distilled water using an Amicon 8200 cell (Millipore ultrafiltration membrane YM – 30 kDa).

Characterization.

Transmission electron microscopy (TEM) was done using a FEI Tecnai F30 instrument on dextran-coated Au-NP (Dex-Au-NP) samples spotted on a carbon-coated copper grid. Dynamic light scattering (DLS) studies were done using a PDDLS CoolBatch 40T instrument using Precision Deconvolve 32 software. FT-IR experiments were done in a Perkin Elmer Spectrum 100 FTIR spectrometer using samples spotted on plastic cover slips.

UV-vis studies with Dex-Au-NP and *E. coli*.

E. coli (strain 8739 from ATCC, 10^6 CFU) was grown in MH broth (DIFCO^{TM}, BD), for 2 hours at 37°C in the presence or absence of ampicillin. Each nanoparticle solution (400

µl Dex-Au NP in 600 µl distilled water) was spiked with 10 µl of specimen and examined on a Cary 300 UV-Visible spectrophotometer (Varian Inc.). Addition of Con A (Sigma, 10 µgml^{-1}) resulted in changes in the absorption profiles of the Dex-Au-NP, which were monitored with the Cary 300 UV-Vis spectrophotometer, at various time intervals.

High-throughput determination of antimicrobial susceptibility using Dex-Au-NP.

In each well of the 96-well plate (Corning) 100 µl of Dex-Au-NP (40:60 v:v) were added. Then 1 µl aliquots of each samples with either sterile MH medium, *E. coli* grown in 64 µg ampicillin, 2 µg ampicillin, 0 µg ampicillin, or heat-inactivated *E. coli* were added in triplicates in various wells of the plate. All bacterial cultures were grown as stated above, whereas heat inactivation of *E. coli* was achieved by autoclaving the culture immediately after the bacteria (10^6 CFU) were added into the MH broth, preventing any bacterial metabolism and proliferation. The absorbance of each well was monitored on a Synergy HT microplate reader (BioTek) prior and after Con A addition (10 µg/ml final concentration). As all wells had the same surface plasmon peak prior the addition of Con A, the wavelength difference ($\Delta\lambda$) was denoted as the wavelength with maximum absorbance of the sterile control minus the wavelength with maximum absorbance of the specimen, both under Con A-induced clustering. Control samples of sterile medium or heat-inactivated bacteria had a $\Delta\lambda$ equal to zero and were depicted as purple in our color map. Samples that exhibited $\Delta\lambda$ values below 4 nm indicated the absence of bacterial growth, suggesting the presence of an effective inhibitory antibiotic concentration, and were depicted as green. Finally, samples with $\Delta\lambda$ values above 4 nm indicated that bacterial growth occurred, due to either absence of antibiotic or low antibiotic concentration, and were denoted as red.

Reagents for the synthesis of MRnS.

All the reagents used were of AR (Analytical Reagent) grade. Nitrogen-purged double-distilled water was used throughout the reaction. Iron salts, $FeCl_2.4H_2O$ and $FeCl_3.6H_2O$, were obtained from Fluka. Dextran (MW 10kDa) was received from Amersham. TEOS: tetraethylorthosilicate (Fluka), APTS: 3-(amino-propyl)triethoxysilane (Aldrich) and THPMP: 3-(trihydroxysilyl)propylmethyl-phosphonate (Gelest Inc) were used as received from the suppliers.

Synthesis of MRnS.

The dextran-coated iron oxide nanoparticles were prepared as previously reported in the literature[52]. The aminated silica-coated iron oxide nanoparticles were prepared using a previously published protocol[124], with modifications in order to yield stable nanoparticles via a water-based synthesis. Specifically, iron oxide nanocrystals were formed via the alkaline precipitation method, by mixing a solution of iron salts (0.202 g $FeCl_2.4H_2O$, 0.488 g $FeCl_3.6H_2O$, 88.7 μL HCl in 2 mL distilled water) with an ammonium hydroxide solution (830 μl NH_4OH in 15 mL distilled water). Then, 20 seconds after the initiation of the iron oxide nanocrystal formation, a TEOS-THPMP-APTS solution was added (6180 μL THPMP, 2680 μL TEOS, 670 μL APTS) under continuous vortexing. The as-synthesized nanoparticle suspensions were centrifuged to remove large particles. Both the amino-silica- and dextran-coated nanoparticles were washed several times with distilled water and concentrated through an Amicon 8200 cell (Millipore Ultrafiltration membrane YM – 30 kDa). Finally, the nanoparticle suspensions were stored at 4 ^{o}C until further use.

Conjugation of Concanavalin A to silica-coated iron oxide nanoparticles.

Two milliliters of aminated silica-coated iron oxide nanoparticles (R2=225 $mM^{-1}s^{-1}$, [Fe] = 0.47 mg/ml) were used for the conjugation of Con A to the nanoparticles' surface. Initially, in 1 mL of cold MES buffer (0.1M, pH 6.0) 4.8 mg EDC (Pierce) and 3 mg NHS (Pierce) were dissolved. Then, 2 mg of lyophilized Con A (Sigma) were dissolved in 2 mL cold MES buffer (0.1M, pH 6.0). Subsequently, the Con A solution was mixed with the EDC/NHS solution, followed by a 3-minute low-speed rotary mixing at room temperature. Finally, the aminated silica-coated iron oxide nanoparticles were added to the Con A (amine-reactive NHS-ester form) solution, followed by periodical rotary mixing at low speed and storage at 4 ^{o}C. The resulting Con A-conjugated silica-coated iron oxide nanoparticles were purified from any unbound protein via magnetic separation using an MES buffer-equilibrated (0.1M) LS25 MACS$^{®}$ column (Miltenyi Biotec).

MRnS characterization.

Dynamic light scattering (DLS) studies were done using a PDDLS CoolBatch 40T instrument using Precision Deconvolve 32 software. Iron concentration was determined spectrophotometrically after acid digestion of the nanoparticles' suspension, whereas R2 relaxivity measurements were obtained using a 0.47T mq20 NMR analyzer (Minispec, Bruker, Germany). Starch sensing with the magnetic nanoparticles was performed using serial dilutions of starch (~75% amylopectin, ~25% amylose, S-516, Fisher) in non-starch containing MH broth (DIFCO^{TM}, BD). The concentration of Con A conjugated to the silica-coated iron oxide nanoparticles was determined through the BCA assay, in accordance to the manufacturer's protocol (Pierce), after magnetic separation of the

nanoparticle suspension using an MES buffer-equilibrated (0.1M) LS25 MACS® column (Miltenyi Biotec).

Bacterial cultures.

In order to investigate if the dextran-coated iron oxide nanoparticles can monitor the starch utilization due to bacterial metabolic activity, different populations of *Escherichia coli* (strain 8739 from ATCC) were grown in starch-containing MH broth (DIFCO^{TM}, BD) for 2 hours at 37 ^{o}C. For determination of the minimum inhibitory concentration, *Escherichia coli* (10^6 CFU), *Serratia marcescens* (ATCC, 10^6 CFU) and *Shigella sonnie* (strain 9290 from ATCC, 10^6 CFU) were grown in a starch-containing MH broth (DIFCO^{TM}, BD), for 2 hours at 37°C in the presence or absence of ampicillin. For determination of MIC in blood, bacterial stocks (10^6 CFU) were grown in the presence or absence of ampicillin in a 5%-blood-supplemented starch-containing MH broth, for 2 hours at 37 ^{o}C. Defibrinated sheep blood was obtained from the Colorado Serum Company, simulating bacterial isolation and growth in typical blood agar plates. For studies requiring heat inactivation, *E. coli* bacteria were autoclaved in the culture tubes for 10 minutes. Upon incubation or inactivation, all bacterial stocks were placed in a Fisher Isotemp freezer (Fisher Scientific, Hampton, NH), until further use.

Sample preparation for relaxation measurements.

Aliquots of 10 µl (either of the aforementioned bacteria or media) were added into 190 µl nanoparticle working solution (0.02 µg/µL in Ca^{2+}/Mg^{2+}-free 1X PBS for both the dextran-coated and Con A-conjugated polysaccharide nanosensors). For the dextran-coated polysaccharide nanosensors, 10 µL Con A (Sigma, 1 µg/µl) were added in order to induce nanoparticle clustering.

Measurement of proton relaxation times.

Spin-spin relaxation times (T2) were measured using a 0.47 T mq20 NMR analyzer (Minispec, Bruker). T2 values were obtained before and after addition of the aliquot, and through the time course of the study. For the quantification of starch, we prepared serial dilutions of sterile starch-supplemented MH broth (DIFCO[TM], BD) in sterile non-starch-supplemented MH broth (DIFCO[TM], BD). Subsequently, the dextran-coated polysaccharide nanosensors' sensitivity and dose response to the analyte (starch) was evaluated, by monitoring the changes in the spin-spin relaxation time. In this case, $\Delta T2$ is denoted as the difference between the relaxation time of the solution's initial dispersed state before addition of the MH broth aliquot ($T2_{in}$) and the solution's T2 after addition of the MH broth aliquot (T2'). Thus, $\Delta T2 = |T2' - T2_{initial}|$. For all other measurements, including *E.coli*'s metabolic activity monitoring via carbohydrate quantification and magnetic relaxation-mediated antimicrobial susceptibility assessment, $\Delta T2$ is denoted as the difference between the T2 of a sample and the corresponding sterile control sample ($\Delta T2 = |T2_{sample} - T2_{control}|$), where the sterile control was starch-containing MH which is used for the growth of these microorganisms. The sterile control used for the nanoparticle-mediated antimicrobial susceptibility assessment in blood was 5%-blood-supplememted starch-containing MH broth. All experiments and measurements were carried out in triplicate and data were expressed as mean ± standard error, unless otherwise denoted. Response curves were obtained by fitting the data on a sigmoidal curve, using Origin 7.5 (OriginLab, Northampton, MA). Statistical analyses were performed on SPSS 11.5 (SPSS Inc., Chicago, IL).

Broth dilution assay for determination of Minimum Inhibitory Concentration (MIC).

Broth dilution assay (standard method for measuring MIC) was achieved by inoculating serial dilutions of ampicillin in sterile starch-containing MH broth, with either *E. coli*, *S. marcescens*, or *S. sonnei* (10^6 CFU), followed by a 24-hour long incubation at 37°C. Bacterial growth was assessed based on the broth's turbidity, where absence of turbidity was an indicator of successful antimicrobial susceptibility. The lowest ampicillin concentration where the MH broth is clear indicates the minimum concentration of ampicillin that can successfully inhibit bacterial growth[114, 115].

Results

Initially we developed a spectrophotometric antimicrobial susceptibility assay, based on the concanavalin-induced self-assembly of dextran-coated gold nanoparticles (Dex-Au-NP) in response to bacteria's metabolic state. Dex-Au-NP have been previously used as nanosensors for the detection of glucose[125], due to the nanoparticles' ability to cluster in the presence of Concanavalin A (Con A), a protein with high affinity towards carbohydrates[125, 126]. We reasoned that in the (i) absence of an inhibitory compound, (ii) presence of an ineffective antibiotic, or (iii) at non-inhibitory antibiotic concentrations, the bacteria will proliferate, reducing the levels of nutrients, such as carbohydrates in solution. Under these conditions, Con A would facilitate the assembly of the Dex-Au-NP to carbohydrates on the surface of the growing bacterial population, creating a semi-dispersed state and favoring formation of small clusters (Figure 37A). Meanwhile, in the case of an effective antibiotic, there would be suppression of the bacterial metabolism with corresponding reduction in the uptake of carbohydrates by the bacteria. Thus, the

excess complex carbohydrates in solution presumably would promote the concanavalin-induced clustering of Dex-Au-NP. This would result in the formation of larger Au-nanoassemblies, leading to a significant red-shift of the surface plasmon band (Figure 37B), that is proximal to the surface plasmon band of a sterile solution containing Con A-assembled Dex-Au-NP (Figure 37C).
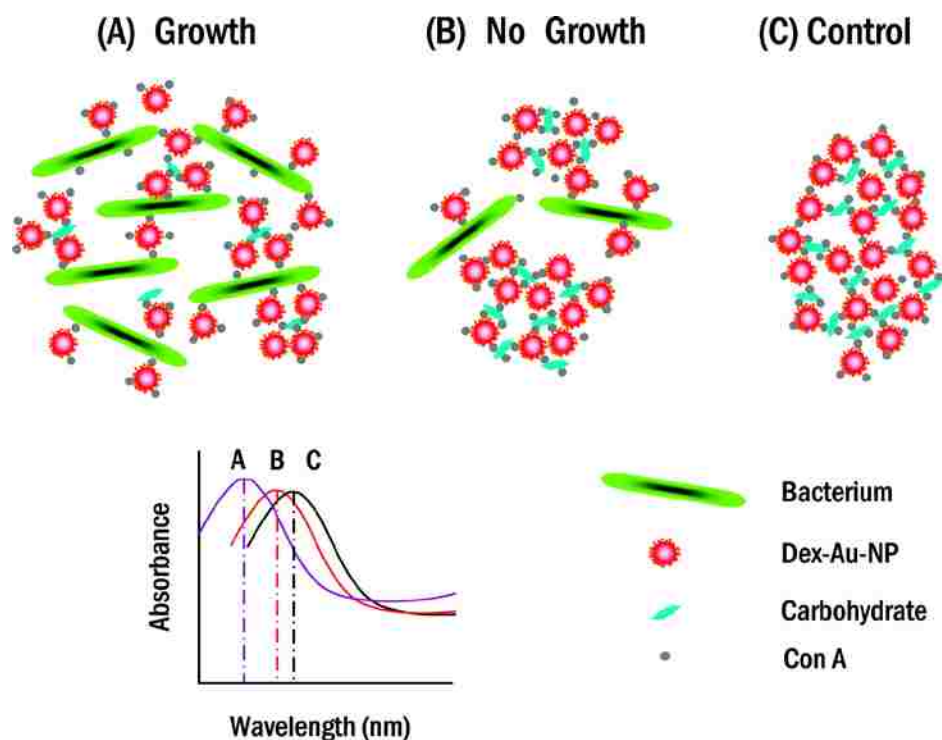
Figure 37: Proposed model for Dex-Au-NP-mediated antimicrobial susceptibility assessment.
In the absence of bacterial carbohydrate uptake (**B**) or in sterile conditions (**C**), addition of Con A results in the formation of large nanoassemblies and large shifts in the surface plasmon band, due to the presence of free carbohydrates in solution. During bacterial growth (**A**), the increased population of bacteria utilizes more carbohydrates, resulting in a decrease in the amount of free carbohydrates and a corresponding decrease in the size of the gold nanoclusters, causing lower shifts in the plasmonic band.

For the spectrophotometric assessment of antimicrobial susceptibility, we used dextran-coated gold nanoparticles. Dynamic light scattering results (Figure 38A) showed that the Dex-Au-NP preparation was composed of monodispersed nanoparticles of 25 ± 5 nm in size, as confirmed by TEM, which showed spheres with diameter in the range of 22 $\pm$ 3 nm (Figure 38A, inset). The Dex-Au-NP were highly stable in water for up to a year of storage at 4°C, and were easily suspended in a solution containing sterile MH bacterial medium with no precipitation. In our synthetic procedure, dextran served the dual role of

107

a reducing and a stabilizing agent. Dextran reduces Au^{III} to Au^0 and substitutes the role of citrate in previously reported preparations[127, 128]. Indeed, FTIR data showed that some of dextran's hydroxyl groups got oxidized to aldehyde groups, a process that is coupled to the reduction of Au^{III} to Au^0 (Figure 38B). Finally, the evolved gold nanoparticles were stabilized by the dextran in solution, again substituting citrate's role. The presence of dextran peaks in Dex-Au-NP demonstrated that dextran was an integral part of the as-synthesized nanoparticles, providing stability to them.
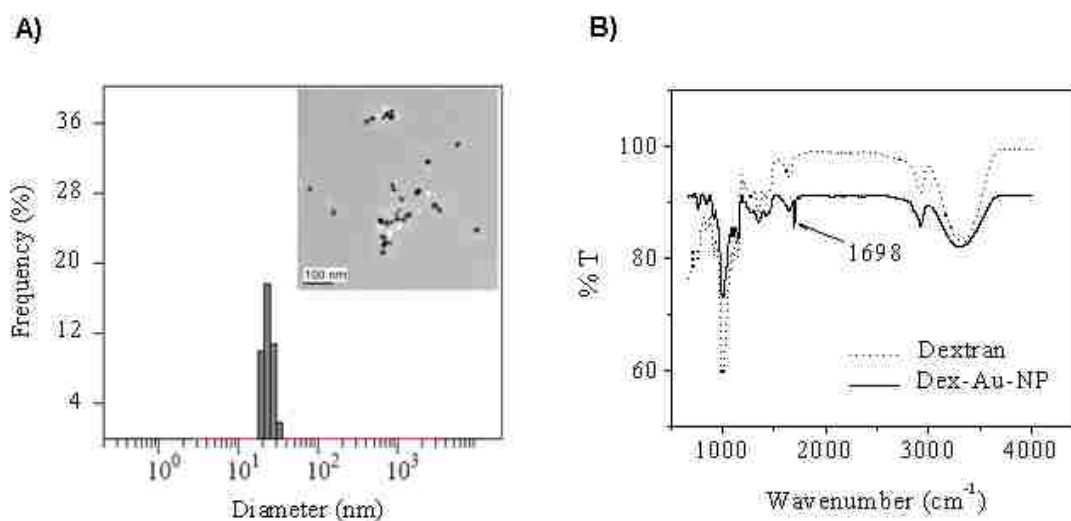
Figure 38: Characterization of the Dex-Au-NP.
A) Particle size distribution with corresponding TEM image (inset). **B)** FT-IR spectra of free dextran and Dex-Au-NP. The peak at 1698 cm^{-1} represents the formation of aldehyde groups on Dex-Au-NP.

UV-vis analysis of the Dex-Au-NP in either PBS or sterile MH medium revealed the characteristic profile for gold nanoparticles (Figure 39A) with an absorption maximum at 531 ± 0.1 nm, which was unaffected when the nanoparticles were in the presence of increasing amounts of antibiotic, *E. coli* bacteria or a combination of both

(Table 7, Figure 39B). No clustering or precipitation was observed for weeks, which supports the idea that the nanoparticles are stable in media containing nutrients (complex carbohydrates) and bacteria. However, when Con A (10 µg/ml) was added to the nanoparticles, a significant red-shift was observed, with a maximum surface plasmon peak at 566 ± 0.3 nm (Table7) due to cluster formation, as confirmed by DLS. Notably, the presence of the antibiotic in sterile MH medium, which was free from any bacteria, did not affect the nanoparticles' absorption profile under Con A-induced clustering conditions (Figure 40).
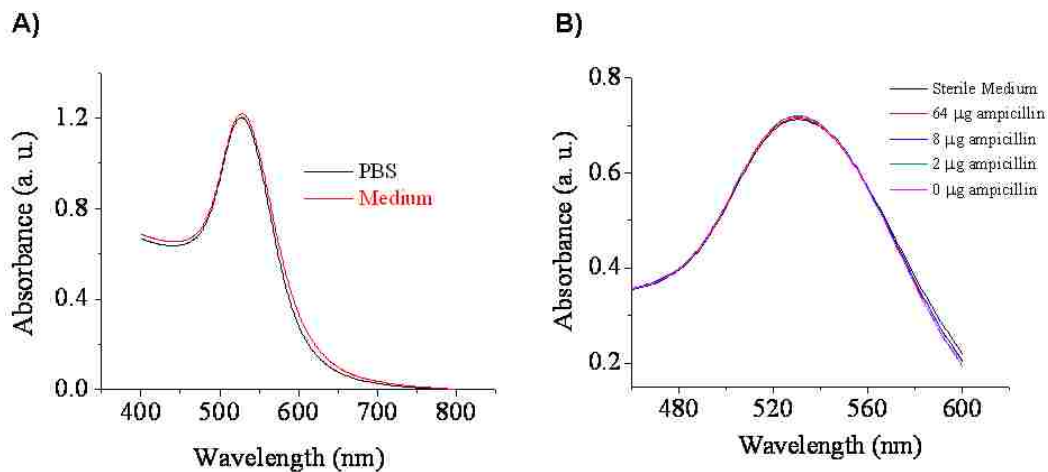
Figure 39: UV-vis spectroscopic characterization of Dex-Au-NP in culture media.
A) UV-Visible spectra of Dex-Au-NP in the absence of Con A (non-assembled conditions). **B)** In the absence of Con A, the Dex-Au-NPs were in a non-assembled state, exhibiting the same spectral characteristics, regardless of the presence of bacteria and antibiotic. The samples with ampicillin (64, 8, and 2 µg) and the bacterial growth control (0 µg ampicillin) contained aliquots from liquid cultures initially inoculated with 10^6 CFU *E. coli*.

Table 7: Absorption maxima of Dex-Au-NP in various media with or without E. coli in the presence of ampicillin (Amp).
Means ± SE. [a] Represents the difference between the absorption maxima of the control sample (MH Broth + Con A) and the test sample.

Dex-Au-NP in various media	λ_{max} (nm)	$\Delta\lambda$[a] (nm)
PBS	531 ± 0.1	-
MH Broth	531 ± 0.1	-
MH Broth + 64 µg Amp + *E. coli* (10^6)	531 ± 0.1	-
MH Broth + Con A	566 ± 0.3	-
MH Broth + Con A + *E. coli* (10^6) + 64 µg Amp (inhibitory)	564 ± 0.4	2
MH Broth + Con A + *E. coli* (10^6) + 2 µg Amp (non inhibitory)	557 ± 0.6	9
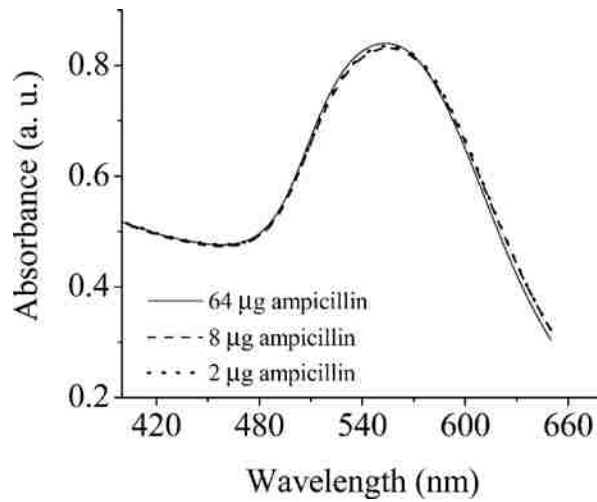
Figure 40: Dex-Au-NP's spectral characteristics in sterile MH broth under Con A-induced clustering.

Next, we examined whether bacterial metabolic activity can be assessed via the Dex-Au-NP's surface plasmon band changes. In these studies, *E. coli* (10^6 CFU) were incubated for 2 hours at 37 °C in MH broth, in the presence of various concentrations of ampicillin. Then, 10 µl aliquots of these samples were added into the Dex-Au-NP solution. As described before, despite the presence of bacteria and antibiotic, the samples exhibited identical absorption spectra, under non-assembled conditions (Figure 39B). However, after addition of Con A (10 µg/ml) and a 30-minute incubation at 25 °C, significant changes were observed (Figure 41). The surface plasmon band of a sample containing a low, non-inhibitory, concentration of ampicillin (2 µg) was 557 ± 0.6 nm, corresponding to a difference ($\Delta\lambda$) of 9 nm between the control and the sample (Table 7, Figure 41A). Similar differences were also observed in samples containing bacteria actively proliferating in the absence of the antibiotic. The observed 9 ± 0.6 nm difference is the result of Dex-Au-NP re-dispersion due to an increase in the bacterial population and subsequent decrease of available free carbohydrates. However, when a higher and inhibitory amount of ampicillin (64 µg) was used, the surface plasmon of the nanoparticles was 564 ± 0.4 nm, corresponding to a difference of only 2 nm (Table 7, Figure 41B). Under these conditions, the surface plasmon band was closer to that of the sterile control, due to the higher amount of free carbohydrates that have not been utilized by the bacteria as their metabolism was suppressed, hence promoting extensive concanavalin-induced Dex-Au-NP clustering. The presence of large gold nanoclusters in the sample with inhibitory antibiotic concentration was confirmed by DLS studies. Specifically, at 64 µg ampicillin, 60% of the Con A-induced clusters were 350 nm or larger in diameter, whereas the remaining 40% had diameters below 100 nm. In contrast,

at the low non-inhibitory antibiotic concentration (2 µg), only 40% of the Con A-induced clusters were 350 nm or larger, while 60% had diameters of 100 nm or smaller. These results confirm that under conditions of bacterial growth the gold nanoclusters were smaller than those formed under inhibition or absence of bacterial growth and substantiate the observed changes in surface plasmon.
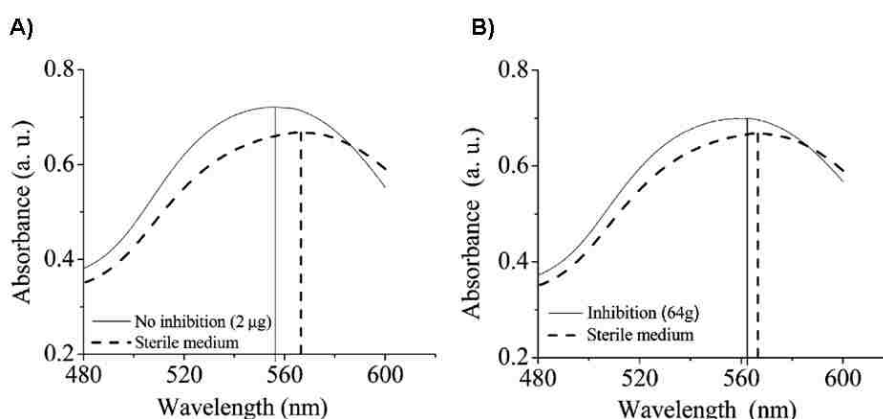
Figure 41: Distinct plasmonic shifts of Dex-Au-NP under Con A-induced clustering conditions in bacterial cultures supplemented with antibiotics.
A) Bacterial growth in the presence of the non-inhibitory ampicillin concentration of 2 µg. **B)** Absence of bacterial growth corresponding to the inhibitory 64 µg ampicillin concentration.

We then asked if one could use the developed Dex-Au-NP in antimicrobial susceptibility assays. The goal of an antimicrobial susceptibility test is to predict the *in vivo* success or failure of a particular antibiotic therapy by measuring the growth response of an isolated organism in the presence of a particular antimicrobial agent[114]. Results are expressed in terms of the antibiotic's minimum inhibitory concentration (MIC), which is defined as the antibiotic's minimum concentration that can inhibit the growth of an

isolated microorganism. Accurate determination of the MIC is critical for the identification of an effective compound and its' administration at dosages that prevent adverse side effects, such as renal toxicity. Considering that current MIC determination methods, such as broth dilution or disk diffusion assays, yield results in approximately 24 hours[115], we examined if our Dex-Au NP-based method can yield similar results but faster and without sacrificing reliability. For these studies, *E. coli* (10^6 CFU) were incubated for only 2 hours at 37 ^{o}C in MH broth, in the presence of different concentrations of ampicillin. Then, aliquots of these samples were incubated with Dex-Au-NP for 30 minutes at 25 ^{o}C, in the presence of Con A (10 µg/ml). The ampicillin MIC for this *E. coli* strain was found to be 8 µg, because at this concentration the surface plasmon band shift of the nanoparticles was statistically different from that of the sample containing bacteria growing in the absence of antibiotic (Figure 42A). Confirmation of our results was achieved via a broth dilution assay[115]. Bacterial growth was assessed based on the broth's turbidity, where absence of turbidity was an indicator of successful antimicrobial susceptibility. The lowest ampicillin concentration as determined by this method was also 8 µg (Figure 42A). This concentration was identical to the Dex-Au-NP/Con A-determined MIC, though the nanoparticle-based method yielded the same results within 3 hours as opposed to 24 hours.
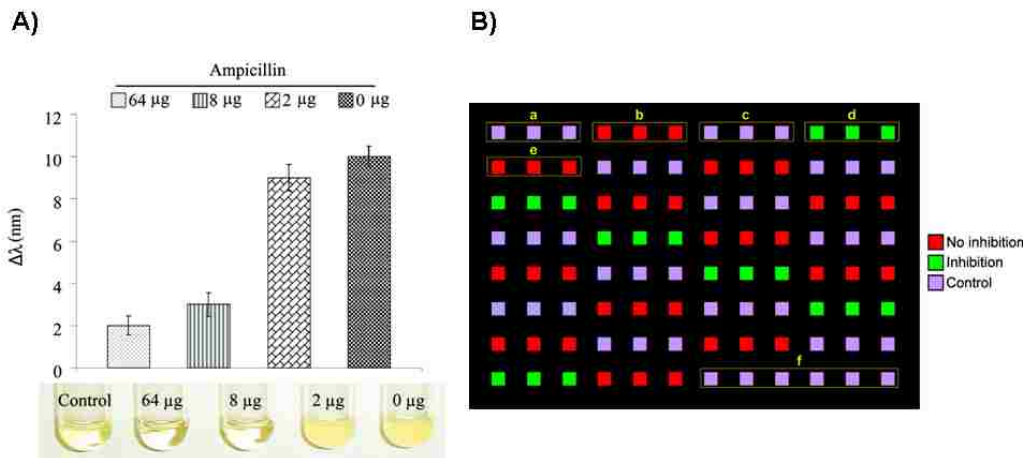
Figure 42: Spectrophotometric determination of antimicrobial susceptibility using Dex-Au-NP.
A) Determination of the minimum inhibitory concentration using the surface plasmon peak shift of Dex-Au-NP and confirmation via the turbidity method (numbers indicate the amount of ampicillin) (Means ± SE). **B)** Determination of minimum inhibitory concentration in high-throughput format using Dex-Au-NP and Con A. Purple squares indicate absence of bacterial metabolism ($\Delta\lambda = 0 \pm 0.4$ nm), green areas demonstrate inhibition of bacterial metabolism ($\Delta\lambda = 2 \pm 0.4$ nm), and red wells show active bacterial metabolism ($\Delta\lambda = 9 \pm 0.6$ nm). Group: (a) Sterile MH broth, (b) *E. coli* (10^6 CFU) grown in the absence of ampicillin, (c) heat-inactivated *E. coli* (10^6 CFU) in MH broth, (d) and (e) *E. coli* (10^6 CFU) grown in the presence of 64 and 2 µg ampicillin, respectively. Following wells include replications of these groups, obeying the above pattern. Group (f) consists of additional control samples, similar to (a).Absence of bacterial growth corresponding to the inhibitory 64 µg ampicillin concentration.

In subsequent studies, we investigated the potential use of Dex-Au-NP for the determination of antimicrobial susceptibility in high-throughput format. In these studies, samples of heat-inactivated *E. coli* (10^6 CFU) and *E. coli* (10^6 CFU) grown in the presence or absence of ampicillin were screened with the Dex-Au-NP on a 96-well plate using a microtiter plate reader. Addition of Con A, followed by a 30-min incubation at 25 ^{o}C, resulted in distinct changes of the surface plasmon band, similar to those described above with standard errors of less than 0.6 nm. This allowed the categorization of the samples in inhibitory (64 µg ampicillin; $\Delta\lambda < 4$ nm) or non-inhibitory (2 and 0 µg

ampicillin; $\Delta\lambda > 4$ nm) cohorts, denoted as green and red areas respectively (Figure 42B). Also, the wells with heat-inactivated bacteria had the same absorption maximum with the sterile medium ($\Delta\lambda = 0$ nm), collectively classifying these samples as control and denoting them as purple. In control studies, high-throughput spectrophotometric screening of 100 µl aliquots of bacterial cultures (10^6 CFU) incubated for 2 hours in the presence of ampicillin did not reveal significant changes in the culture's absorbance at 500 nm (Figure 43), indicating that the Dex-Au-NP can facilitate reliable and fast MIC detection. Overall, these demonstrated the reproducibility and capability of dextran-coated gold nanoparticles to rapidly screen multiple samples simultaneously in a high-throughput format, outperforming the traditional 24-hour-long.turbidity method.
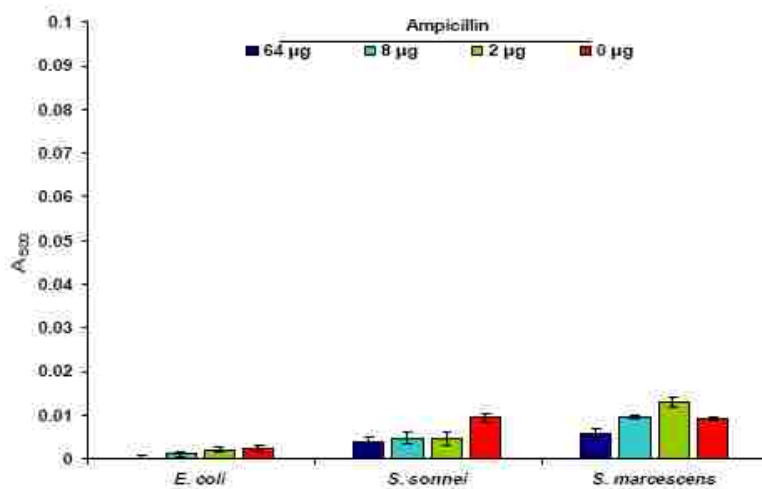
Figure 43: Unassisted determination of MIC by monitoring the absorbance at 500 nm.

Although Dex-Au-NP are ideal for transparent samples, their use in opaque media is limited. Thus, to circumvent this limitation, we developed MRnS-based antimicrobial assays. Initially, we reasoned that the polysaccharide nanosensors' clustering should result in a significant change in the spin-spin relaxation time (T2) of the solution's water protons, facilitating the reliable identification of effective antimicrobial agents. This can be achieved using dextran-coated MRnS along with a protein with high affinity to carbohydrates, such as Concanavalin A (ConA), in a competition assay. Specifically, we hypothesized that upon Con A-induced clustering, the dextran-coated MRnS could differentially respond to the polysaccharide levels associated with bacterial metabolism and growth. Hence, the higher the rate of bacterial metabolic activity, the fewer amount of the available polysaccharides (such as starch) would be, resulting in prominent changes in the sample's ΔT2 when compared to those of the sterile medium (Figure 44).
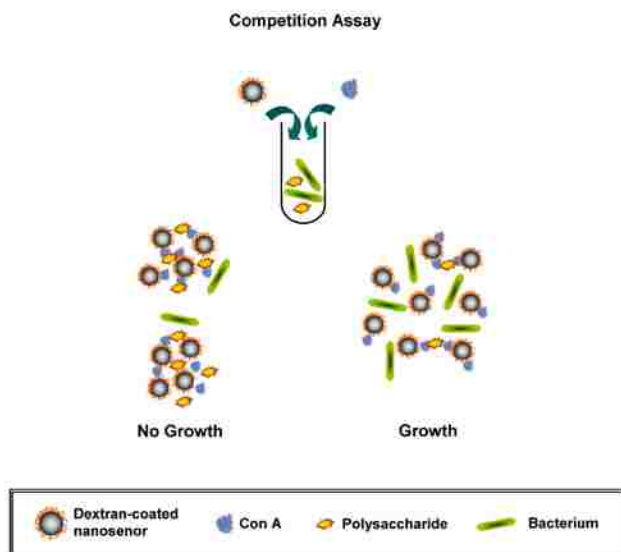
Figure 44: Proposed model for the assessment of antimicrobial susceptibility using dextran-coated polysaccharide MRnS and Concanavalin A.
In this competition assay, the dextran found on the surface of the iron oxide nanoparticles and the starch in solution compete for binding to Con A's carbohydrate-binding domains. This results in changed in the degree of Con A-induced nanoparticle clustering upon bacterial metabolic uptake of the starch.

In our first set of experiments with MRnS, we investigated if dextran-coated iron oxide nanoparticles (Figure 45A, R2 = 300 mM^{-1}s^{-1}) were responsive to changes in starch concentration upon bacterial growth. Initial studies in phosphate buffered saline showed that the nanosensors quickly clustered after addition of Con A, (Figure 45B) forming stable nanoassemblies that induced prominent changes in the T2 within an hour (Figure 46A). During initial optimization studies, we found that a Con A concentration of 1 µg/µL and a nanoparticle solution with a concentration of 0.02 µg Fe/µL provided optimum results (Figure 46B). Thus, we used this iron concentration in all of our experiments. Lower iron concentrations increased the error in the measurement, whereas

117

higher concentrations sacrificed sensitivity and detection kinetics, requiring higher concentrations of Con A.
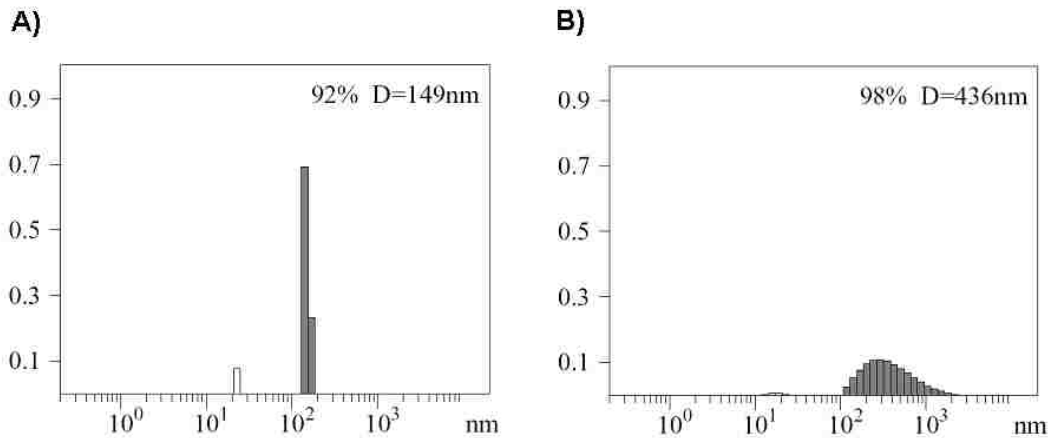
Figure 45: Size distribution of dextran-coated polysaccharide MRnS.
A) Before addition of Con A, and **B)** one hour after Con A addition (1 µg/µL), indicating the formation of nanoparticle clusters.
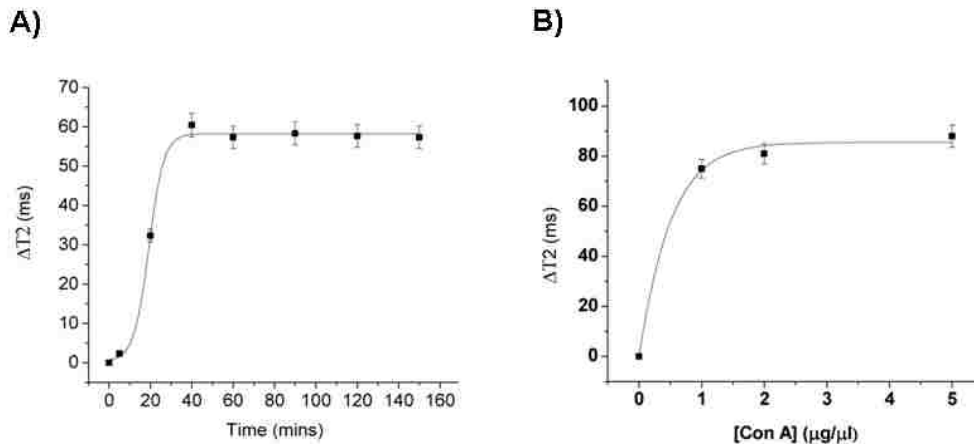
Figure 46: Con A-induced changes in T2.
A) Treatment with Con A (1µg/µL) facilitates prominent changes in the solution's spin-spin relaxation time (T2). **B)** Standard curve for determination of Con A's optimum concentration using a nanoparticle solution with a concentration of 0.02 µg Fe/µl. (Means ± SE)

Next, we assessed the capability of our nanosensors to sense variations in MH broth's starch concentration. In these experiments we added our nanosensors (0.02 μg Fe/μL) to solutions containing increasing amounts of starch in MH broth and Con-A (1 μg/μL). We anticipated that in this competition assay and at low concentrations of starch, the Con A would be able to cluster the dextran- coated magnetic nanosensors resulting in prominent changes in T2. However, as the amount of starch increases, smaller changes in T2 are expected, as Con A would primarily bind to starch. Results showed that after a 30-minute-long incubation at room temperature, a dose-dependent response curve was obtained ($R^2 = 0.99$), demonstrating that the changes in T2 were inversely proportional to the starch concentration (Figure 47A), in accordance with our hypothesis. Notably, the dextran-coated polysaccharide nanosensors were able to quantify starch from concentrations of 77.5 ng/μL, which is the initial starch concentration of a typical MH broth, to 1.5 ng/μL.
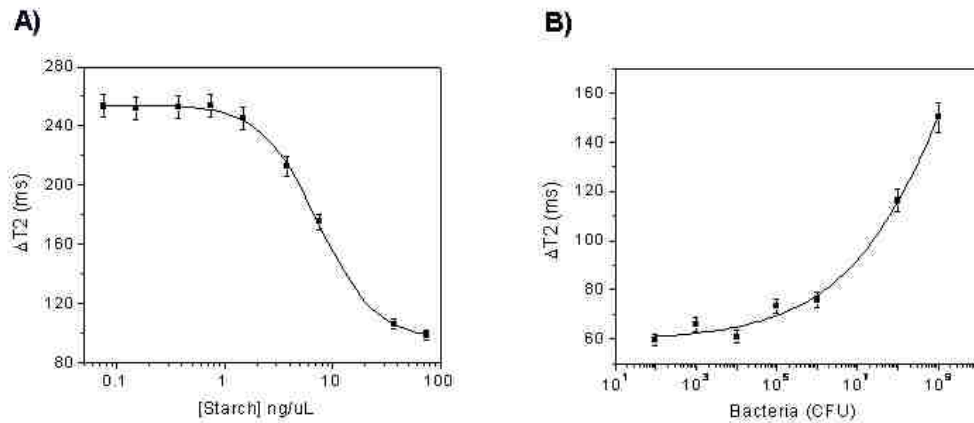
Figure 47: MRnS-mediated sensing of polysaccharide levels and monitoring of bacterial metabolic activity.
A) Quantification of starch in sterile MH broth, and **B)** determination of starch consumption due to bacterial metabolism in MH broth, using the dextran-coated MRnS. (Means ± SE)

We then examined if these polysaccharide MRnS can respond to changes in the starch concentration of MH broth (initial starch concentration = 77.5 ng/µL) due to bacterial metabolic activity. In these experiments, magnetic nanoprobe solutions (0.02 µg Fe/µL) containing aliquots of increasing amounts of *E. coli* were incubated with Con A. Results showed that upon addition of Con A, a dose-dependent response was observed ($R^2 = 0.99$), after a 30-minute incubation at room temperature (Figure 47B). The higher the bacterial population (expressed in Colony Forming Units, CFU) the larger the changes in T2 (ΔT2). This is attributed to the fact that higher bacterial populations utilize more amounts of starch via their metabolic activities, resulting in a concomitant reduction of the media's carbohydrates. As a result, addition of Con A promotes the formation of extensive nanoassemblies, as expected. Notably, even at low bacterial populations (10^2 – 10^4 CFUs) significant changes in T2 were detected. Hence, this demonstrates the high sensitivity of the nanosensors in detecting bacterial metabolic activity, even in the presence of as few as 10^2 CFUs. This is of grave importance in order to prevent septicemia, as very few bacteria in circulation may cause systemic infection leading to death.

In control experiments we found that in the absence of Con A, the presence of increasing amount of bacteria does not affect the T2 of the nanoparticle solution. Specifically, all samples containing either sterile media or different bacterial loads exhibited similar T2 values, suggesting that the presence of bacteria does not alter the spin-spin relaxation times of the non-assembled state (Figure 48). To further corroborate our results, we used heat-inactivated bacteria to halt their metabolic activities.

Consequently, nominal differences were observed between the samples of heat-inactivated bacteria and sterile medium (Figure 49).
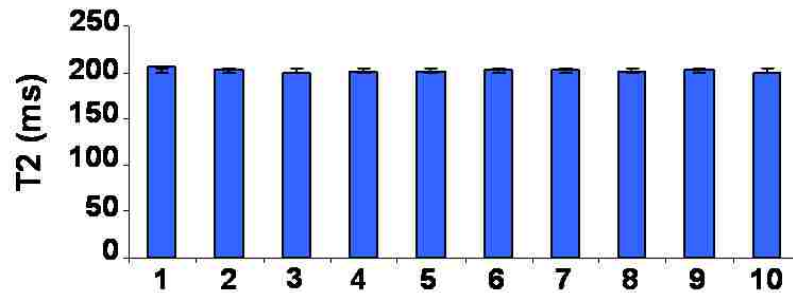
Figure 48: In the absence of ConA, MRnS exhibit the same T2 regardless of the presence of bacteria.
Results obtained after a 30-minute incubation. **1**. Water, **2**. Sterile medium (with starch), **3**. Sterile medium (no starch), **4**. 10^2 CFU *E. coli*, **5**. 10^3 CFU *E. coli*, **6**. 10^4 CFU *E. coli*, **7**. 10^5 CFU *E. coli*, **8**. 10^6 CFU *E. coli*, **9**. 10^8 CFU *E. coli,* **10**. 10^9 CFU *E. coli*. (Means ± SE)
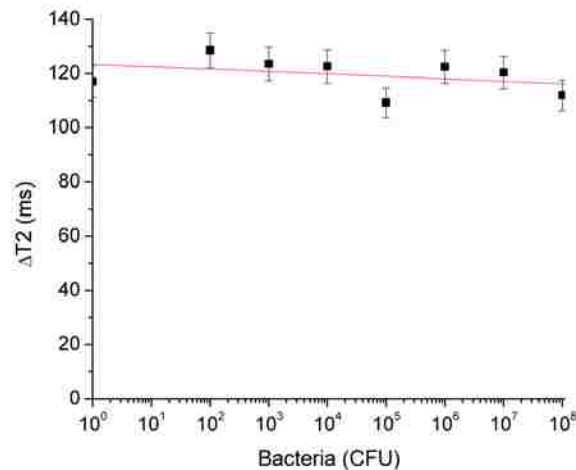
Figure 49: The behavior of MRnS is independent of the heat-inactivated bacterial population, but it is dependent of active bacterial metabolism.
The graph depicts data obtained after a 30-minute incubation at room temperature, in the presence of Con A. Linear fit was applied with an $R^2 = 0.14$ (OriginPro 7.5). (Means ± SE)

121

Based on our dextran-coated MRnS's ability to sense carbohydrate utilization due to microbial metabolism, we examined if these nanosensors can be used for the identification of antimicrobial susceptibility and determination of an antibiotic's minimum inhibitory concentration (MIC). As MIC predicts the success of a particular antibiotic and is an important clinical parameter that dictates treatment in order to minimize adverse side effects, such as renal failure, quick determination of MIC is of paramount importance[114]. Thus, we first examined if the presence of antibiotics in the media might induce non-specific nanoparticle clustering, potentially interfering with the assay's carbohydrate specificity. In these control studies, a bacterial population (10^6 CFU) which is typically used in MIC experiments was incubated in the presence of different antibiotic concentrations. Results showed that these culture conditions did not affect the spin-spin relaxation times of the nanoparticle solution, indicating absence of non-specific antibiotic-mediated nanoparticle assembly (Figure 50).
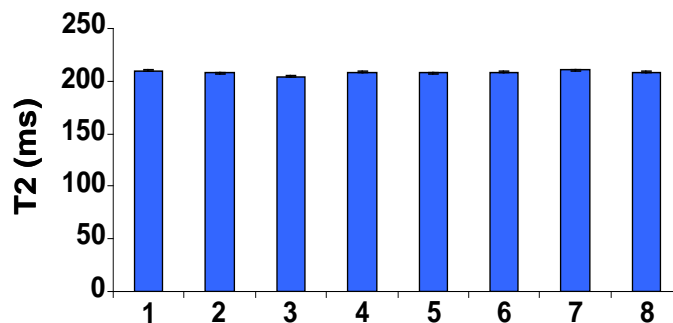
Figure 50: MRnS are not affected by the presence of bacteria and antibiotic.
In the absence of ConA, the IO NPs exhibited the same T2, regardless of the presence of bacteria and antibiotic. **1**. Water, **2**. Sterile medium (with starch), **3**. Sterile medium (no starch), **4**. 64 µg ampicillin, **5**. 8 µg ampicillin, **6**. 2 µg ampicillin, **7**. 1 µg ampicillin, **8**. 0 µg ampicillin.

Subsequently, we examined if bacterial growth and the corresponding carbohydrate uptake are affected by the presence of a particular antibiotic. After incubating *E. coli* for 2 hours in the presence of ampicillin, we took 10-µL bacterial culture aliquots in order to examine them using the dextran-coated polysaccharide nanosensors. Thirty minutes after addition of Con A distinct changes in the T2 were observed, indicating the presence of two cohorts (Figure 51A upper panel). Specifically, the starch utilization and growth of *E. coli* were suppressed at ampicillin concentrations above 8 µg, as demonstrated by the low changes in the ΔT2 compared to the sterile medium. Furthermore, the nanoparticle-derived MIC of 8 µg was confirmed through the turbidity method, which is the current gold standard for antimicrobial susceptibility determination (Figure 51A lower panel). Although both assays provided identical results, the dextran-coated polysaccharide nanosensor assay yielded faster results with an overall time of 2.5 hours (2 hours for bacterial-antibiotic incubation and 30 minutes for nanoparticle readout), as opposed to 24 hours. In addition, the nanosensor-based assay requires smaller bacterial culture volumes (10 µL) as opposed to the turbidity MIC method (2 mL). The latter is of particular logistics importance during epidemics and drug discovery efforts, as it facilitates the simultaneous and cost-effective screening of multiple samples, eliminating the need of tedious visual examination of numerous cultures.
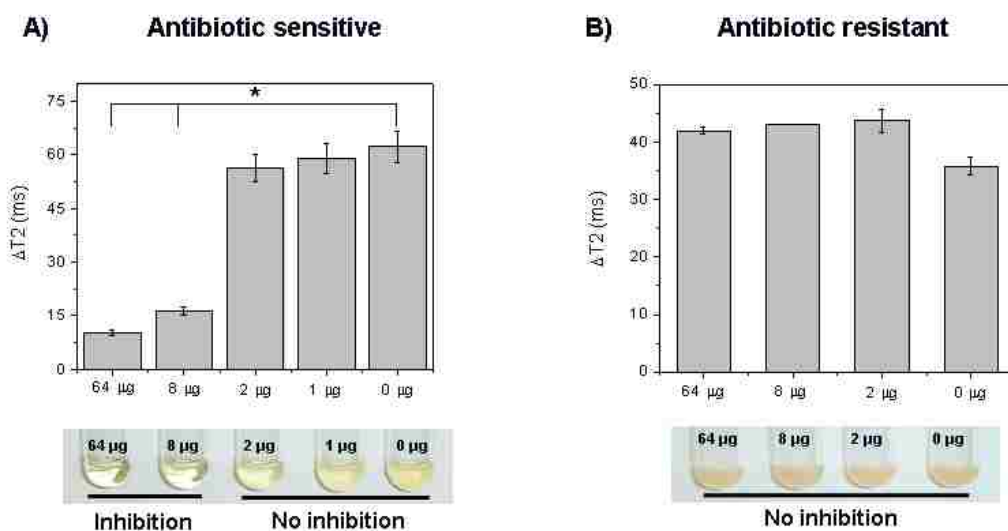
Figure 51: Antimicrobial susceptibility screening in MH broth with dextran-coated polysaccharide MRnS.
A) Determination of *E. coli*'s minimum inhibitory concentration in MH broth, using the changes in spin-spin relaxation times ($\Delta T2$, upper panel) (Means $\pm$ SE; $p < 0.05$) and the turbidity method (lower panel). **B)** Identification of S. *marcescens*' resistance to ampicillin via $\Delta T2$ (upper panel, Means $\pm$ SE) and the turbidity assay (lower panel). The corresponding amount of ampicillin is indicated in the graphs and pictures of the bacterial cultures.

We further validated the antimicrobial susceptibility potential of dextran-coated polysaccharide nanosensors using other bacteria. *Shigella sonnie*, a close relative of the highly pathogenic Shiga-toxin producer *Shigella dysenteriae,* had an ampicillin MIC of 8 µg (Figure 52). Similar to *E. coli*, these results were also obtained within 2.5 hours. Then, we investigated if our assay can determine bacterial drug resistance via the changes in spin-spin relaxation time. As a model system, we used the hospital-acquired pathogen *Serratia marcescens*[129]. This pathogen is resistant to many antibiotics, including ampicillin, due to the presence of resistance plasmids, and is used as a model organism for bacterial drug resistance[62, 130]. Thirty minutes after addition of Con A into the nanoparticle solution, all samples exhibited similar $\Delta T2$ values with no statistically

124

significant differences, indicating that this pathogen is not susceptible to ampicillin (Figure 51B upper panel). Confirmation of our results was achieved via the turbidity method, where after 24 hours all cultures had a reddish turbid appearance, due to the characteristic production of the pigment prodigiosin by *S. marcescens*[131] (Figure 51B lower panel).
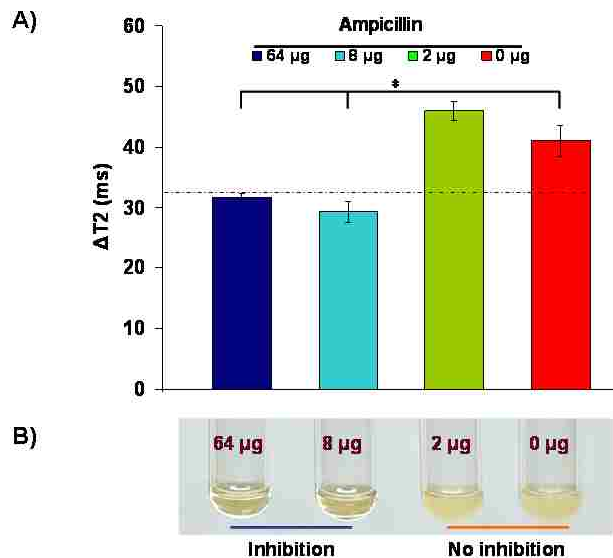
Figure 52: Determination of the minimum inhibitory concentration of *Shigella sonnie*.
A) Using the changes in spin-spin relaxation times (ΔT2) after a 30-min incubation at 25 °C (Means ± SE; $p < 0.05$), and **B)** with the turbidity method. The dotted line indicates the threshold of the drug's successful inhibition.

Due to the fact that many bacteria can either cause septicemia or require growth in optically turbid media, it is important to assess bacterial susceptibility in these complex matrices. However, most current methods cannot be utilized for the detection of molecular targets and assessment of antimicrobial susceptibility in blood. This is due to the strong absorbance and scattering from the matrix's constituents, including platelets and red blood cells (Figures 53 and 54).

125
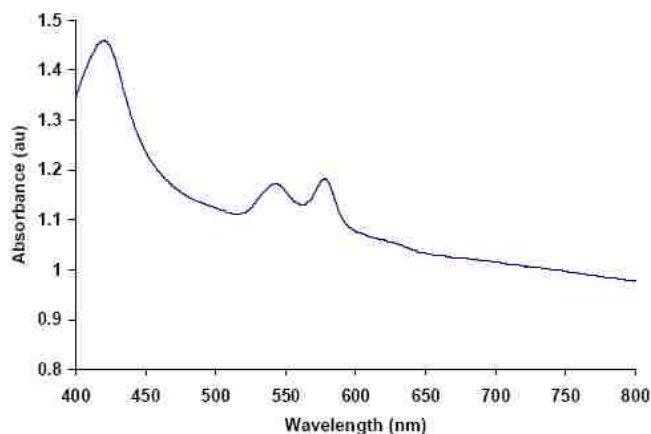
Figure 53: UV-vis profile of a bacterial culture growing in 5%-blood-supplemented MH broth.

E. coli (10^6 CFU) were incubated for 2 hours at 37 ^oC in the presence of 4 µg ampicillin, in 5%-blood-supplemented starch-containing MH broth. Then, a 50-µL bacterial culture aliquot was diluted in 950 µL 1X PBS (Ca^{2+}/Mg^{2+}-free), resulting in similar to the relaxation setup bacterial aliquot dilution. The strong absorbance of blood in the visible spectrum suggests that optical-based methods spanning from 400 to 800 nm may not be effective for MIC determination in this matrix.
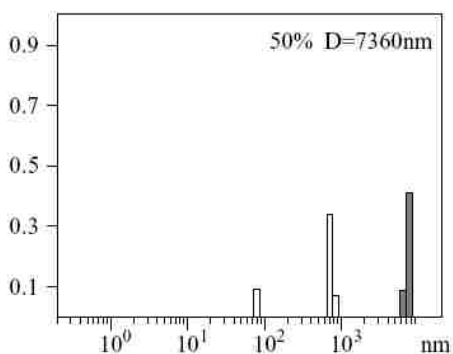
Figure 54: DLS of 5%-blood-supplemented MH broth.

Therefore, considering these drawbacks and the facts that bacterial isolation is a major limitation step in diagnosis and that certain pathogenic microorganisms require growth in specialized media, we examined if the dextran-coated polysaccharide MRnS can assess antimicrobial susceptibility in blood. To address this, we used *E. coli* and *S. marcescens* cultures in blood-supplemented MH broth, grown in the presence of ampicillin for 2 hours at 37 $^{\circ}$C. Aliquots of these cultures (10 µL) were obtained and added into the dextran-coated polysaccharide nanosensors working solution, followed by 10-µL Con A treatment (1 µg/µL). After 45 minutes post-Con A addition at room temperature, we determined that *E. coli*'s ampicillin MIC was 8 µg (Figure 55A), without observing any nanoparticle precipitation (Figure 55C). Additionally, the *S. marcescens*' drug resistance was identified after an hour-long incubation at 25 $^{\circ}$C (Figure 55B).
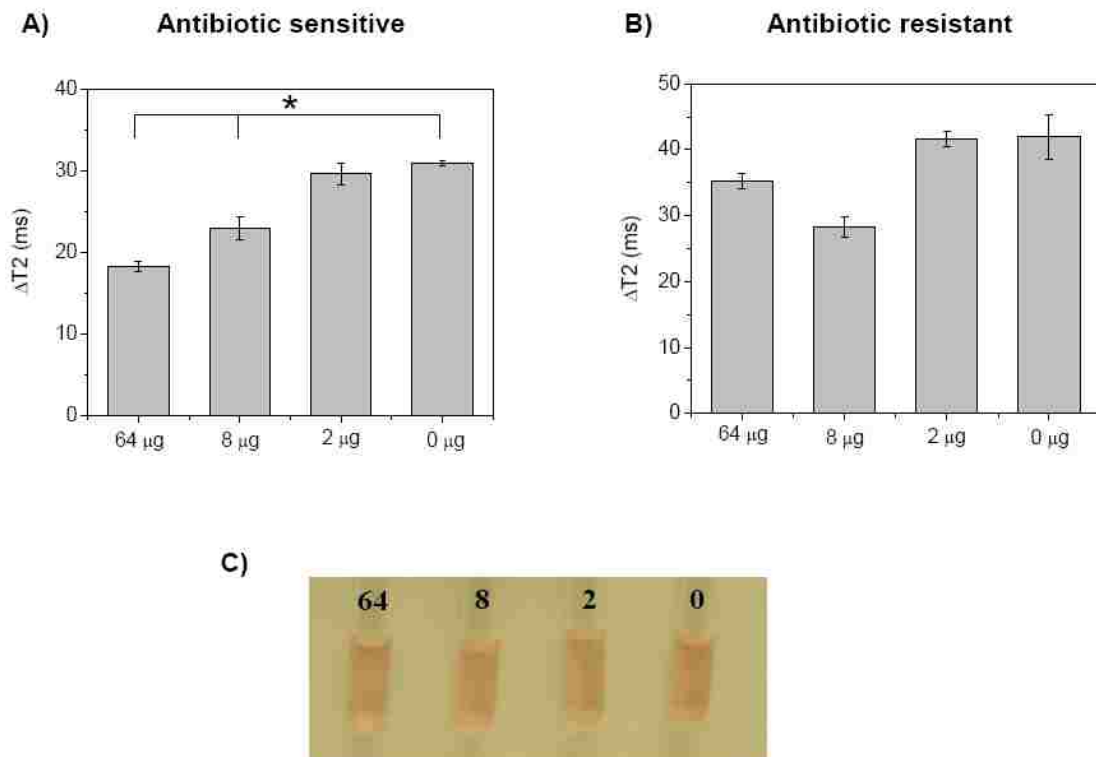
Figure 55: Determination of antimicrobial susceptibility in blood using dextran-coated polysaccharide MRnS.
A) Assessment of *E. coli*'s ampicillin MIC, and **B)** identification of *S. marcescens'* ampicillin resistance in blood (Means ± SE; $p < 0.05$). **C)** Blood cultures in nanoparticle solution demonstrating the absence of nanoparticle precipitation and the optical nature of the solution (numbers indicate the corresponding concentration of ampicillin in µg).

Often times a slight modification in the nanosensors' design and/or the protocol followed can result in significant improvements in either the sensitivity or speed of the assay[132, 133]. Therefore, we hypothesized whether conjugating Con A to the surface of magnetic nanoparticles would achieve faster detection kinetics. For these experiments, we conjugated Con A directly to aminated silica-coated iron oxide nanoparticles. We chose silica-coated instead of dextran-coated iron oxide nanoparticles to avoid possible cross reaction with the dextran on the nanoparticle's surface. In this non-competition

assay (Figure 56), the Con A-conjugated silica coated nanosensors would facilitate the direct sensing of the levels of carbohydrates in solution, as opposed to the competition assay that requires two reagents; the dextran-coated nanoparticles and the Con A for successful sensing. The aminated silica-coated nanoparticles were synthesized using a modified water-based synthetic protocol[124]. The resulting nanoparticles were monodispersed, having a diameter of 145 nm (Figure 57A) and an R2 relaxivity of 225 $mM^{-1}s^{-1}$.
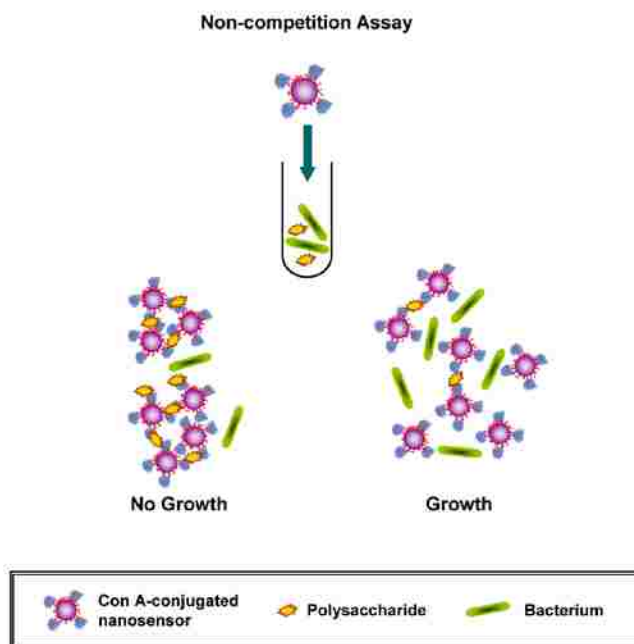
Figure 56: Schematic representation of the assessment of antimicrobial susceptibility using Concanavalin A-conjugated polysaccharide MRnS.
The use of silica-coated nanoparticles and the direct conjugation of Con A to the capping matrix result in a non-competition-based assay format, which may potentially provide faster readout times.
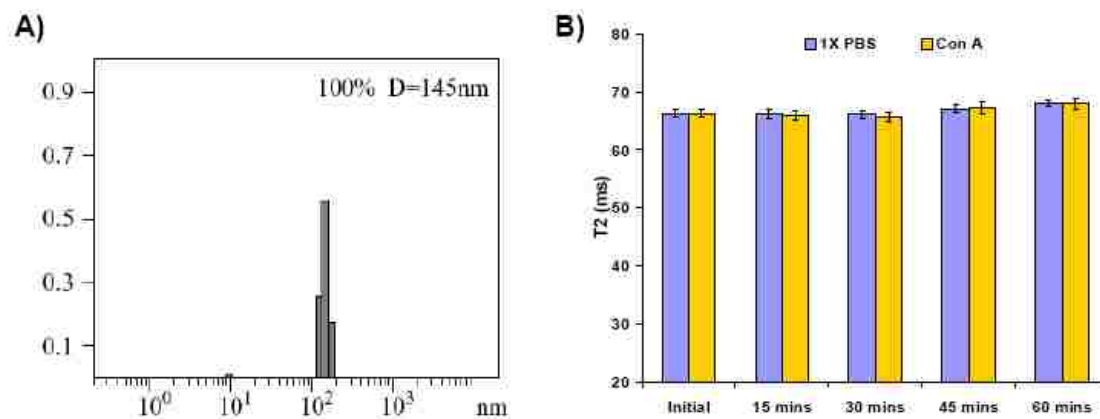
Figure 57: Characterization of silica-coated IONP prior to Con A conjugation.
A) DLS of silica-coated IONP. **B)** Absence of Con A-induced clustering in silica-coated IO nanoparticles, indicating the lack of carbohydrate-containing moieties on the nanoparticles' surface.

In our first set of experiments with the aminated silica-coated nanoparticles, we determined whether these nanoparticles clustered non-specifically in the presence of Con A in solution. As expected, we observed that Con A did not induce any changes in the relaxation times of the nanoparticles (Figure 57B). This demonstrates that the silica coating on these nanoparticles lacks any carbohydrate epitopes, rendering them suitable for the non-competition-based sensing of carbohydrates. Therefore, we conjugated Con A to the aminated silica-coated nanoparticles, via carbodiimide chemistry, resulting in Con A-carrying nanoparticles with a hydrodynamic diameter of ~160 nm (Figure 58) (R2 = 225 mM^{-1}s^{-1}, [Con A] = 0.03 μg/μL).
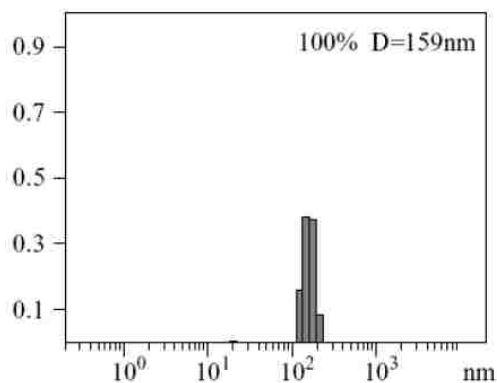
Figure 58: DLS of Concanavalin A-conjugated polysaccharide MRnS.

Next, we compared the kinetic profiles of the dextran-coated nanosensors and Con A-conjugated nanosensors using bacterial *E. coli* blood cultures (10^6 CFU grown in the presence of 2 µg ampicillin). Interestingly, we found that the non-competition assay with the Con A-conjugated MRnS (Figure 59, curve B) provided faster results than the competition assay that utilizes the dextran-coated MRnS (Figure 59, curve A). Specifically, the competition assay format reached its end-point after a 45-minute incubation, whereas the non-competition assay reaches its end-point within 5 minutes upon addition of the bacterial sample. These findings support our hypothesis of achieving faster kinetics due to the direct conjugation of Con A to the nanoparticles.
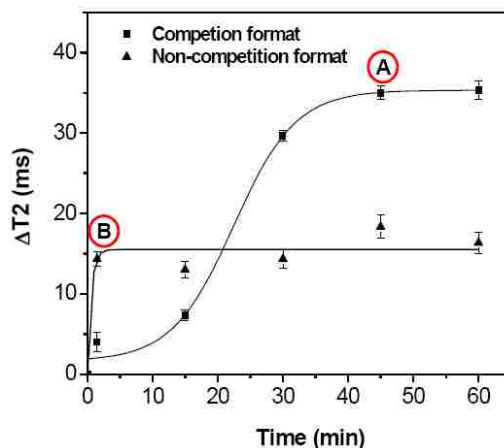
Figure 59: Kinetic profiles of the competition and non-competition assay formats.
Point A represents the end-point of the competition assay utilizing the dextran-coated polysaccharide MRnS, whereas Point B corresponds to the end-point of the non-competition assay based on the Con A-conjugated polysaccharide MRnS.

We finally examined if MIC determination can be achieved using these Con A-conjugated MRnS, in blood cultures of *E. coli* and *S. marcescens*. Immediately upon addition of the bacterial sample into the nanoparticle solution, distinct changes in the T2 were observed. Specifically, within 5 minutes the Con A-nanosensors were able to determine that *E. coli* had an ampicillin MIC of 8 µg (Figure 60A), in line with the data from the dextran-coated nanosensors in the competition assay or the turbidity test. Likewise, within 5 minutes the Con A-conjugated nanosensors assessed that *S. marcescens* was resistant to ampicillin, further corroborating the findings that the non-competition assay format provides faster results than the competition-based assay of the dextran-coated MRnS (Figure 60B).

132
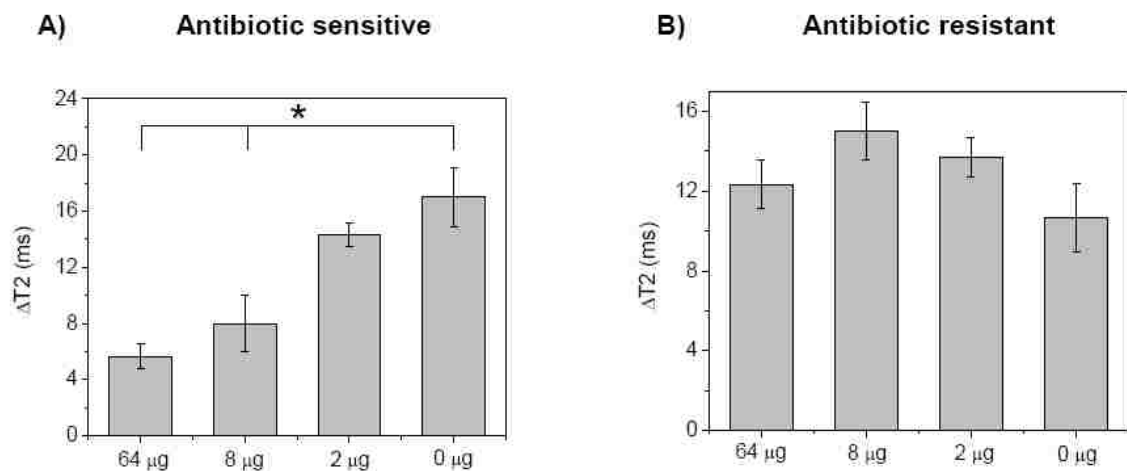
Figure 60: Antimicrobial susceptibility in blood using Con A-conjugated polysaccharide MRnS.
A) Determination of *E. coli*'s ampicillin MIC in blood, and **B)** determination of *Serratia marcescens*' drug resistance in blood with the Con A-conjugated polysaccharide MRnS, five minutes after addition of the bacterial aliquot into the nanoparticle solution (Means ± SE; $p < 0.05$).

Conclusion

➢ Spectrophotometric assessment of antimicrobial susceptibility can be quickly and reliably achieved using dextran-coated gold nanoparticles.

➢ High-throughput screening and determination of MIC can be easily achieved using the discrete clustering of dextran-coated gold nanosensors.

➢ Polysaccharide-sensing MRnS can assess bacterial metabolism through magnetic relaxation.

➢ MRnS can determine MIC and bacterial drug resistance in opaque media, including blood.

➢ Conjugation of Con A to MRnS improves detection kinetics, leading to faster determination of antimicrobial susceptibility than MRnS in competition format.

133

Discussion

Fast identification and administration of the most effective antimicrobial agents is critical for control of bacterial infections. In particular, the emergence of multidrug resistant bacterial strains makes the fast and accurate identification of these pathogens and their susceptibility to antibiotics critical for treatment decision making. As most antimicrobial susceptibility methods require extensive incubations hampering the expedite assessment of drug resistance, we utilized nanosensors in an effort to improve readout times without compromising reliability and sensitivity. Our results indicate that gold nanosensors within less than 3 hours can spectrophotometrically identify if a pathogen is resistant to antibiotics or not. Comparing these results with the workhorse antimicrobial susceptibility assays of the turbidity method or disk diffusion, the nanoparticle-based methodologies are equally sensitive and reliable, yet high-throughput capable and do not need overnight or daylong incubations.

However, considering that antimicrobial susceptibility has to be frequently performed in clinical and opaque samples, we utilized MRnS for MIC determination. We demonstrated that MRnS, either dextran-coated supplemented with Con A or Con A-conjugated, can be used for the quantification of polysaccharides, the assessment of metabolic activity and determination of antimicrobial susceptibility in complex matrices, such as blood, through magnetic relaxation. This approach is an alternative to optical-based assays, which cannot be utilized in opaque media. Additionally, both MRnS assay formats require minute sample volumes, are equally reliable to established methods, and do not require any sample preparation, contrary to other techniques. Intriguingly, a simple modification to the MRnS design by directly conjugating Con A to the

134

nanosensors resulted in more sensitive polysaccharide-sensing MRnS. The Con A-conjugated polysaccharide nanosensor assay yielded faster results, without compromising sensitivity and reliability, due to faster binding kinetics. Also, as there is no need for the addition of a second reagent (Con A), this format might be particularly useful for point-of-care diagnostics and field applications.

Concluding, we anticipate that the MRnS, similar to the gold nanosensors, can be easily adapted for the high-throughput screening of multiple clinical and environmental samples, preventing epidemics and promoting drug discovery. In view of the recent advancements in NMR technology[58, 86, 134], the high-throughput and/or field analysis of multiple samples in complex media should be feasible, even outside of the typical laboratory setting. Overall, we believe that these assays can expedite clinical decision-making and may facilitate the faster discovery of potential antimicrobial agents through the screening of combinatorial libraries and environmental sample fractionations.

CHAPTER VI: GENERAL CONCULSION –"IT'S ONLY THE BEGINNING …"

Molecular recognition events are characterized by unique fidelity, strong affinity and remarkable specificity, through the fine-tuning of multiple interactions and optimization of structural components via evolutionary and selection processes. From antibodies and antigens to receptors and ligands, nature is able to perform a plethora of life supporting functions, including extracellular milieu sensing, matrix attachment, pathogen recognition, nutrient uptake, proofreading, and signal transduction. The second half of the 20th century experienced the birth of molecular diagnostics and the expansion of biological sciences. Consequently, humanity for the first time was able to achieve understanding of basic cellular and sub-cellular events that led to an expansion of the published literature and propelled the development of novel therapeutics and treatment regimes. However, at the end of that century, researchers geared their efforts towards rational design of nanoparticle-based diagnostics, in order to achieve more sensitive diagnostic methods with improved detection thresholds and kinetics. A particular challenge of this approach is the inherent complexity of these nanoparticle-based systems, requiring materials optimization, rigorous testing, instrumentation advancements, as well as efficient coupling and modifying chemistries.

In parallel though, determination of how the fine-tuning of existing systems can evolve molecular diagnostics has provided us with more encouraging results, particularly in the emerging fields of nanotechnology-based diagnostic modalities. For instance in this work, we have demonstrated how the nanoparticles' polymeric coating can modulate intrinsic properties of iron oxide nanoparticles, such as their peroxidase-like activity.

Furthermore, we discovered that the valency of magnetic relaxation nanosensors plays a pivotal role in the relaxation-mediated detection pattern, as well as detection range and kinetics. Reminiscent of biological entities such as viruses, MRnS with high valency were able to quickly detect a single cancer cell in blood samples, due to the abundance of a small ligand found on the nanoparticles. Apart from cancer cells, we were able to detect bacteria, nucleic acid markers, and toxins with high specificity, using a single instrument (relaxometer). Notably, by utilizing a protein that has high affinity to carbohydrates and MRnS, we were able to monitor metabolic activity and quickly assess bacterial drug resistance. This demonstrates that rational selection of existing molecular components and the fine-tuning of nanostructures can synergistically lead to the creation of ultrasensitive probes that use existing instrumentation, propelling drug discovery and point-of-care diagnostics.

Overall, nanotechnology is poised to revolutionize the way how pathogen and infectious diseases diagnostics are performed in the 21st century. By enabling the fast, cost effective and sensitive detection of infectious agents, engineered nanoprobes and nanodevices have the potential to facilitate the robust and high-throughput screening of pathogens in biological and environmental samples. This can be achieved via the unique interactions these nanoprobes and nanodevices have upon recognition of the molecular target or pathogen. Inorganic nanoparticles, semiconductor quantum dots, carbon nanotubes, polymeric nanoparticles, as well as cantilevers and nanochips, all have the potential to be useful in the design of sensitive pathogen diagnostics. Particularly, nanoparticles are versatile, because in principle could substitute the use of fluorescence molecules as tags in most diagnostics applications. Future trends in nanotechnology will

be the design of nanostructures to build miniaturized devices, requiring smaller sample volumes. In addition, as the field of nanotechnology progresses into the design of smart 2-D and 3-D nanoassemblies, new devices that facilitates fast and sensitive pathogen detection in minimal sample volumes are expected. As drug resistance strains continue to emerge, in the forthcoming years we would expect the design of nanosystems that not only are able to sense the presence of a pathogen, but also assess if this pathogen is resistant to a particular drug. Finally, we believe that we are at the dawn of nanomedicine, and more exciting discoveries should be expected as part of the eternal processes of improvement, intellectuality and imagination.

REFERENCES

1.   Taubes, G., The bacteria fight back. *Science* 2008, 321, (5887), 356-61.

2.   Batt, C. A., Materials science. Food pathogen detection. *Science* 2007, 316, (5831), 1579-80.

3.   Martinez, J. L., Antibiotics and antibiotic resistance genes in natural environments. *Science* 2008, 321, (5887), 365-7.

4.   Salyers, A. A.; Whitt, D. D., *Bacterial pathogenesis : a molecular approach*. 2nd ed.; ASM Press: Washington, D.C., 2002; 539 p.

5.   Cirino, F.; Webley, W. C.; West, C.; Croteau, N. L.; Andrzejewski, C., Jr.; Stuart, E. S., Detection of Chlamydia in the peripheral blood cells of normal donors using in vitro culture, immunofluorescence microscopy and flow cytometry techniques. *BMC Infect Dis* 2006, 6, 23.

6.   Ulitzur, S.; Kuhn, J., Construction of lux bacteriophages and the determination of specific bacteria and their antibiotic sensitivities. *Methods Enzymol* 2000, 305, 543-57.

7.   Seo, K. H.; Brackett, R. E.; Frank, J. F.; Hilliard, S., Immunomagnetic separation and flow cytometry for rapid detection of Escherichia coli O157:H7. *J Food Prot* 1998, 61, (7), 812-6.

8.   Notzon, A.; Helmuth, R.; Bauer, J., Evaluation of an immunomagnetic separation-real-time PCR assay for the rapid detection of Salmonella in meat. *J Food Prot* 2006, 69, (12), 2896-901.

9.   Houben, E. N.; Nguyen, L.; Pieters, J., Interaction of pathogenic mycobacteria with the host immune system. *Curr Opin Microbiol* 2006, 9, (1), 76-85.

10.   Schmitt, C. K.; Meysick, K. C.; O'Brien, A. D., Bacterial toxins: friends or foes? *Emerg Infect Dis* 1999, 5, (2), 224-34.

11.   Kayal, S.; Charbit, A., Listeriolysin O: a key protein of Listeria monocytogenes with multiple functions. *FEMS Microbiol Rev* 2006, 30, (4), 514-29.

12.   Endo, Y.; Tsurugi, K.; Yutsudo, T.; Takeda, Y.; Ogasawara, T.; Igarashi, K., Site of action of a Vero toxin (VT2) from Escherichia coli O157:H7 and of Shiga toxin on eukaryotic ribosomes. RNA N-glycosidase activity of the toxins. *Eur J Biochem* 1988, 171, (1-2), 45-50.

13.   Saxena, S. K.; O'Brien, A. D.; Ackerman, E. J., Shiga toxin, Shiga-like toxin II variant, and ricin are all single-site RNA N-glycosidases of 28 S RNA when microinjected into Xenopus oocytes. *J Biol Chem* 1989, 264, (1), 596-601.

14.   Turk, B. E., Manipulation of host signalling pathways by anthrax toxins. *Biochem J* 2007, 402, (3), 405-17.

15.   Mabry, R.; Brasky, K.; Geiger, R.; Carrion, R., Jr.; Hubbard, G. B.; Leppla, S.; Patterson, J. L.; Georgiou, G.; Iverson, B. L., Detection of anthrax toxin in the serum of animals infected with Bacillus anthracis by using engineered immunoassays. *Clin Vaccine Immunol* 2006, 13, (6), 671-7.

16.   Ezzell, J. W., Jr.; Abshire, T. G., Serum protease cleavage of Bacillus anthracis protective antigen. *J Gen Microbiol* 1992, 138, (3), 543-9.

17.   Panchal, R. G.; Halverson, K. M.; Ribot, W.; Lane, D.; Kenny, T.; Abshire, T. G.; Ezzell, J. W.; Hoover, T. A.; Powell, B.; Little, S.; Kasianowicz, J. J.; Bavari, S., Purified Bacillus anthracis lethal toxin complex formed in vitro and during infection exhibits functional and biological activity. *J Biol Chem* 2005, 280, (11), 10834-9.

18.   Rucker, V. C.; Havenstrite, K. L.; Herr, A. E., Antibody microarrays for native toxin detection. *Anal Biochem* 2005, 339, (2), 262-70.

19.   Homola, J.; Dostalek, J.; Chen, S.; Rasooly, A.; Jiang, S.; Yee, S. S., Spectral surface plasmon resonance biosensor for detection of staphylococcal enterotoxin B in milk. *Int J Food Microbiol* 2002, 75, (1-2), 61-9.

20.   Medina, M. B., Development of a fluorescent latex microparticle immunoassay for the detection of staphylococcal enterotoxin B (SEB). *J Agric Food Chem* 2006, 54, (14), 4937-42.

21.   Kawano, Y.; Ito, Y.; Yamakawa, Y.; Yamashino, T.; Horii, T.; Hasegawa, T.; Ohta, M., Rapid isolation and identification of staphylococcal exoproteins by reverse phase capillary high performance liquid chromatography-electrospray ionization mass spectrometry. *FEMS Microbiol Lett* 2000, 189, (1), 103-8.

22.   Carol, J.; Gorseling, M. C.; de Jong, C. F.; Lingeman, H.; Kientz, C. E.; van Baar, B. L.; Irth, H., Determination of denaturated proteins and biotoxins by on-line size-exclusion chromatography-digestion-liquid chromatography-electrospray mass spectrometry. *Anal Biochem* 2005, 346, (1), 150-7.

23.   Jain, K. K., Nanotechnology in clinical laboratory diagnostics. *Clin Chim Acta* 2005, 358, (1-2), 37-54.

24.   Rosi, N. L.; Mirkin, C. A., Nanostructures in biodiagnostics. *Chem Rev* 2005, 105, (4), 1547-62.

25.   Elghanian, R.; Storhoff, J. J.; Mucic, R. C.; Letsinger, R. L.; Mirkin, C. A., Selective colorimetric detection of polynucleotides based on the distance-dependent optical properties of gold nanoparticles. *Science* 1997, 277, (5329), 1078-81.

26.   Mirkin, C. A.; Letsinger, R. L.; Mucic, R. C.; Storhoff, J. J., A DNA-based method for rationally assembling nanoparticles into macroscopic materials. *Nature* 1996, 382, (6592), 607-9.

27.   Daniel, M. C.; Astruc, D., Gold nanoparticles: assembly, supramolecular chemistry, quantum-size-related properties, and applications toward biology, catalysis, and nanotechnology. *Chem Rev* 2004, 104, (1), 293-346.

28.   Sun, Y.; Xia, Y., Shape-controlled synthesis of gold and silver nanoparticles. *Science* 2002, 298, (5601), 2176-9.

29.   Schaller, M.; Laude, J.; Bodewaldt, H.; Hamm, G.; Korting, H. C., Toxicity and antimicrobial activity of a hydrocolloid dressing containing silver particles in an ex vivo model of cutaneous infection. *Skin Pharmacol Physiol* 2004, 17, (1), 31-6.

30.   Chen, S.; Carroll, D. L., Synthesis and Characterization of Truncated Triangular Silver Nanoplates. *Nano Letters* 2002, 2, (9), 1003-1007.

31.   Akamatsu, K.; Ikeda, S.; Nawafune, H., Site-Selective Direct Silver Metallization on Surface-Modified Polyimide Layers. *Langmuir* 2003, 19, (24), 10366-10371.

32.   Medintz, I. L.; Uyeda, H. T.; Goldman, E. R.; Mattoussi, H., Quantum dot bioconjugates for imaging, labelling and sensing. *Nat Mater* 2005, 4, (6), 435-46.

33.   Bruchez, M., Jr.; Moronne, M.; Gin, P.; Weiss, S.; Alivisatos, A. P., Semiconductor nanocrystals as fluorescent biological labels. *Science* 1998, 281, (5385), 2013-6.

34.   Michalet, X.; Pinaud, F. F.; Bentolila, L. A.; Tsay, J. M.; Doose, S.; Li, J. J.; Sundaresan, G.; Wu, A. M.; Gambhir, S. S.; Weiss, S., Quantum dots for live cells, in vivo imaging, and diagnostics. *Science* 2005, 307, (5709), 538-44.

35.   Ness, J. M.; Akhtar, R. S.; Latham, C. B.; Roth, K. A., Combined tyramide signal amplification and quantum dots for sensitive and photostable immunofluorescence detection. *J Histochem Cytochem* 2003, 51, (8), 981-7.

36.   Pellegrino, T.; Parak, W. J.; Boudreau, R.; Le Gros, M. A.; Gerion, D.; Alivisatos, A. P.; Larabell, C. A., Quantum dot-based cell motility assay. *Differentiation* 2003, 71, (9-10), 542-8.

37.   Tully, E.; Hearty, S.; Leonard, P.; O'Kennedy, R., The development of rapid fluorescence-based immunoassays, using quantum dot-labelled antibodies for the detection of Listeria monocytogenes cell surface proteins. *Int J Biol Macromol* 2006, 39, (1-3), 127-34.

38.   Pathak, S.; Choi, S. K.; Arnheim, N.; Thompson, M. E., Hydroxylated quantum dots as luminescent probes for in situ hybridization. *J Am Chem Soc* 2001, 123, (17), 4103-4.

39.   Taton, T. A.; Mirkin, C. A.; Letsinger, R. L., Scanometric DNA array detection with nanoparticle probes. *Science* 2000, 289, (5485), 1757-60.

40.   Zhang, C. Y.; Yeh, H. C.; Kuroki, M. T.; Wang, T. H., Single-quantum-dot-based DNA nanosensor. *Nat Mater* 2005, 4, (11), 826-31.

41.   McCarthy, J. R.; Perez, J. M.; Bruckner, C.; Weissleder, R., Polymeric nanoparticle preparation that eradicates tumors. *Nano Lett* 2005, 5, (12), 2552-6.

42.   Qin, D.; He, X.; Wang, K.; Tan, W., Using fluorescent nanoparticles and SYBR Green I based two-color flow cytometry to determine Mycobacterium tuberculosis avoiding false positives. *Biosens Bioelectron* 2008, 24, (4), 626-31.

43.   Zhao, X.; Hilliard, L. R.; Mechery, S. J.; Wang, Y.; Bagwe, R. P.; Jin, S.; Tan, W., A rapid bioassay for single bacterial cell quantitation using bioconjugated nanoparticles. *Proc Natl Acad Sci U S A* 2004, 101, (42), 15027-32.

44.   Santra, S.; Kaittanis, C.; Grimm, J.; Perez, J. M., Drug/dye-loaded, multifunctional iron oxide nanoparticles for combined targeted cancer therapy and dual optical/magnetic resonance imaging. *Small* 2009, 5, (16), 1862-8.

45.   Hsu, H. Y.; Huang, Y. Y., RCA combined nanoparticle-based optical detection technique for protein microarray: a novel approach. *Biosens Bioelectron* 2004, 20, (1), 123-6.

46.   Lynch, M.; Mosher, C.; Huff, J.; Nettikadan, S.; Johnson, J.; Henderson, E., Functional protein nanoarrays for biomarker profiling. *Proteomics* 2004, 4, (6), 1695-702.

47.   DeMarco, D. R.; Saaski, E. W.; McCrae, D. A.; Lim, D. V., Rapid detection of Escherichia coli O157:H7 in ground beef using a fiber-optic biosensor. *J Food Prot* 1999, 62, (7), 711-6.

48.   Lim, D. V.; Simpson, J. M.; Kearns, E. A.; Kramer, M. F., Current and developing technologies for monitoring agents of bioterrorism and biowarfare. *Clin Microbiol Rev* 2005, 18, (4), 583-607.

49.   Tims, T. B.; Lim, D. V., Rapid detection of Bacillus anthracis spores directly from powders with an evanescent wave fiber-optic biosensor. *J Microbiol Methods* 2004, 59, (1), 127-30.

50.   Perez, J. M.; Josephson, L.; O'Loughlin, T.; Hogemann, D.; Weissleder, R., Magnetic relaxation switches capable of sensing molecular interactions. *Nat Biotechnol* 2002, 20, (8), 816-20.

51.   Perez, J. M.; O'Loughin, T.; Simeone, F. J.; Weissleder, R.; Josephson, L., DNA-Based Magnetic Nanoparticle Assembly Acts as a Magnetic Relaxation Nanoswitch Allowing Screening of DNA-Cleaving Agents. *Journal of the American Chemical Society* 2002, 124, (12), 2856-2857.

52.   Perez, J. M.; Simeone, F. J.; Saeki, Y.; Josephson, L.; Weissleder, R., Viral-induced self-assembly of magnetic nanoparticles allows the detection of viral particles in biological media. *J Am Chem Soc* 2003, 125, (34), 10192-3.

53.   Grimm, J.; Perez, J. M.; Josephson, L.; Weissleder, R., Novel nanosensors for rapid analysis of telomerase activity. *Cancer Res* 2004, 64, (2), 639-43.

54.   Perez, J. M.; Grimm, J.; Josephson, L.; Weissleder, R., Integrated nanosensors to determine levels and functional activity of human telomerase. *Neoplasia* 2008, 10, (10), 1066-72.

55.   Chemla, Y. R.; Grossman, H. L.; Poon, Y.; McDermott, R.; Stevens, R.; Alper, M. D.; Clarke, J., Ultrasensitive magnetic biosensor for homogeneous immunoassay. *Proc Natl Acad Sci U S A* 2000, 97, (26), 14268-72.

56.   Grossman, H. L.; Myers, W. R.; Vreeland, V. J.; Bruehl, R.; Alper, M. D.; Bertozzi, C. R.; Clarke, J., Detection of bacteria in suspension by using a superconducting quantum interference device. *Proc Natl Acad Sci U S A* 2004, 101, (1), 129-34.

57.   Yang, S. Y.; Chieh, J. J.; Wang, W. C.; Yu, C. Y.; Lan, C. B.; Chen, J. H.; Horng, H. E.; Hong, C. Y.; Yang, H. C.; Huang, W., Ultra-highly sensitive and wash-free bio-detection of H5N1 virus by immunomagnetic reduction assays. *J Virol Methods* 2008, 153, (2), 250-2.

58.   Lee, H.; Sun, E.; Ham, D.; Weissleder, R., Chip-NMR biosensor for detection and molecular analysis of cells. *Nat Med* 2008, 14, (8), 869-74.

59.   Wang, D.; He, J.; Rosenzweig, N.; Rosenzweig, Z., Superparamagnetic Fe2O3 Beads-CdSe/ZnS Quantum Dots Core-Shell Nanocomposite Particles for Cell Separation. *Nano Letters* 2004, 4, (3), 409-413.

60.   Baghi, M.; Mack, M. G.; Hambek, M.; Rieger, J.; Vogl, T.; Gstoettner, W.; Knecht, R., The efficacy of MRI with ultrasmall superparamagnetic iron oxide particles (USPIO) in head and neck cancers. *Anticancer Res* 2005, 25, (5), 3665-70.

61.   Gupta, A. K.; Gupta, M., Synthesis and surface engineering of iron oxide nanoparticles for biomedical applications. *Biomaterials* 2005, 26, (18), 3995-4021.

62.   Ito, A.; Kuga, Y.; Honda, H.; Kikkawa, H.; Horiuchi, A.; Watanabe, Y.; Kobayashi, T., Magnetite nanoparticle-loaded anti-HER2 immunoliposomes for combination of antibody therapy with hyperthermia. *Cancer Letters* 2004, 212, (2), 167-175.

63.   Kohler, N.; Sun, C.; Wang, J.; Zhang, M., Methotrexate-Modified Superparamagnetic Nanoparticles and Their Intracellular Uptake into Human Cancer Cells. *Langmuir* 2005, 21, (19), 8858-8864.

64.   Josephson, L.; Tung, C.-H.; Moore, A.; Weissleder, R., High-Efficiency Intracellular Magnetic Labeling with Novel Superparamagnetic-Tat Peptide Conjugates. *Bioconjugate Chemistry* 1999, 10, (2), 186-191.

65.   Thorek, D. L.; Chen, A. K.; Czupryna, J.; Tsourkas, A., Superparamagnetic iron oxide nanoparticle probes for molecular imaging. *Ann Biomed Eng* 2006, 34, (1), 23-38.

66.   Park, S.-J.; Kim, S.; Lee, S.; Khim, Z. G.; Char, K.; Hyeon, T., Synthesis and Magnetic Studies of Uniform Iron Nanorods and Nanospheres. *Journal of the American Chemical Society* 2000, 122, (35), 8581-8582.

67.   Wang, J.; Peng, Z.; Huang, Y.; Chen, Q., Growth of magnetite nanorods along its easy-magnetization axis of [1 1 0]. *Journal of Crystal Growth* 2004, 263, (1-4), 616-619.

68.   Corr, S. A.; Gun'ko, Y. K.; Douvalis, A. P.; Venkatesan, M.; Gunning, R. D.; Nellist, P. D., From Nanocrystals to Nanorods: New Iron Oxideâˆ'Silica Nanocomposites from Metallorganic Precursors. *The Journal of Physical Chemistry C* 2008, 112, (4), 1008-1018.

69.   Nath, S.; Kaittanis, C.; Tinkham, A.; Perez, J. M., Dextran-Coated Gold Nanoparticles for the Assessment of Antimicrobial Susceptibility. *Analytical Chemistry* 2008, 80, (4), 1033-1038.

70.   Perez, J. M.; Asati, A.; Nath, S.; Kaittanis, C., Synthesis of biocompatible dextran-coated nanoceria with pH-dependent antioxidant properties. *Small* 2008, 4, (5), 552-6.

71.   Gao, L.; Zhuang, J.; Nie, L.; Zhang, J.; Zhang, Y.; Gu, N.; Wang, T.; Feng, J.; Yang, D.; Perrett, S.; Yan, X., Intrinsic peroxidase-like activity of ferromagnetic nanoparticles. *Nat Nano* 2007, 2, (9), 577-583.

72.   Perez, J. M., Iron oxide nanoparticles: hidden talent. *Nat Nanotechnol* 2007, 2, (9), 535-6.

73.   Manna, L.; Scher, E. C.; Alivisatos, A. P., Synthesis of Soluble and Processable Rod-, Arrow-, Teardrop-, and Tetrapod-Shaped CdSe Nanocrystals. *Journal of the American Chemical Society* 2000, 122, (51), 12700-12706.

74.   Jaiswal, J. K.; Chakrabarti, S.; Andrews, N. W.; Simon, S. M., Synaptotagmin VII restricts fusion pore expansion during lysosomal exocytosis. *PLoS Biol* 2004, 2, (8), E233.

75.   Alivisatos, A. P.; Gu, W.; Larabell, C., Quantum dots as cellular probes. *Annu Rev Biomed Eng* 2005, 7, 55-76.

76.   Ferrari, M., Cancer nanotechnology: opportunities and challenges. *Nat Rev Cancer* 2005, 5, (3), 161-71.

77.   Seela, F.; Sirivolu, V. R., Nucleosides and oligonucleotides with diynyl side chains: the huisgen-sharpless cycloaddition "click reaction" performed on DNA and their constituents. *Nucleosides Nucleotides Nucleic Acids* 2007, 26, (6-7), 597-601.

78.   Naser, S. A.; Ghobrial, G.; Romero, C.; Valentine, J. F., Culture of Mycobacterium avium subspecies paratuberculosis from the blood of patients with Crohn's disease. *Lancet* 2004, 364, (9439), 1039-44.

79.   Naser, S. A.; Shafran, I.; Schwartz, D.; El-Zaatari, F.; Biggerstaff, J., In situ identification of mycobacteria in Crohn's disease patient tissue using confocal scanning laser microscopy. *Mol Cell Probes* 2002, 16, (1), 41-8.

80.   Naser, S. A.; Schwartz, D.; Shafran, I., Isolation of Mycobacterium avium subsp paratuberculosis from breast milk of Crohn's disease patients. *Am J Gastroenterol* 2000, 95, (4), 1094-5.

81.   Vary, P. H.; Andersen, P. R.; Green, E.; Hermon-Taylor, J.; McFadden, J. J., Use of highly specific DNA probes and the polymerase chain reaction to detect Mycobacterium paratuberculosis in Johne's disease. *J Clin Microbiol* 1990, 28, (5), 933-7.

82.   Cocito, C.; Gilot, P.; Coene, M.; de Kesel, M.; Poupart, P.; Vannuffel, P., Paratuberculosis. *Clin Microbiol Rev* 1994, 7, (3), 328-45.

83.   Manning, E. J.; Collins, M. T., Mycobacterium avium subsp. paratuberculosis: pathogen, pathogenesis and diagnosis. *Rev Sci Tech* 2001, 20, (1), 133-50.

84.   Shin, S. J.; Wu, C. W.; Steinberg, H.; Talaat, A. M., Identification of novel virulence determinants in Mycobacterium paratuberculosis by screening a library of insertional mutants. *Infect Immun* 2006, 74, (7), 3825-33.

85.   Hermon-Taylor, J.; Bull, T. J.; Sheridan, J. M.; Cheng, J.; Stellakis, M. L.; Sumar, N., Causation of Crohn's disease by Mycobacterium avium subspecies paratuberculosis. *Can J Gastroenterol* 2000, 14, (6), 521-39.

86.   Perlo, J.; Demas, V.; Casanova, F.; Meriles, C. A.; Reimer, J.; Pines, A.; Blumich, B., High-resolution NMR spectroscopy with a portable single-sided sensor. *Science* 2005, 308, (5726), 1279.

87.   Badjic, J. D.; Nelson, A.; Cantrill, S. J.; Turnbull, W. B.; Stoddart, J. F., Multivalency and cooperativity in supramolecular chemistry. *Acc Chem Res* 2005, 38, (9), 723-32.

88.   Collins, B. E.; Paulson, J. C., Cell surface biology mediated by low affinity multivalent protein-glycan interactions. *Curr Opin Chem Biol* 2004, 8, (6), 617-25.

89.   Greenspan, N. S., Dimensions of antigen recognition and levels of immunological specificity. *Adv Cancer Res* 2001, 80, 147-87.

90.   Kiessling, L. L.; Gestwicki, J. E.; Strong, L. E., Synthetic multivalent ligands as probes of signal transduction. *Angew Chem Int Ed Engl* 2006, 45, (15), 2348-68.

91.   Larsen, M.; Artym, V. V.; Green, J. A.; Yamada, K. M., The matrix reorganized: extracellular matrix remodeling and integrin signaling. *Curr Opin Cell Biol* 2006, 18, (5), 463-71.

92.   Mathai, M.; Seok-Ki, C.; George, M. W., Polyvalent Interactions in Biological Systems: Implications for Design and Use of Multivalent Ligands and Inhibitors. *Angewandte Chemie International Edition* 1998, 37, (20), 2754-2794.

93.   Mulder, A.; Huskens, J.; Reinhoudt, D. N., Multivalency in supramolecular chemistry and nanofabrication. *Org Biomol Chem* 2004, 2, (23), 3409-24.

94.   Ramsay, A. G.; Marshall, J. F.; Hart, I. R., Integrin trafficking and its role in cancer metastasis. *Cancer Metastasis Rev* 2007, 26, (3-4), 567-78.

95.   Schwartz, M. A.; DeSimone, D. W., Cell adhesion receptors in mechanotransduction. *Curr Opin Cell Biol* 2008, 20, (5), 551-6.

96.   Zutter, M. M., Integrin-mediated adhesion: tipping the balance between chemosensitivity and chemoresistance. *Adv Exp Med Biol* 2007, 608, 87-100.

97.   Kaittanis, C.; Naser, S. A.; Perez, J. M., One-step, nanoparticle-mediated bacterial detection with magnetic relaxation. *Nano Lett* 2007, 7, (2), 380-3.

98.   Cristofanilli, M.; Mendelsohn, J., Circulating tumor cells in breast cancer: Advanced tools for "tailored" therapy? *Proc Natl Acad Sci U S A* 2006, 103, (46), 17073-4.

99.   Nagrath, S.; Sequist, L. V.; Maheswaran, S.; Bell, D. W.; Irimia, D.; Ulkus, L.; Smith, M. R.; Kwak, E. L.; Digumarthy, S.; Muzikansky, A.; Ryan, P.; Balis, U. J.; Tompkins, R. G.; Haber, D. A.; Toner, M., Isolation of rare circulating tumour cells in cancer patients by microchip technology. *Nature* 2007, 450, (7173), 1235-9.

100.   Sha, M. Y.; Xu, H.; Natan, M. J.; Cromer, R., Surface-enhanced Raman scattering tags for rapid and homogeneous detection of circulating tumor cells in the presence of human whole blood. *J Am Chem Soc* 2008, 130, (51), 17214-5.

101.   Bauer, K. D.; de la Torre-Bueno, J.; Diel, I. J.; Hawes, D.; Decker, W. J.; Priddy, C.; Bossy, B.; Ludmann, S.; Yamamoto, K.; Masih, A. S.; Espinoza, F. P.; Harrington, D. S., Reliable and sensitive analysis of occult bone marrow metastases using automated cellular imaging. *Clin Cancer Res* 2000, 6, (9), 3552-9.

102.   Kraeft, S. K.; Ladanyi, A.; Galiger, K.; Herlitz, A.; Sher, A. C.; Bergsrud, D. E.; Even, G.; Brunelle, S.; Harris, L.; Salgia, R.; Dahl, T.; Kesterson, J.; Chen, L. B., Reliable and sensitive identification of occult tumor cells using the improved rare event imaging system. *Clin Cancer Res* 2004, 10, (9), 3020-8.

103.   Parker, N.; Turk, M. J.; Westrick, E.; Lewis, J. D.; Low, P. S.; Leamon, C. P., Folate receptor expression in carcinomas and normal tissues determined by a quantitative radioligand binding assay. *Anal Biochem* 2005, 338, (2), 284-93.

104.   Alix-Panabieres, C.; Riethdorf, S.; Pantel, K., Circulating tumor cells and bone marrow micrometastasis. *Clin Cancer Res* 2008, 14, (16), 5013-21.

105.   Koch, A. M.; Reynolds, F.; Kircher, M. F.; Merkle, H. P.; Weissleder, R.; Josephson, L., Uptake and metabolism of a dual fluorochrome Tat-nanoparticle in HeLa cells. *Bioconjug Chem* 2003, 14, (6), 1115-21.

106.   Shen, T.; Weissleder, R.; Papisov, M.; Bogdanov, A., Jr.; Brady, T. J., Monocrystalline iron oxide nanocompounds (MION): physicochemical properties. *Magn Reson Med* 1993, 29, (5), 599-604.

107.   Nath, S.; Kaittanis, C.; Ramachandran, V.; Dalal, N. S.; Perez, J. M., Synthesis, Magnetic Characterization, and Sensing Applications of Novel Dextran-Coated Iron Oxide Nanorods. *Chemistry of Materials* 2009, 21, (8), 1761-1767.

108.   Quintana, E.; Shackleton, M.; Sabel, M. S.; Fullen, D. R.; Johnson, T. M.; Morrison, S. J., Efficient tumour formation by single human melanoma cells. *Nature* 2008, 456, (7222), 593-8.

109.   Miyauchi, K.; Kim, Y.; Latinovic, O.; Morozov, V.; Melikyan, G. B., HIV enters cells via endocytosis and dynamin-dependent fusion with endosomes. *Cell* 2009, 137, (3), 433-44.

110.   Bowman, M. C.; Ballard, T. E.; Ackerson, C. J.; Feldheim, D. L.; Margolis, D. M.; Melander, C., Inhibition of HIV fusion with multivalent gold nanoparticles. *J Am Chem Soc* 2008, 130, (22), 6896-7.

111.   Bancroft, E. A., Antimicrobial resistance: it's not just for hospitals. *Jama* 2007, 298, (15), 1803-4.

112.   Klevens, R. M.; Morrison, M. A.; Nadle, J.; Petit, S.; Gershman, K.; Ray, S.; Harrison, L. H.; Lynfield, R.; Dumyati, G.; Townes, J. M.; Craig, A. S.; Zell, E. R.; Fosheim, G. E.; McDougal, L. K.; Carey, R. B.; Fridkin, S. K., Invasive methicillin-resistant Staphylococcus aureus infections in the United States. *Jama* 2007, 298, (15), 1763-71.

113.   Liu, C. I.; Liu, G. Y.; Song, Y.; Yin, F.; Hensler, M. E.; Jeng, W. Y.; Nizet, V.; Wang, A. H.; Oldfield, E., A cholesterol biosynthesis inhibitor blocks Staphylococcus aureus virulence. *Science* 2008, 319, (5868), 1391-4.

114.   Andrews, J. M., Determination of minimum inhibitory concentrations. *J Antimicrob Chemother* 2001, 48 Suppl 1, 5-16.

115.   Murray, P. R.; Baron, E. J., *Manual of clinical microbiology*. 9th ed.; ASM Press: Washington, D.C., 2007.

116.   Phillips, R. L.; Miranda, O. R.; You, C. C.; Rotello, V. M.; Bunz, U. H., Rapid and efficient identification of bacteria using gold-nanoparticle-poly(para-phenyleneethynylene) constructs. *Angew Chem Int Ed Engl* 2008, 47, (14), 2590-4.

117.   Katneni, R.; Hedayati, S. S., Central venous catheter-related bacteremia in chronic hemodialysis patients: epidemiology and evidence-based management. *Nat Clin Pract Nephrol* 2007, 3, (5), 256-66.

118.   Tapsall, J. W., Antibiotic resistance in Neisseria gonorrhoeae. *Clin Infect Dis* 2005, 41 Suppl 4, S263-8.

119.   Choi, J. H.; Nguyen, F. T.; Barone, P. W.; Heller, D. A.; Moll, A. E.; Patel, D.; Boppart, S. A.; Strano, M. S., Multimodal biomedical imaging with asymmetric single-walled carbon nanotube/iron oxide nanoparticle complexes. *Nano Lett* 2007, 7, (4), 861-7.

120. Koh, I.; Hong, R.; Weissleder, R.; Josephson, L., Sensitive NMR sensors detect antibodies to influenza. *Angew Chem Int Ed Engl* 2008, 47, (22), 4119-21.

121. Sun, E. Y.; Weissleder, R.; Josephson, L., Continuous analyte sensing with magnetic nanoswitches. *Small* 2006, 2, (10), 1144-7.

122. Tsourkas, A.; Hofstetter, O.; Hofstetter, H.; Weissleder, R.; Josephson, L., Magnetic relaxation switch immunosensors detect enantiomeric impurities. *Angew Chem Int Ed Engl* 2004, 43, (18), 2395-9.

123. Norman, R. S.; Stone, J. W.; Gole, A.; Murphy, C. J.; Sabo-Attwood, T. L., Targeted photothermal lysis of the pathogenic bacteria, Pseudomonas aeruginosa, with gold nanorods. *Nano Lett* 2008, 8, (1), 302-6.

124. Ma, D. L.; Guan, J. W.; Normandin, F.; Denommee, S.; Enright, G.; Veres, T.; Simard, B., Multifunctional nano-architecture for biomedical applications. *Chemistry of Materials* 2006, 18, (7), 1920-1927.

125. Aslan, K.; Lakowicz, J. R.; Geddes, C. D., Nanogold-plasmon-resonance-based glucose sensing. *Anal Biochem* 2004, 330, (1), 145-55.

126. Yoshizumi, A.; Kanayama, N.; Maehara, Y.; Ide, M.; Kitano, H., Self-assembled monolayer of sugar-carrying polymer chain: Sugar balls from 2-methacryloyloxyethyl D-glucopyranoside. *Langmuir* 1999, 15, (2), 482-488.

127. Frens, G., Controlled Nucleation for Regulation of Particle-Size in Monodisperse Gold Suspensions. *Nature-Physical Science* 1973, 241, (105), 20-22.

128. Storhoff, J. J.; Lucas, A. D.; Garimella, V.; Bao, Y. P.; Muller, U. R., Homogeneous detection of unamplified genomic DNA sequences based on colorimetric scatter of gold nanoparticle probes. *Nat Biotechnol* 2004, 22, (7), 883-7.

129. Kramer, A.; Schwebke, I.; Kampf, G., How long do nosocomial pathogens persist on inanimate surfaces? A systematic review. *BMC Infect Dis* 2006, 6, 130.

130. Knothe, H.; Shah, P.; Krcmery, V.; Antal, M.; Mitsuhashi, S., Transferable resistance to cefotaxime, cefoxitin, cefamandole and cefuroxime in clinical isolates of Klebsiella pneumoniae and Serratia marcescens. *Infection* 1983, 11, (6), 315-7.

131. Bennett, J. W.; Bentley, R., Seeing red: the story of prodigiosin. *Adv Appl Microbiol* 2000, 47, 1-32.

132. Lee, J. S.; Han, M. S.; Mirkin, C. A., Colorimetric detection of mercuric ion (Hg2+) in aqueous media using DNA-functionalized gold nanoparticles. *Angew Chem Int Ed Engl* 2007, 46, (22), 4093-6.

133.   Lee, J. S.; Ulmann, P. A.; Han, M. S.; Mirkin, C. A., A DNA-gold nanoparticle-based colorimetric competition assay for the detection of cysteine. *Nano Lett* 2008, 8, (2), 529-33.

134.   Demas, V.; Herberg, J. L.; Malba, V.; Bernhardt, A.; Evans, L.; Harvey, C.; Chinn, S. C.; Maxwell, R. S.; Reimer, J., Portable, low-cost NMR with laser-lathe lithography produced microcoils. *J Magn Reson* 2007, 189, (1), 121-9.